Diss. ETH No. 25636

Multiresonant Nanostructures for Tailoring the Spectral, Directional and Polarization Response of Light Sources

A thesis submitted to attain the degree of

DOCTOR OF SCIENCES of ETH ZURICH

(Dr. sc. ETH Zurich)

presented by

Eva De Leo

MSc in Nanotechnologies for ICTs
Politecnico di Torino, INP Grenoble, EPFL

born on 05.10.1988

citizen of Italy

accepted on the recommendation of

Prof. Dr. David J. Norris (ETH Zurich), examiner
Prof. Dr. Hatice Altug (EPF Lausanne), co-examiner
Prof. Dr. Juerg Leuthold (ETH Zurich), co-examiner
Dr. Ferry Prins (Universidad Autónoma de Madrid), co-examiner

2018

The unexamined life is not worth living.

Apology of Socrates, Plato

To my parents

Acknowledgements

I would like to thank all the people that have made this thesis possible by giving me the tools, space, time, and support to grow professionally and personally.

First of all, my advisor Prof. David J. Norris. I will always be grateful for his trust in giving me this opportunity to work in OMEL and in allowing me to pursue my research interests. His trust in doctoral students and postdocs, his friendly attitude always encouraging questions towards deep understanding, debate, and initiative, and his availability anytime I needed to discuss along with his logical and meticulous approach to scientific and non-scientific topics were always sources of inspiration for me. His support for new exposure and experiences played a crucial role in this thesis as I learned to appreciate the freedom to choose my research path and collaborations. He has also always been understanding of students' life also outside of work and contributed in making our life easier and more enjoyable whenever possible.

Dr. Ferry Prins because of his limitless support and optimism that have been essential for the development of this thesis. He has always found time to discuss and help me, and our collaboration has infinitely enriched me scientifically and personally. I very much enjoyed the fun time in the lab as well as the constant positive encouragement that even new and difficult tasks could just be learned. His expertise and enthusiasm for science and research have always been pleasantly contagious. Thank you also for sharing with me many parts of the processes involved in building a lab, writing proposals and reviewing scientific work.

Prof. Leuthold for accepting to serve on my defense committee, organizing with his group many interesting electromagnetic seminars and courses that I had the pleasure to attend and always being open for questions and discussion.

Prof. Altug for kindly accepting to serve on my defense committee.

Pascale Bachmann for all the support she constantly gives to the group beyond administrative matters. During these years she has always been available to help me in different ways, from giving me life advices to even confronting the impolite employee at my house agency when necessary.

All my fellow colleagues and friends in OMEL and ETH during these years. In particular: Lisa Poulikakos with whom I shared office, lab space and music playlists but also lots of scientific and life discussions and experiences, Jian Cui for always being available to dig with me into life truths, Aurelio Rossinelli for always helping me out in the wet lab and with his quantum-dot experience for Chapter 4, Sriharsha Jayanti and David Kim for their constant help, especially at the beginning of my doctorate, and their American humor, Ario Cocina for the great discussions and his great contribution to the multiresonant project of Chapter 2, Priyank Kumar for always being supportive and trying out many Indian restaurants with me, Kevin McPeak for his endless nanofabrication knowledge spiced up by hilarious jokes and anecdotes, Daniele Braga for his Italian wisdom and organizing fun OMEL events, Jan Winkler, Robert Keitel, Patricia Marquez-Gallego, Boris le Feber, and George Christidis for our enriching collaborations, Freddy Rabouw for always being a loyal Game of Thrones buddy and being available with Raphael Brechbühler for scientific discussion, Stefan Meyer for his help in the lab and his music suggestions, Henar Rojo for help, discussions and for the very nice lunches together, Sarah Kurmulis for the many physics discussions and time outside ETH, Florian Ott, Michael Heinrich, Stefan Kress, Felipe Antolinez, Aniket Mule, Marianne Aellen, Sergio Mazzotti, Philippe Knuesel, Ann-Katrin Michael, Nolan Lassaline, Andreas Riedinger, Mengmeng Deng, Hanbing Fang, Carin Lightner and Deepankur Thureja.

All the students that I enormously enjoyed supervising and the ones that I have collaborated with at OMEL. In particular, Stefan Köpfli that has been essential for the development of Chapter 3 of this thesis, his resourcefulness in our projects has made it always very fun to work together in the lab and outside, Preksha Tiwari for her enthusiastic working attitude and contributions to Chapter 2, Alex Hernandez and Prachi Thureja for

the great collaborations, Krispin Dettlaff, Lukas Robers, Nicolas Blondel, Jorrit Bühlmann, Qianchen Yu, Nicolas Ehrenberg.

Ute Dreschler, Yuriy Fedoryshyn, Antonis Olziersky, Marilyne Sousa and Steffen Reidt for their valuable help in the cleanroom.

The ZIGSS association and all the Italians that supported me in ETH.

The LIMES researchers and Aveth diversity group for the great events and experiences together.

All my close friends and particularly to Denise and Ashwyn with whom few words are needed to understand each other and that have by all means supported me: I am honored and proud of such friendships.

My gine and gini wishing you good luck for a great future, and to all cousins, aunts and uncles that have always brought big warmth in my life.

Nick, for the feeling of home together, for our shared scientific approach to life and for supporting me through ups and downs.

And above all, my family. My parents for all the love and life lessons, even from far away, without which this thesis would have not been possible and my sister Elisa who always brings me happiness with her curious attitude and love for life.

Abstract

Spatial structuring of materials at the nanoscale can strongly modify their optical properties, such as transmission, reflection, and diffraction with respect to their macroscopically homogeneous counterpart. In particular, when they are periodically structured, light propagation, field localization and spontaneous emission can be more efficiently controlled thanks to scattering and interference phenomena. The use of such nanostructures is widely exploited in research areas like sensing, spectroscopy, integrated light sources or thermal emitters. Nevertheless, most nanostructured surfaces are tailored around one single frequency of interest and are therefore unable to provide enhancements, directionality or polarization-dependent properties to more than one colour simultaneously. This thesis aims to address this challenge by developing new concepts of plasmonic and photonic multiresonant antennas to tailor specific properties of light sources including their spectral, directional and polarization response.

First, exploiting the properties of surface plasmon polaritons and extraordinary optical transmission, we introduce a family of plasmonic directional multiresonant antennas that allows for polarization-resolved spectral sorting of fluorescent emission. Inspired by the single-resonant bull's-eye structure, we design multiresonant bull's eyes with polygonal periodic corrugations around a central nanoaperture. The multiresonant character is provided by introducing variations in the periodicity along the different axes of the structure. Moreover, the transmitted resonant color associated with each axis will acquire a unique linear polarization imposed by the axis orientation. We experimentally demonstrate that the resonant wavelengths of our structures can be directly mapped to the transmitted polarization while wavelength-dependent optical beaming is achieved. To explore the potential of these antennas in sensing applications and simplified detection schemes, we couple fluorescent emitters to the central nanoaperture using it as a nanocuvette and tailor the emission from such nanoscale light sources.

The explored multiresonant concept is then extended to plasmonic hole

arrays by modifying each periodicity axis individually and converting single-resonant square and hexagonal hole array structures into rectangular and oblique ones. Exploiting the polarization dependence of the different structure's axes, we show the simultaneous beaming of multiple colors addressable using polarization. These modified hole array configurations can be used to sort different incoming wavelengths or generate polarization-tunable spectral filters that allow for a wide range of transmitted colors. We demonstrate their working principle by sorting the fluorescent emission from colloidal quantum dots coupled to the antenna and proposing polarization-resolved spectral reconstruction of quasi-monochromatic input signals.

Multiresonant bull's-eye antennas can have intriguing applications also beyond the plasmonic extraordinary optical transmission concept. We demonstrate this by using template stripping to obtain direct patterning of colloidal quantum-dot (cQD) thin films. When nanostructured with linear grating patterns, these thin films generate highly directional and polarized emission. Combining the tunability of colloidal quantum dots with the polarization dependence of grating structures, we pattern multiresonant antennas on films composed by cQDs with different spectral properties to realize polarization-tunable on-chip light sources. More complex antenna designs consisting of multiple linear grating building blocks are then explored to engineer structured beams of fluorescence with elaborate intensity and polarization distributions.

Finally, 1D photonic crystals made up of thin films with a periodic modulation in their refractive index are explored as thermal emitters for thermophotovoltaic applications. Along with the numerical optimization of their spectral response to match energies that can be efficiently converted by a photovoltaic cell, the challenges of high temperature operation have guided the experimental optimization in terms of thermal stability and optical properties of the used refractory materials. Following the integration of the thin films on a microcombustor chamber for use in a hybrid thermophotovoltaic platform, we employ a home-built absorptivity/emissivity setup to characterize the nanostructure's efficiency as a high-temperature thermal emitter.

In summary, this thesis introduces plasmonic and photonic multiresonant

nanostructures with a highly directional and polarization-dependent character for use in applications ranging from sensing and spectroscopy to thermophotovoltaics.

Riassunto

La strutturazione dei materiali su scala nanometrica può modificare in maniera significativa le loro proppriетà ottiche, come trasmissione, riflessione e diffrazione rispetto alla loro controparte macroscopicamente omogenea. In particolare, quando la strutturazione é di tipo periodico, la propagazione della luce, la localizzazione del campo elettromagnetico e l' emissione spontanea possono essere controllati in maniera più efficiente grazie ai fenomeni di scattering ed interferenza. L' utilizzo di queste nanostrutture è ampiamente sfruttato in aree di ricerca che comprendono, ad esempio, la spettroscopia, la realizzazione di sensori, sorgenti luminose integrate o emettitori termici. Tuttavia, la maggior parte delle superfici nanostrutturate sono dedicate alla manipolazione di una singola frequenza di interesse e, pertanto, non sono in grado di fornire un aumento del segnale, direzionalità o una dipendenza dalla polarizzazione per piu' di un colore contemporaneamente. Questa tesi si propone di affrontare questo problema sviluppando nuovi concetti di antenne multirisonanti plasmoniche e fotoniche che possano manipolare diverse proprietà delle sorgenti di luce come la loro risposta spettrale, direzionale e di polarizzazione.

Inizialmente, sfruttando le proprietà delle risonanze plasmoniche di superficie e della trasmissione ottica straordinaria (EOT = extraordinary optical transmission), introduciamo una famiglia di antenne plasmoniche multirisonanti e direzionali che consente di differenziare emissioni fluorescenti con diversa frequenza utilizzando la loro polarizzazione. Ispirati dalla struttura chiamata "bull's eye" che sostiene un' unica risonanza, mostriamo il progetto di bull's eyes multirisonanti costituiti da corrugazioni periodiche poligonali attorno ad una nanoapertura centrale. Il carattere multirisonante è fornito introducendo variazioni nella periodicità lungo i diversi assi della struttura. Inoltre, ogni colore risonante trasmesso sarà associato ad un particolare asse ed acquisirà direzionalità ed una specifica polarizzazione lineare imposta dall'orientamento dell'asse. Per esplorare il potenziale di queste antenne come sensori che utilizzano schemi di rileva-

mento semplificati, dimostriamo che accoppiando emettitori fluorescenti alla nanoapertura centrale, che utilizziamo come nanocuvetta, è possibile modificare l'emissione di queste sorgenti di luce nanometriche.

Il concetto di multirisonanza presentato viene poi esteso ad insiemi ordinati di aperture plasmoniche (plasmonic hole arrays) dove, tramite la modifica della periodicità lungo ciascun asse, è possibile convertire le strutture con singola risonanza a matrice quadrata ed esagonale in strutture rettangolari e oblique. Sfruttando le proprietà polarizzanti di ciascun asse, dimostriamo la trasmissione simultanea di più colori distinguibili effettuando un' analisi della loro polarizzazione. Queste configurazioni modificate di hole arrays possono essere utilizzate per separare diverse lunghezze d'onda o generare filtri spettrali controllabili con la polarizzazione tramite i quali un'ampia gamma di colori trasmessi può essere realizzata. Per dimostrare il loro principio di funzionamento, separiamo le emissioni fluorescenti generate da punti quantici colloidali (colloidal quantum dots, cQDs) accoppiati all' antenna ed effettuiamo, tramite analisi della polarizzazione trasmessa, la ricostruzione spettrale di segnali quasi-monocromatici forniti in ingresso.

Le antenne bull's eye multirisonanti possono avere applicazioni intreressanti anche oltre il concetto di EOT. Lo dimostriamo utilizzando il metodo "template stripping" per strutturare su nanoscala, in pochi step di fabbricazione, la superficie di film sottili composti esclusivamente da cQDs. Quando nanostrutturati con reticoli lineari, questi film sottili generano emissioni altamente direzionali e polarizzate. Combinando la sintonizzabilità spettrale dei cQDs con la polarizzazione imposta dalle strutture reticolate, abbiamo fabbricato antenne multirisonanti in un film composto di cQDs con diverse proprietà spettrali e realizzato sorgenti luminose su chip che possono essere controllate tramite polarizzazione. In seguito, presentiamo progetti di antenne più complesse costituite da molteplici blocchi lineari che possono generare fasci di fluorescenza con elaborate distribuzioni di intensità e polarizzazione.

Infine, cristalli fotonici 1D costituiti da film sottili che presentano una modulazione periodica nel loro indice di rifrazione vengono esplorati come emettitori termici per applicazioni termofotovoltaiche. Oltre all' ottimizzazione numerica della loro risposta spettrale per ottenere emissione

termica ad energie che possono essere efficientemente convertite da una cella fotovoltaica, la necessità di funzionamento ad alte temperature ha guidato l' ottimizzazione sperimentale, in termini di stabilità termica e proprietà ottiche, dei materiali refrattari utilizzati. Dopo aver integrato i cristalli fotonici su una camera di microcombustione, come parte di una piattaforma ibrida termofotovoltaica, abbiamo costruito un setup ottico per misurare la radiazione elettromagnetica assorbita/emessa e caratterizzato l' efficienza della nanostruttura come emettitore termico funzionante ad alte temperature.

In sintesi, questa tesi introduce nanostrutture multiresonanti plasmoniche e fotoniche con un carattere altamente direzionale e dipendente dalla polarizzazione per utilizzo in applicazioni che spaziano dalla realizzazione di sensori, fino alla spettroscopia e al termofotovoltaico.

Contents

Chapter 1

Introduction

Light carries information about the world that surrounds us through its properties like intensity, propagation direction, frequency and polarization. It helps us to understand the physical and chemical behaviours of matter very close to us as well as the dynamics in bodies very far from our planet while, at the same time, driving life on earth. For these reasons, being able to control different aspects of light sources has represented a fundamental aspect in everyday life as in more specialized applications such as information or sensing technology. In particular, by increasing efficiency and integration of light sources, nanotechnology has significantly widened their possible applications.

In this introductory chapter, we present the basic concepts of light–matter interactions along with some examples of nanostructures used to tailor light sources and their applications. In particular, we discuss the advantages of periodic photonic and plasmonic nanostructures in shaping the spectral, directional and polarization response of light.

1.1 Properties of light

The perception of light is at the base of communication not only for humans but also for the natural world. From its earliest forms of smoke signals passing by lighthouses to today's optical fibers and displays, light has played a key role as a means of transfering information. By controlling different properties of light like its direction of propagation, color, polarization or intensity we can control the information conveyed by a light beam. Since we can consider light propagating in the form of waves, the electric field behaviour along a certain direction x of a monochromatic plane wave traveling in the z-direction can be described as:

$$E_x(z,t) = E_{0x}\cos(\omega t - kz - \phi_x) \tag{1.1}$$

where E_{0x} is the amplitude of the wave, $\omega = 2\pi f$ with f being the frequency (cycles/s) of the wave that carries the information that we perceive as color, $k = 2\pi f/c = 2\pi/\lambda$ is the wavenumber, with λ being the wavelength, and ϕ_x is the phase of the wave. For a general transverse electromagnetic (TEM) wave propagating along z:

$$\boldsymbol{E}(z,t) = E_x\hat{\boldsymbol{x}} + E_y\hat{\boldsymbol{y}} \tag{1.2}$$

Therefore, in addition to Eq. (1.1), we can express the y-component of the electric field as:

$$E_y(z,t) = E_{0y}\cos(\omega t - kz - \phi_y) \tag{1.3}$$

Light can also acquire different polarization states. If we consider $\phi = \phi_y - \phi_x$ being the phase difference between the two components of the electric field oscillating in the x- and y-direction respectively, we can identify different situations:

- If one of the two components vanishes (example $E_{0x} = 0$), it means that the electric field will oscillate and have a component only along

the other direction (in this case y) along which the wave is said to be linearly polarized (LP). The wave will also be linearly polarized if $\phi = 0$ or π, with a resulting amplitude $|A| = \sqrt{E_{0x}^2 + E_{0y}^2}$ and angle of polarization $\theta = \arctan(E_{0y}/E_{0x})$. For example, if $E_{0x} = E_{0y}$ the plane of polarization makes 45° with the x axis.

- If $E_{0x} = E_{0y}$ and $\phi = +\pi/2$, the light is said to be right circularly polarized (RCP) whereas if $\phi = -\pi/2$, the light is said to be left circularly polarized.
- In any other situation in between the light is said to be elliptically polarized.

Light in which the electric field oscillates randomly in all directions perpendicular to the direction of propagation is usually referred to as unpolarized light (light from many sources, like the sun or incandescent light bulbs, is of this typology).

Another source of information in light is, of course, also the energy that it carries. The intensity (average energy per unit area and unit time) is a measure of the amount of power delivered by the electromagnetic signal. It can be derived as the time averaged value of the Poynting vector's magnitude and is proportional to the square of the amplitude of the electric field as [1]:

$$I = \frac{c\varepsilon_0}{2} E_0^2 \tag{1.4}$$

1.2 Light interactions with matter

Our perception of light is based on its interaction with matter. Light filtered through a window that is scattered by dust particles and captured by the receptors in our eyes or the heat that we feel on our skin under the sunlight are common examples. Nevertheless, this interaction between light and matter is a two-way process. While matter reveals the properties and behaviour of light, light gives us information about materials and their characteristics. In general, the propagation of light through a medium can be described through the refractive index n, which defines the decrease in

the apparent phase velocity of the traveling wave compared to propagation in vacuum: $n = c/v$.

When light propagates from a medium of a given refractive index n_1 into a second medium with refractive index n_2, both reflection and transmission of the light may occur. In a thin film, due to the presence of multiple interfaces between media with different refractive indices and their location at length scales comparable to the wavelength of light, interference between light transmitted and light reflected at the different interfaces can occur. Here, depending on the wavelength of light, this interference can be constructive or destructive, which forms the basis for thin-film-interference filters. In addition, if light is incident under an angle, the beam can also be refracted. In Figure 1.1, an incident light ray

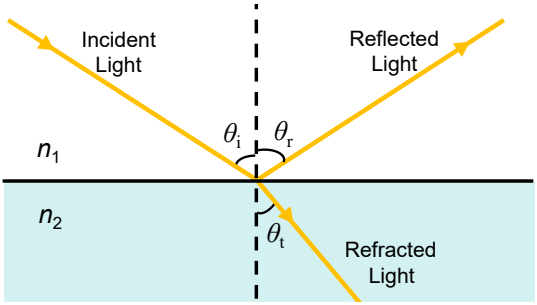

Figure 1.1 – Behaviour of light rays and important parameters involved when reflection and refraction occur at the interface between two media.

strikes at the interface between two media of refractive indices n_1 and n_2. Part of the ray is reflected and part refracted. The angles that the incident, reflected and refracted rays make to the normal of the interface are given as θ_i, θ_r and θ_t, respectively. The law of reflection tells us that:

$$\theta_\mathrm{i} = \theta_\mathrm{r} \tag{1.5}$$

while the behavior of refracted light rays follows Snell's Law:

$$n_1 \sin\theta_\mathrm{i} = n_2 \sin\theta_\mathrm{t} \tag{1.6}$$

where θ_i is the angle between the ray and the surface normal in the first medium, θ_t is the angle between the ray and the surface normal in the second medium, and n_1, n_2 are the indices of refraction of the two media. From this equation it becomes clear that at normal incidence ($\theta_\mathrm{i} = 0$), no refraction will occur. Light will either be transmitted or reflected and the intensities of such reflected and transmitted beams, together with the angles at which refraction occurs, are described by the polarization-dependent Fresnel's equations ($\perp$ for transverse-electric and $\parallel$ for transverse-magnetic polarization of the incident beam). In their reflectance form, these equations can be expressed as [1]:

$$R_\perp = r_\perp^2 = \left[\frac{n_1\cos\theta_\mathrm{i} - n_2\cos\theta_\mathrm{t}}{n_1\cos\theta_\mathrm{i} + n_2\cos\theta_\mathrm{t}}\right]^2 \tag{1.7}$$

$$R_\parallel = r_\parallel^2 = \left[\frac{n_2\cos\theta_\mathrm{i} - n_1\cos\theta_\mathrm{t}}{n_1\cos\theta_\mathrm{t} + n_2\cos\theta_\mathrm{i}}\right]^2 \tag{1.8}$$

indicating the intensity ratio between the reflected radiation I_r and incident radiation I_i: $R = I_\mathrm{r}/I_\mathrm{i}$, while $r_\perp$ and $r_\parallel$ are the corresponding reflection coefficients. However, if we consider the incident angle close to zero (almost along the surface normal: $\theta_\mathrm{i} \approx \theta_\mathrm{t} \approx 0$), the calculation can be simplified and yield a value independent of polarization.

$$R = R_\perp = R_\parallel = \left(\frac{n_1 - n_2}{n_1 + n_2}\right)^2 \tag{1.9}$$

By involving the conservation of power we can calculate the intensity of the transmitted light as: $T = 1 - R$.

Until now, we have only considered reflection and transmission at interfaces between materials that do not absorb light. This is indeed a very good approximation for dielectrics, where the extinction coefficient is negligible for a very large portion of the electromagnetic spectrum. However, if visible light is incident on a metal or semiconductor, some of the incident light can be dissipated due to electron displacement in the material. In this case, Fresnel's coefficients require the refractive index to be specified as the sum of its real and imaginary part: $\tilde{n}(\omega) = n(\omega) + i\kappa(\omega)$, where $\kappa(\omega)$ is the extinction coefficient. Rewriting Eq. (1.1) in its exponential form and inserting the complex refractive index $\tilde{n}$ we obtain:

$$\begin{aligned} E_x(z,t) &= Re\{\tilde{E_{0x}} e^{i(kz-\omega t)}\} = Re\{\tilde{E_{0x}} e^{i(\frac{2\pi(n+i\kappa)}{\lambda} z-\omega t)}\} \\ &= Re\{\tilde{E_{0x}} e^{-(\frac{2\pi\kappa}{\lambda} z-\omega t)} e^{i(\frac{2\pi n}{\lambda} z-\omega t)}\} \end{aligned} \tag{1.10}$$

where $\tilde{E_{0x}}$ is the complex amplitude of the wave and $2\pi\kappa/\lambda$ is called the absorption coefficient since it introduces an exponential decay in the intensity of the wave propagating through the absorbing material.

1.3 Engineering thin-film interference

The development of vacuum science as well as a deeper understanding of surface phenomena and of ways to characterize them, were necessary to the launch of thin-film technology. Thin films occur naturally in a variety of systems and are responsible for the bright colors that can be observed in soap bubbles, oil spills, and in the wings of butterflies. Inspired by nature, the ability to engineer and structure thin films in the nanometer to micrometer range through controllable processes was one of the key requirements to control visible light and develop today's miniaturized devices as well as nanotechnology itself.

Following the behaviour of transmitted and reflected waves introduced in Section 1.2, when light propagates through multiple interfaces, forward and backward travelling waves can interfere with each other, depending on their respective phases. We can distinguish between constructive and

destructive interference. Constructive interference occurs when the crest of a wave meets the crest of another wave at the same point, i.e. when the two waves are in phase with each other. In this case, the amplitude of the resulting wave is the sum of the individual magnitudes. Instead, if a crest of one wave meets the trough of another wave then the final amplitude is equal to the difference in their individual amplitudes. Such waves are out of phase and this is known as destructive interference.

Complete constructive interference occurs when the phase difference between the waves is a multiple of 2π, whereas completely destructive interference occurs when the difference is an odd multiple of π. If the difference between the phases is intermediate between these two extremes, then the magnitude of the displacement of the summed waves lies between the minimum and maximum values. To engineer the constructive and destructive interference pattern at a given wavelength of light, we need to vary its optical path length for a given refractive index. The optical path length (OPL) is the product of the geometric length (d) that the light follows when passing through a medium and the index of refraction of the medium (n) through which it propagates. In a homogeneous medium $OPL = dn$ determining the phase, and therefore the interference, of waves as they propagate. A difference in optical path length between two paths is called the optical path difference (OPD). The optical path difference corresponds then to the phase difference that is acquired between two previously coherent sources (waves that have constant phase shift and same frequency) when passing through different mediums. The OPD can be calculated from the following equation:

$$OPD = d_1 n_1 - d_2 n_2 \tag{1.11}$$

Where d_1 and d_2 are the physical distances the ray travels through media with indices n_1 and n_2. By applying the concepts from Section 1.2 to light incident on a dielectric thin film, we can determine the conditions for interference between light that is reflected by the upper and lower boundaries (see Figure 1.2). The optical path difference (OPD) of the reflected light must be calculated to determine the condition for interference. The

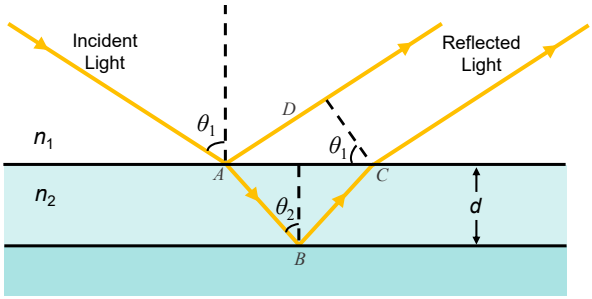

Figure 1.2 – Schematic considering the parameters involved in thin-film interference, when light rays are reflected and refracted at the two interfaces present between media with different refractive indices.

OPD between the two waves is [1]:

$$\text{OPD} = n_2(\overline{AB} + \overline{BC}) - n_1(\overline{AD}) \tag{1.12}$$

Where: $\overline{AB} = \overline{BC} = d/\cos\theta_2$ and $\overline{AB} = 2\,d\,\tan\theta_2 \sin\theta_1$. Using Snell's law:

$$\begin{aligned}\text{OPD} &= n_2\left(\frac{2d}{\cos\theta_2} - 2d\tan\theta_2\sin\theta_1\right) = 2\,n_2\,d\left(\frac{1-\sin^2\theta_2}{\cos\theta_2}\right) \\ &= 2\,n_2\,d\cos\theta_2\end{aligned} \tag{1.13}$$

Interference will be constructive if the optical path difference is equal to an integer multiple of the wavelength of light, λ as: OPD$= 2\,n_2\,d\cos\theta_2 = m\lambda$.

The above example considers the relatively simple situation of interference in a single thin dielectric layer. When a multitude of interfaces is present and a complex refractive index describing absorption is taken into account, the resulting interference spectrum can be calculated nu-

merically. In particular, by engineering thin-film stacks of layers with periodically alternating refractive index very efficient spectral filters can be constructed as we will discuss in Chapter 5.

1.4 Engineering planar periodic thin films

A thin film can also be used to confine and guide light. In fact, in a film that is surrounded by materials with a different refractive index, we can find solutions to the wave equation that represent electromagnetic modes bound to a certain region of space in a particular direction, while they are free to propagate in the other two directions. This category includes modes propagating in high-refractive index waveguides and surface plasmons. Nevertheless, in many applications we are also interested in extracting this confined light. For this purpose, we can efficiently structure the surface of our thin films at the nanoscale as will be discussed in Section 1.4.3.

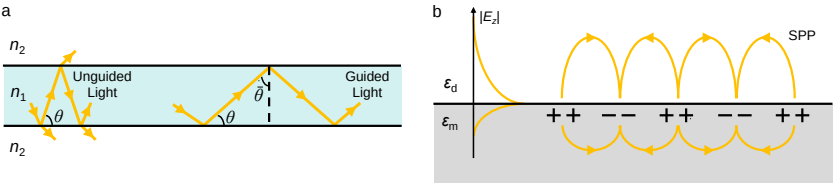

Figure 1.3 – (a) Schematic of a planar dielectric waveguide where light is guided if rays reach the interface with an angle $\overline{\theta} > \theta_c$. (b) Schematic of a surface plasmon polariton (SPP) wave with electric field intensity confined at the interface between a metal and a dielectric.

1.4.1 Waveguided modes

In an optical waveguide, light propagates in a high refractive index medium when surrounded by media with lower refractive index. Due to total internal reflection at the interfaces, the light's propagation is confined. Following from Eq. (1.6), total internal reflection occurs when the incident angle is larger than a critical angle $\theta_c = \arcsin(n_2/n_1)$ with

respect to the surface normal. Light rays present inside the slab that reach the boundaries with an angle θ_m can undergo multiple total internal reflections if the complement of the critical angle $\overline{\theta}_c = \pi/2 - \theta_m > \theta_c$ [2]. From these considerations follows that the propagation constant (i.e. wavevector components in the propagation direction) of the waveguided mode is:

$$\beta_m = n_1 \, k_0 \, cos\theta_m > n_2 \frac{2\pi}{\lambda} \tag{1.14}$$

Such waveguide modes can have an electric field oscillating parallel to the waveguiding plane (transverse electric — TE modes) or perpendicular to this plane (transverse magnetic — TM modes).

1.4.2 Surface plasmons polaritons

The interaction between an incident electromagnetic field and the conduction electrons at the surface of a metal can give rise to evanescent electron–photon waves propagating at the metal–dielectric interface called surface plasmon polaritons (SPPs). These surface modes are TM homogeneous solutions of Maxwell's equations at the interface between two media with dielectric constants $\varepsilon_1(\omega)$ and $\varepsilon_2(\omega)$, where $\varepsilon = \sqrt{n}$. The condition for confinement at the surface requires that one of the dielectric functions is negative and has an absolute value higher compared to the dielectric function of the other material: $\varepsilon_1(\omega) \cdot \varepsilon_2(\omega) < 0$ and $\varepsilon_1(\omega) + \varepsilon_2(\omega) < 0$. These conditions are satisfied if material 1 is a metal and material 2 is a dielectric. In fact, at optical frequencies, the dielectric constant of noble metals, like silver, has a large negative real part, which is the reason for their high reflectivity, and a small imaginary part, associated with energy dissipation due to electrons motion [3]. The propagation constant for the SPP wave is:

$$\beta = \frac{\omega}{c} \sqrt{\frac{\varepsilon_m \varepsilon_d}{\varepsilon_m + \varepsilon_d}} \tag{1.15}$$

where $\varepsilon_m = \varepsilon'_m + i\varepsilon''_m$ is the complex dielectric constant of the metal and ε_d is the one of the dielectric. While the imaginary part of β accounts for the SPP damping upon propagation along the interface, the real part

determines its propagation wavelength:

$$\lambda_{\mathrm{SPP}} \approx \sqrt{\frac{\varepsilon'_{\mathrm{m}} + \varepsilon_{\mathrm{d}}}{\varepsilon'_{\mathrm{m}}\varepsilon_{\mathrm{d}}}}\lambda \tag{1.16}$$

where λ is the excitation wavelength in vacuum. The reduced wavelength of SPPs compared to light in vacuum is an essential feature of plasmonic films since it allows to overcome the diffraction limit and generate strongly confined electric fields that can interact with nanoscale light sources.

1.4.3 Out-coupling using periodic nanostructures

Waveguided modes (both on a metal or in a dielectric slab) have a momentum which is larger than light in vacuum [as demonstrated by Eq. (1.14) and Eq. (1.15)] and are therefore bound to their material/surface. Nevertheless, in many applications from integrated circuits to sensing devices, it is necessary to out-couple such confined energy into the far-field. For this purpose, thin films can be patterned with scattering features for light extraction. In particular, periodic patterning can allow to subtract (or add) momentum to control the direction and polarization of the out-coupled (in-coupled) light in a frequency-dependent fashion such that:

$$\boldsymbol{k}_{\mathrm{in}} \pm \Delta\boldsymbol{k} = \boldsymbol{k}_{\mathrm{out}} \tag{1.17}$$

where $\boldsymbol{k}_{\mathrm{in}}$ and $\boldsymbol{k}_{\mathrm{out}}$ are the wavevectors before and after the scattering process.

Diffraction gratings, consisting of periodically-spaced adjacent elements or apertures, derive their name from the latin *diffringĕre* = "break apart in pieces" (*dis* = "apart" + *frangere* = "to break") [5]. The phenomenon of diffraction was first used by Young to demonstrate that light behaved as a wave [6] since it can "bend" due to an obstacle (e.g. edge, aperture...) even into the region of geometrical shadow of the obstacle. When light hits a diffraction grating made of multiple apertures, using Huygen's principle, every point on a wavefront can be considered a source of secondary spherical wavelets and the new wavefront is the surface tangential to all

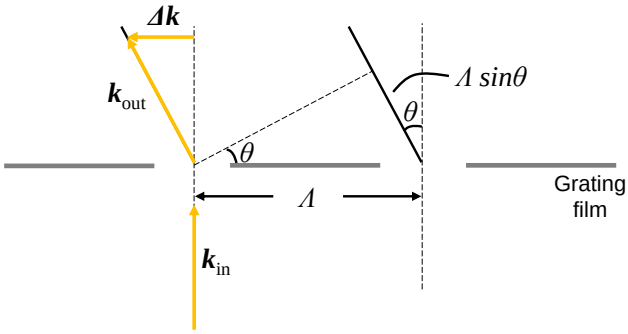

Figure 1.4 – Light diffracted from a grating with periodicity Λ acquires an additional momentum $\Delta \boldsymbol{k}$ and constructive interference occurs for rays whose optical path difference is a multiple of the wavelength [4].

these secondary wavelets. The resulting intensity pattern generated in the Fraunhofer approximation will have maxima at positions where the light emerging from the slits will interfere constructively and minima otherwise. As for the interference phenomenon explained in Section 1.3, for a certain wavelength λ and diffraction angle θ, contructive interference will occur when:

$$\Lambda \, sin\theta = \pm m\lambda \tag{1.18}$$

where Λ is the grating periodicity (distance between two slits) and m is an integer indicating the diffracted order. The "bending" with an angle θ due to diffraction of the incoming beam is the result of additional momentum $\Delta k = \sin\theta \, 2\pi/\lambda = 2\pi/\Lambda$ provided to the out-coupled light.

1.5 Extraordinary optical transmission

Among the simplest type of nanostructures, we can consider a circular aperture in a thin film. Despite its geometrical simplicity such apertures can give rise to very interesting optical phenomena and have therefore been widely investigated in the last centuries. They were of interest to understand the nature of light since Grimaldi in 1660s and then

Young in 1800s investigated the phenomenon of diffraction, and therefore interference, of light waves. In the 1940s, during the second world war, the study of light transmission though small apertures in metallic films was of interest due to its possible implications for military purposes. In these years, Bethe [7] started investigating how light with wavelength λ would be transmitted through a circular aperture with radius $r << \lambda$ in an idealized, infinitely thin and perfectly conducting film. Substituting the hole with a small magnetic dipole in its plane for normal incidence together with an electric dipole in the normal direction to take into account incidence at other angles, his theory predicted that the transmitted light intensity normalized to the hole area $T(\lambda)$ would decay following:

$$T(\lambda) \sim (r/\lambda)^4 \tag{1.19}$$

which implies very low transmitted powers as the wavelength becomes larger than the aperture radius. Following models [9], that took into

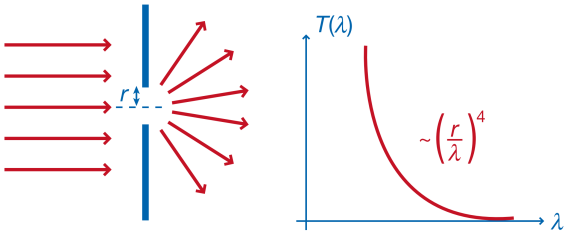

Figure 1.5 – Illustration from [8] representing (left) a schematic of the diffraction through a subwavelength hole in an infinitely thin perfect metal film and (right) the typical transmission spectrum. Reprinted by permission from Springer Nature: Nature [8], copyright 2007.

account the thickness of the metal film which can act as a waveguide for light, gave more insight on the transmittance of light in real sub-wavelength aperture systems. Also in these cases, a significant drop in transmission was predicted above a so-called cut-off wavelength $\lambda_c \sim 4r$.

These conclusions, which have important implications for the realization of optical devices below the diffraction limit, proved incomplete when the phenomenon of extraordinary optical transmission was discovered.

Among different experimental studies on perforated metallic films, in 1998, Ebbesen *et al.* [10] investigated transmission efficiencies through a periodic array of subwavelength holes in optically thick (∼200 nm) films of noble metals (gold and silver) beyond cut-off and in the optical regime, where only very weak direct transmission of light should have been present. In such configuration, they observed high spectral dependence in light transmittance (transmission normalized to the area of the holes on which light was impinging) with strong maxima at specific wavelengths (as shown in Figure 1.6b). Higher intensities of transmitted light were measured compared to what predicted by conventional theories but also compared to the amount of light impinging on the apertures. Therefore, for certain wavelengths, more light was transmitted through such a periodic array of subwavelength holes than through one single larger hole with an area equivalent to the sum of all the small holes. For this phenomenon

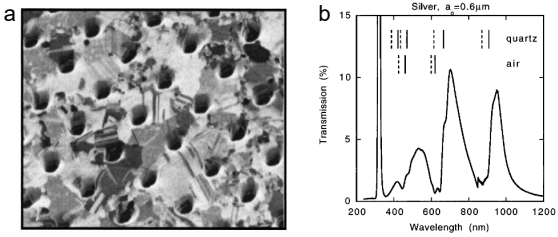

Figure 1.6 – Images from [11]. (a) Two-dimensional hole array pattern in a polycrystalline silver film. (b) Measured transmission at normal incidence for the films in (a). Solid markers indicate SPP modes while dashed markers indicate Wood anomalies for the interfaces present on both sides of the silver film (air and quartz). Reprinted with permission from [11]. Copyright 1998 by the American Physical Society.

to occur, the metal film had to now be seen as an active element in the transmission process. Ebbesen *et al.*, in fact, demonstrated that surface

plasmon resonances excited on the metal film would participate in the transmission process by collecting the light impinged also on areas where no holes were present. Such surface waves would then travel through the holes to the other side of the metal film where they could scatter again as free-space radiation. By mapping the spectral response as a function of the incident angle of the light, they could retrieve the dispersion relation for the SPPs that follows the conservation of momentum:

$$k_{\mathrm{SPP}} = k_x \pm nG_x \pm mG_y = k_0 \sin\theta \pm (n+m)\frac{2\pi}{\Lambda} \tag{1.20}$$

where k_{SPP} is the SPP propagation constant, k_x is the component of the incident wavevector in the direction parallel to the metal surface which is defined, in its magnitude, by $k_0 = 2\pi/\lambda$ and the angle of incidence θ. While n and m are the diffracted orders, G_x and G_y are the grating vectors in the x- and y-direction respectively, with a_0 the periodicity of the grating (same for both directions). For a single interface between a metal and a dielectric with permittivity ε_1 and ε_2, respectively, the effective index of the SPP can be calculated as $n_{\mathrm{SPP}} = \sqrt{\varepsilon_1\varepsilon_2/(\varepsilon_1+\varepsilon_2)}$. From Eq. (1.20) it is possible to predict the rough position (without considering scattering losses that cause a red shift of the resonance position) of the SPP peaks (λ_{SPP}) in a square lattice as:

$$\lambda_{\mathrm{SPP}}(n,m) = \frac{n_{\mathrm{SPP}}\ \Lambda}{\sqrt{n^2+m^2}} \tag{1.21}$$

Such phenomenon indicated that in nanostructured metal thin films unexpected "extraordinary" optical transmission of light could occur under certain conditions. Moreover, the metal in these nanoantennas could be patterned with periodic features of different geometries [12], and both surfaces of the film could be patterned independently to achieve the desired scattering dynamics. Therefore, the same research group started to investigate other type of patterning designs. This included the case of a single subwavelength aperture surrounded by concentric corrugations,

usually referred to as a "bull's eye" [13]. Such a configuration allows one to harvest light of specific colors from the entire corrugated area and direct it towards the central hole via surface plasmons. This property has been exploited to increase the efficiency of photo-detectors or to realize photon sorters with very compact architectures [14–16]. At the same time, in the inverse process, if surface plasmons are traveling on the metal surface (for example excited through the aperture or via local nanoscale emitters), the concentric and periodic geometry allows for the generation of a highly directional beam of light outscattering from the metal surface. Therefore, the generated surface mode radiates back into propagating light with its energy and momentum conserved and defined by the periodicity of the corrugations. In the initial demonstration of this phenomenon [13], Ebbesen *et al.* observed divergence angles of only $\pm 5°$ for light of 660 nm wavelength and full-width-at-half-maximum (FWHM) of 50 nm sent through the aperture and reemerging on the other corrugated side.

The interesting properties of this structure can be manipulated by modifying various geometrical parameters such as the distance and position of the first groove with respect to the central aperture, the displacement of the aperture to break the concentric symmetry and the number of corrugations. In particular, the distance of the first groove from the central aperture determines the phase relation between the light directly transmitted through the aperture and the light generated by the scattering of the SPP waves though the corrugations [17]. Depending on the permittivity of the material, to achieve constructive interference and beaming at a particular wavelength, this distance needs to therefore be appropriately chosen. The importance of such interference effect can also be demonstrated by displacing the position of the aperture within the concentric geometry, to allow for steering of the outscattered beam towards a particular direction [18] with a linear dependence between the hole shift and the shift in angular scattering. Different works have also investigated the effect of an increasing number of rings aroung the central aperture finding that the transmitted intensity saturates after a certain number of rings ($\sim$10) due to the high scattering losses during plasmon propagation on the corrugated film [17].

The narrow emission angles and strong wavelength dependence of bull's

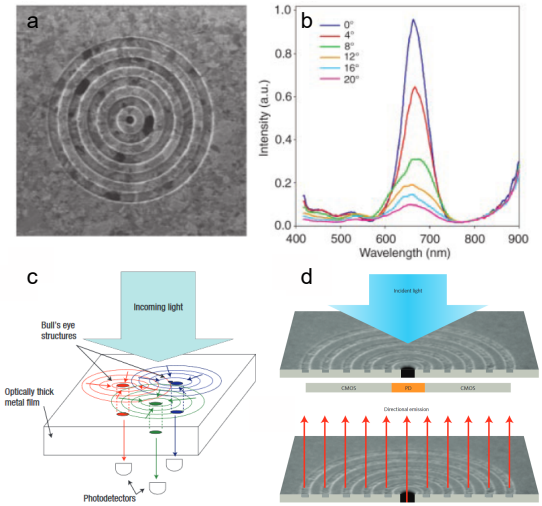

Figure 1.7 – Plasmonic bull's-eye antennas. (a) A scanning electron micrograph and (b) corresponding transmission spectrum of a plasmonic bull's-eye aperture from [13]. Applications ranging from (c) photon sorters [16] to (d) photodetectors or thermal emitters [14–16] have been demonstrated. (a), (b) From [13]. Reprinted with permission from AAAS. (c) Reprinted by permission from Springer Nature: Nature Photonics [16], copyright 2008. (d) Reprinted by permission from Springer Nature: Nature Photonics [15], copyright 2012 and from [14], copyright 2005 The Japan Society of Applied Physics.

eyes have also been used to sort fluorescent emitters or tailor thermal emission among other applications.

1.6 Outline of the thesis

The rapid progress of nanotechnology has enabled the development of many techniques for the deposition and nanostructuring of a wide range of materials. Nanostructured thin films can serve as nanoantennas to optimize the energy transfer from a source to a receiver. Nevertheless, such nanoantennas are usually tailored around a single frequency, direction or polarization of interest. In this thesis we design multiresonant plasmonic and photonic nanoantennas that maintain a highly directional and polarization-dependent character.

In Chapter 2 we will introduce a class of multiresonant plasmonic antennas that allow directional and polarization-dependent out-scattering of many resonant wavelengths simultaneously. Such antennas present a central subwavelength nanoaperture surrounded by concentric polygonal corrugations with a periodicity that varies along the different axes of the structure. Since this design enables EOT of a specific wavelength to which is assigned a unique linear polarization, it is possible to use these multiresonant antennas to generate polarization-dependent beaming of multiple colors. Moreover, the central subwavelength aperture can be used as a nanocuvette to couple nanoscale emitters to the antenna and sort different fluorescent colors using polarization.

In Chapter 3 we extend the multiresonant antenna concept to plasmonic thin films of hole-array structures. The conventional single-resonant square and hexagonal hole array configurations are modified in a rectangular and oblique design, respectively, to achieve simultaneous EOT of multiple wavelengths. The chapter will then introduce the potential of these arrays in generating polarization-tunable color filters, shaping the fluorescent response of semiconductor nanocrystals for color sorting and realizing compact spectrometers.

In Chapter 4 we translate our multiresonant bull's-eye-antenna design to structures made entirely out of colloidal quantum-dots. We demonstrate the versatility of a direct nanopatterning technique based on the template stripping method in realizing highly directional and polarization-dependent fluorescent nanostructures. We further use this framework to show multicolor polarization-controllable beaming and realize functional

fluorescent patterns and tunable light sources. Finally, we exploit the high polarization dependence of our quantum-dot antennas to achieve complex polarization and intensity structuring of light beams.

In Chapter 5 we use thin-film interference to design a 1D photonic crystal thermal emitter for use in thermophotovoltaic (TPV) applications. The quality of the deposited materials for high-temperature stability is investigated along with the optimization of the nanostructure's spectral response. By performing high-temperature absorptivity measurements, we characterize the performance of our photonic crystal after integration on a microcombustor chambers for TPV use.

Chapter 2

Polarization multiplexing of fluorescent emission using multiresonant plasmonic antennas*

Combining the ability to localize electromagnetic fields at the nanoscale with a directional response, plasmonic antennas offer an effective strategy to shape the far-field pattern of coupled emitters. Thanks to these properties, such nanoantennas represent a powerful tool in a wide range of applications including optical imaging, light harvesting, and sensing. One the most successful examples of directional antennas are the so-called bull's-eye structures. Using concentric circular grooves, these single-resonant antennas provide spectrally selective and directional transmission of light. Here, inspired by these structures, we introduce a family of directional multiresonant antennas that allows for polarization-resolved spectral identification of fluorescent emission. The geometry consists of a central aperture surrounded by concentric polygonal corrugations. By varying the periodicity of each axis of the polygon individually, this structure can support multiple resonances that provide independent control over emission directionality for multiple wavelengths. Moreover, since each resonant wavelength is directly mapped to a specific polarization orientation, spectral information can be encoded in the polarization state of the out-scattered beam. To demonstrate the potential of such structures

*This chapter is based on the following publication:
De Leo, E.; Cocina, A.; Tiwari, P.; Poulikakos, L. V.; Marqués-Gallego, P.; le Feber, B.; Norris, D. J.; Prins, F. *ACS Nano* **2017**, *11*, 12167, `https://pubs.acs.org/doi/abs/10.1021/acsnano.7b05269`. Further permissions related to the material excerpted should be directed to ACS.

in enabling simplified detection schemes and additional functionalities in sensing and imaging applications, we use the central subwavelength aperture as a built-in nano-cuvette and manipulate the fluorescent response of colloidal-quantum-dot emitters coupled to the multiresonant antenna.

2.1 Introduction

Plasmonic nanoantennas have the capability to confine electromagnetic fields at the nanoscale as well as shape scattered light into the far field [19, 20]. Careful design of these nanostructures allows controlled in- and out-coupling of targeted wavelengths, propagation directions and polarization states of light [21]. Such properties can be used to engineer light-matter interactions in, for example, light-harvesting [22, 23] and light-emitting technologies [24]. In addition, plasmonic nanoantennas have been extensively employed in spectroscopic and molecular sensing applications [25]. Specifically, efficient near-field coupling between molecules and plasmonic antennas can lead to dramatically improved detection limits, enabling sensitivities down to the single-molecule level [26–29]. At the same time, the antenna design can be used to structure and provide directionality to the far-field radiation pattern of the emission [30–33]. A particularly successful example among directional plasmonic nanoantennas is the so-called bull's-eye structure, which has the ability to generate a tightly confined beam of light in the out-of-plane direction [12, 13, 34]. These antenna structures consist of concentric circular corrugations with a fixed periodicity. In a bull's eye with periodicity Λ, the out-scattering angle θ of a propagating surface plasmon is determined, for a specific wavelength λ, through the momentum matching condition of Eq. (1.20). It follows that light from the first diffraction order is scattered out resonantly in the direction normal to the metal surface when $\lambda = \Lambda\ n_{sp}$, generating the distinct beaming behavior that is characteristic of these structures [35, 36]. Bull's-eye antennas have been successfully employed to shape the far-field radiation profiles of dipole emitters, including colloidal quantum dots [37–40], molecular fluorophores [41, 42], and nitrogen-vacancies centers in diamond [43]. For example, the placement of dyes of different colors inside the central nanoaperture of a bull's eye results in efficient directional sorting and improved detection efficiency of fluorescence [18]. Thanks to the on-resonant unidirectional emission imposed by the bull's-eye antenna, single-molecule sensitivity can be achieved in such a system, even when using low numerical-aperture collection optics [44]. An additional advantage of using nanoaperture bull's eyes in fluorescent sensing is the ability to provide selective excitation of

small analyte volumes present inside the aperture, thereby significantly reducing background fluorescence [45]. While providing excellent control over directionality, conventional bull's eyes are "single-resonant" structures, designed to provide beaming for only one color [46]. However, in many sensing applications it is required to simultaneously probe multiple spectral features, for example when distinguishing between different fluorescent labels [18, 47] or for dual-resonant enhancement of Raman signals [48–51]. Such sensing applications would therefore benefit from a platform that can support resonances for more than one color, while providing directionality for each wavelength individually.

In this chapter, we introduce, in Section 2.2, the design and fabrication of concentric multiresonant bull's-eye structures that can accommodate multiple resonances through variations in the periodicity along the different axes. Since every resonance acquires a specific linear polarization upon outscattering, we can read spectral features using polarization. We will correlate far-field numerical simulations of Section 2.2.3 and k-space measurements of Section 2.3.1 to verify efficient spectral sorting and beaming of light. Finally, in Section 2.4, we will demonstrate that the subwavelength central nanoaperture of our antennas can be used as a nano-cuvette to probe the spectral response of fluorescent emitters, such as colloidal quantum dots.

2.2 Design and fabrication

2.2.1 Design concept

Single nanoapertures surrounded by plasmonic gratings such as bull's-eye apertures [13], have demonstrated efficient light manipulation in sensing and photodetection [20] as well as thermal emission applications [36]. Inspired by these structures, here, we present a family of compact multiresonant bull's-eye antennas for spectral sorting of fluorescence, in which independent control over the directionality of the various resonant colors can be obtained. Our structures consist of concentric polygons that surround a central nanoaperture (see Figure 2.1). In contrast to the concentric circles of the traditional bull's-eye aperture, a concentric polygonal structure can accommodate multiple resonances through

variations in the periodicity along the different axes. Importantly, this allows independent control of the directionality for multiple wavelengths simultaneously. Moreover, benefitting from the breaking of symmetry in the concentric geometry, our multiresonant platform directly associates each resonance with a unique linear polarization [52–55]. Combined with the controlled directionality of emission, it becomes possible to generate polarization-multiplexed beams of light, in which spectral information is efficiently encoded in their polarization state.

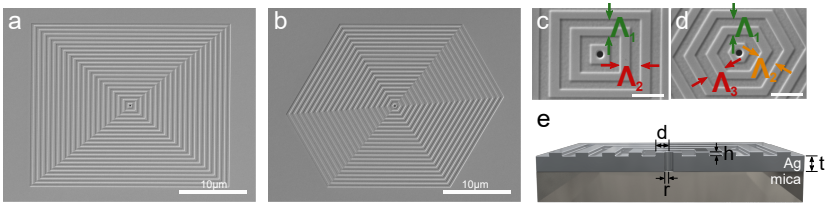

Figure 2.1 – Design of concentric polygonal multiresonant antennas. (a-d) Scanning electron micrographs at different magnifications of a (a, c) rectangular and (b, d) hexagonal multiresonant antenna. The periodicity of the corrugations varies along the different axes of the structures. For the rectangle $\Lambda_1 = 515$ nm and $\Lambda_2 = 635$ nm. For the hexagon $\Lambda_1 = 515$ nm, $\Lambda_2 = 575$ nm and $\Lambda_3 = 635$ nm. (e) Cross-sectional schematic of the structure with distance from the center of the aperture to the first groove $d = 300$ nm, radius r of the aperture, height h of the corrugations, and thickness t of the film. Reprinted with permission from [89], `https://pubs.acs.org/doi/abs/10.1021/acsnano.7b05269`. Further permissions related to the material excerpted should be directed to ACS.

2.2.2 Single-crystalline silver films and FIB patterning

Our multiresonant aperture antennas are fabricated using focused-ion-beam (FIB) milling of single-crystalline silver films grown on mica substrates. Due to the surface nature of SPPs, the quality of the metallic surface used for their propagation should be optimized to minimize losses caused by ohmic heating within the material and random outscattering

from grain boundaries or surface roughness. High-quality surfaces ensure longer propagation lengths, defined as the distance over which the intensity of SPPs decreases to 1/e. This allows for controllable behaviour of SPPs and improved performance of plasmonic devices. The use of single-crystalline films has two main advantages. First, the reduced surface roughness and the absence of grain boundaries allow for increased plasmon propagation lengths [56, 57]. Second, it has been demonstrated that single-crystalline silver provides more homogeneous etching rates during focused-ion-beam milling and thus preserves the smooth surface after patterning, once more providing longer plasmon propagation lengths [57]. These two effects should reduce random scattering and consequently lead to an improved control over the surface-plasmon out-scattering in our system (further demonstrations of the high quality of our films is shown in Section A.1 of Appendix A).

Highest quality grade mica disks (Ted Pella Inc.) with a diameter of 15 mm were freshly cleaved before deposition to reveal clean and flat faces. Silver (Ag) films of 250 nm thickness were epitaxially grown on the mica substrates via DC magnetron sputtering (Lesker PVD 75) [57]. Before deposition, a base pressure lower than 10^{-6} Torr was reached. Sputtering of Ag was performed at an Argon pressure of 6 mTorr and a DC power of 400 W while the substrate temperature was maintained at 360 ° C to yield single-crystalline films. As previously demonstrated by our group, such conditions together with a high deposition rate ($\sim$1.6 nm/sec attainable in our sputtering system) to avoid agglomeration were necessary to achieve a continuous and flat film of single-crystalline Ag. Focused-ion-beam milling (Helios 450, FEI) was then used to pattern the desired geometries into the Ag films with an acceleration voltage of 30 kV and a beam current of 40 pA. Serial patterning of two different etching depths was performed to mill the corrugations and the hole, respectively. High-resolution scanning electron micrographs of a concentric rectangle (Λ_1 = 515 nm, Λ_2 = 635 nm) and a concentric hexagon (Λ_1 = 515 nm, Λ_2 = 575 nm, Λ_3 = 635 nm) are shown in Figure 2.1, respectively. Around the circular central aperture, which is 210 nm in diameter, a total of 20 grooves with a depth of 60 nm were defined (see Figure 2.1e for geometrical parameters of the structure).

2.2.3 Numerical calculations

Comsol Multiphysics 5.2a was used to obtain near- and far-field calculations of the multiresonant bull's-eye structures. Taking advantage of the symmetry around the x and y axis, modeling of rectangular bull's eyes can be efficiently performed using only a quarter of the structure's geometry and therefore reducing significantly the required processing power. The geometry includes a 250-nm-thick Ag film surrounded by air domains. To reduce computation time, only five periodic corrugations with a height of 60 nm were considered. This leads to an overall broadening of the beaming resonances observed (as can be demonstrated comparing the experimental data of 20-ring structures in Figure 2.4b,d with the 10-ring structures in Figure 2.2c,d). In the experimental data indeed, the smoothness of the single-crystalline surface leads to a decrease in FWHM when going from 10 to 20-rings structures. For the simulations, we use refractive indices measured on flat single-crystalline Ag films using a variable-angle spectroscopic ellipsometer (V-VASE or VUV-VASE, J. A. Woollam Co.). In simulations, the number of grooves was limited to 5 due to limitations in computation power.

Excitation of the structure occurs, at normal incidence, from the bottom air layer where the Ag is non-corrugated (corresponding to the excitation configuration in our experimental transmission measurements) and results in an imposed background field, prior to solving the scattering calculation, in the three main domains ($\mathbf{E}_{\mathrm{Air}_1}$ for the bottom air layer Air_1, $\mathbf{E}_{\mathrm{Ag}}$ for the Ag film, and $\mathbf{E}_{\mathrm{Air}_2}$ for the top air layer Air_2):

$$\mathbf{E}_{\mathrm{Air}_1} = \mathbf{E}_0 + \mathbf{E}_{0r} \tag{2.1}$$

$$\mathbf{E}_{\mathrm{Ag}} = \mathbf{E}_{0t} + \mathbf{E}_{0r2} \tag{2.2}$$

$$\mathbf{E}_{\mathrm{Air}_2} = \mathbf{E}_{0t2} \tag{2.3}$$

where $\mathbf{E}_0$ is the initial incident electric field. $\mathbf{E}_{0r}$ and $\mathbf{E}_{0r2}$ are the fields reflected at the first (Air_1/Ag) and second (Ag/Air_2) interface, respectively (since the Ag film is optically thick, additional reflections

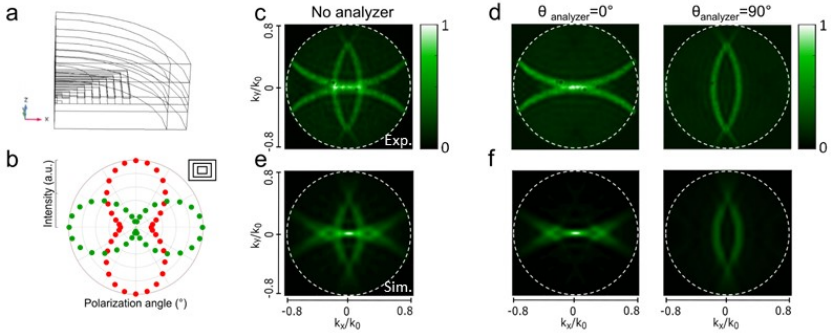

Figure 2.2 – (a) Comsol Multiphysics model of the rectangular bull's-eye antenna. (c, d) Far-field experimental data of rectangular structure consisting of 10 rings compared to calculations (e, f). Polarization-resolved k-space maps are shown in (d) and (f). (b) Calculated intensity as a function of polarization angle extracted from post-processed TE and TM k-space simulations for NA = 0.06. Adapted with permission from [89], `https://pubs.acs.org/doi/abs/10.1021/acsnano.7b05269`. Further permissions related to the material excerpted should be directed to ACS.

within the Ag slab are neglected). $\mathbf{E}_{0t}$ and $\mathbf{E}_{0t2}$ are the fields transmitted through the same interfaces (as introduced in Section 1.2).

For every geometry and wavelength, two separate computations were performed for the case of TM- and TE-polarized plane-wave excitation. In the quarter of geometry, along the sides of symmetry, perfect electric and magnetic conductors (according to the excitation polarization) were set as boundary conditions, whereas on the remaining surfaces we introduced cylindrical perfectly matched layers (PMLs) (Figure 2.2a) to avoid reflections at the boundaries. k-space maps are obtained using the Comsol built-in far-field calculation feature. Response for unpolarized or arbitrarily polarized excitation are extracted from the linear superposition of TE and TM responses using Matlab post-processing. From these results it is possible to report the intensity collected with a numerical aperture

of 0.06 as a function of output polarizer angle for different excitation wavelengths (Figure 2.2b).

2.3 Characterization

2.3.1 *k*-space polarimetry

To investigate the influence of our multiresonant concentric geometry on the angular and spectral scattering of light, we use *k*-space transmission microscopy.

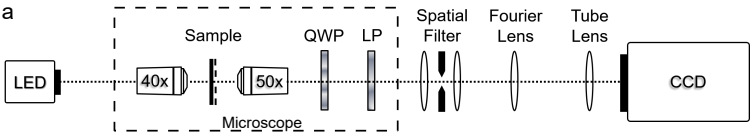

Figure 2.3 – The angle-resolved polarimetry setup consists of a Fourier microscope combined with a rotating linear polarizer and quarter-wave plate. The polarization-dependent *k*-space maps can then be collected on a CCD camera. Reprinted with permission from [89], `https://pubs.acs.org/doi/abs/10.1021/acsnano.7b05269`. Further permissions related to the material excerpted should be directed to ACS.

A modified inverted optical microscope (Ti-U, Nikon) was used for excitation and collection of the measured scattering profile of our multiresonant antennas. Light from a white-light LED (Thorlabs MWWHLP1K) is collimated, filtered with 10 nm FWHM bandpass filters (Thorlabs), and focused at the back unpatterned side of the sample using an excitation objective (NA = 0.6). The light is collected from the corrugated front side and sent to an imaging spectrograph (Acton SP2358, Princeton Instruments) connected to a CCD camera (PIXIS 256E, Princeton Instruments). *k*-space images are obtained by imaging the back focal plane of a 50x collection objective (TU Plan Fluor, NA 0.8, Nikon). The measurement yields angularly resolved intensity maps across the ±53° collection cone of the objective. A spatial filter with a minimum diameter of 1 mm was introduced after the microscope to isolate the structure of interest and a

60 mm Fourier lens was used to project the back aperture of the objective onto the entrance slit of the imaging spectrograph. The k-space color maps were recorded using a fully opened slit and zero dispersion.

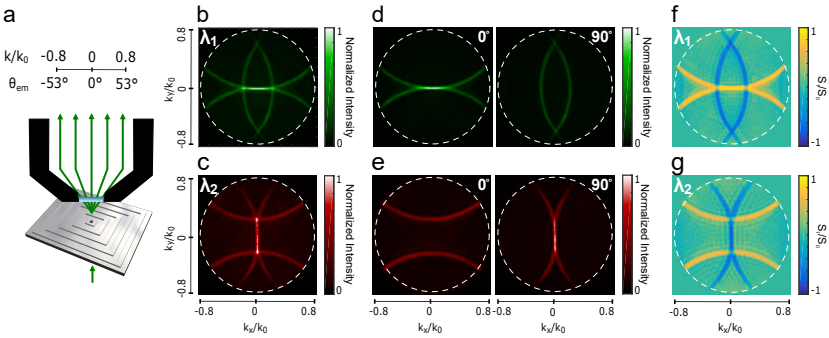

Figure 2.4 – k-space microscopy and polarimetry of rectangular multiresonant antenna. (a) Schematic of k-space measurements where transmitted quasi-monochromatic light is collected using a high-NA objective (NA = 0.8). (b, c) Normalized k-space color maps for the rectangular structure of Figure 1a,c under (b) 550 ± 5 nm and (c) 650 ± 5 nm unpolarized excitation light. The diffraction patterns can be closely predicted using Eq. (1.20). (d, e) Corresponding k-space maps for selected polarization orientations. (f) The Stokes parameter S1 obtained using k-space polarimetry measurements for both 550 nm (top) and 650 nm (bottom) excitation quantifies the ability of the antenna to convert an unpolarized input into a polarized and directional beam. Dashed white lines indicate the numerical aperture of the objective. Reprinted with permission from [89], `https://pubs.acs.org/doi/abs/10.1021/acsnano.7b05269`. Further permissions related to the material excerpted should be directed to ACS.

Figure 2.4b,c show the k-space maps for two different colors of quasi-monochromatic light transmitted through the aperture of the concentric rectangle shown in Figure 2.4a. Orthogonally oriented arc-like patterns of high transmission intensity are observed for each incident color. These arcs are characteristic of the dispersion relation for the two orthogo-

nally oriented linear gratings were the scattering angle is dependent on the grating period [see Eq. (1.20)]. The variation in the periodicity of orthogonal corrugations results, for the rectangular case, in distinct positions of the arcs in k-space as further confirmed by the numerical simulations. For example, while green light ($\lambda_1 = 550 \pm 5$ nm) shows resonant out-coupling via the x axis periodicity ($\Lambda_1 = 515$ nm), leading to high scattering intensity in the normal direction (k_x/k_0 and $k_y/k_0 \approx 0$), light is scattered out at larger angles from the y axis ($\Lambda_2 = 635$ nm). Conversely, red light ($\lambda_2 = 650 \pm 5$ nm) is off-resonant with the x axis, while on-resonant with the y axis. This clearly demonstrates the basic operation principle of the rectangular dual-resonant antenna where the structure's geometry along the two axes can be controlled independently to satisfy the resonant condition for separate colors. Moreover, the high degree of angular control obtained through our structures is illustrated by the small width of the resonances at the center of k-space, measuring a FWHM of around $\pm 2°$. A fundamental aspect of the surface plasmons scattering by our multiresonant geometry is that the scattered-light polarization is acquired from the parallel polarization component of the propagating surface plasmons. It is therefore oriented along the respective axis of the polygon and parallel to the grating vector [58, 59]. To decompose the scattered patterns of Figure 2.4b,c into the different polarization components, we introduce a linear polarizer after the collection objective of Figure 2.4a. The horizontal and vertical polarization contributions are shown for green and red light in Figure 2.4d,e, respectively (for example, in the green case the 0° horizontal contributions are generated due to scattering from the vertically oriented periodicity of 515 nm and, correspondingly, the 90° contributions come from the orthogonally oriented horizontal grating periodicity which is not resonant with the green color). It is evident from these maps that the resonant conditions for the two colors occur at orthogonal polarization orientations and are separable using a linear polarizer.

To quantify the polarizing properties of our device, we perform k-space polarimetry [60] by introducing a quarter-wave plate and a linear polarization analyzer after the collection objectives in the double-turret of the inverted microscope, using home-built filter-cubes. By performing angle-resolved polarimetry of the transmitted light, we can retrieve

the Stokes parameters to fully characterize the polarization state of the resulting optical beam [61–63]. For example, the Stokes parameter S_1, shown in Figure 2.4f,g for the two resonant wavelengths, quantifies the amount of linearly horizontal (LHP) and linearly vertical polarization (LVP) that our structure imposes on the scattered light (S_1 = LHP-LVP). S_1 describes the ability of this multiresonant antenna to convert an unpolarized input into a polarized and directional beam. At the center of k-space, for both wavelengths, we find maxima of $|S_1|$ that reach > 0.75, demonstrating that each wavelength has been efficiently mapped to a specific corresponding polarization. Figure 2.5 shows the other k-space polarimetry maps of a rectangular structure with $\Lambda_1 = 515$ nm and $\Lambda_2 = 635$ nm under illumination with $\lambda = 550$ nm light. The degree of linear and the degree of circular polarization were calculated as DLP $= (S_1^2 + S_2^2)^{-1/2} / S_0$ and DCP $= |S_3|/S_0$ respectively, where S_0, S_1, S_2, and S_3 are the Stokes parameters. S_0 describes the total intensity of the beam, S_1 describes, as already mentioned, the preponderance of linearly horizontal polarization with respect to linear vertical polarization, S_2 describes the preponderance of light linearly polarized at 45° over the one polarized at -45° (S_2 = L-45P - L+45P) and S_3 quantifies the preponderance of right handed circularly polarized light over left handed circularly polarized light (S_3 = RCP - LCP) [63]. The total degree of polarization was calculated as DP $= (S_1^2 + S_2^2 + S_3^2)^{-1/2}/S_0$.

Compared to the relatively simple orthogonal patterns generated by a concentric rectangle, more complex k-space patterns are obtained when using higher order polygons. For example, using green ($\lambda_1 = 550 \pm 5$ nm), orange ($\lambda_2 = 600 \pm 5$ nm), and red ($\lambda_3 = 650 \pm 5$ nm) illumination colors, k-space maps for the hexagonal bull's eye of Figure 2.1b are shown in Figure 2.6. Resonant conditions can be observed every 60°, as imposed by the hexagonal geometry of our antenna for the different resonant colors (see Figure 2.6a-c). These resonant conditions become more apparent when using a linear polarizer, providing selective transmission of the three different beaming conditions (see Figure 2.6d-f). As for the rectangular case, each polarization contribution is obtained mainly via scattering from the orthogonally oriented axis of the structure.

Similarly, polarization resolved k-space maps of the transmission of four different colors through an octagonal structure are presented in

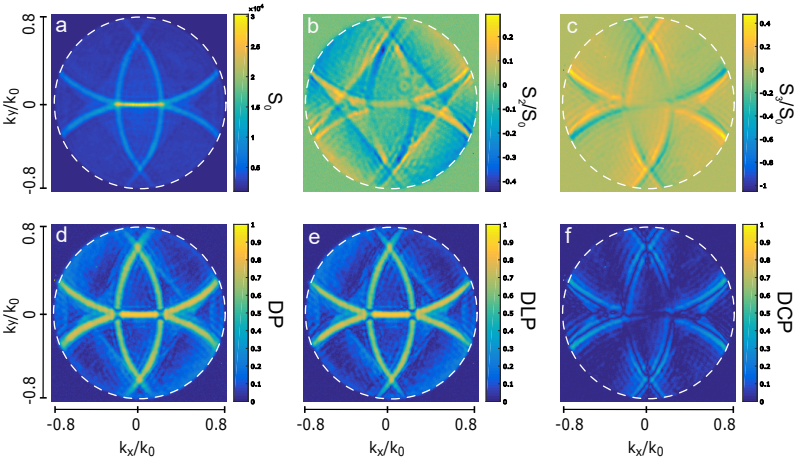

Figure 2.5 – Full characterization of the polarization state of the rectangular structure shown in Figure 2.1a. The optical excitation wavelength was $\lambda = 550$ nm. The S_1 parameter is shown in Figure 2.4f. Reprinted with permission from [89], `https://pubs.acs.org/doi/abs/10.1021/acsnano.7b05269`. Further permissions related to the material excerpted should be directed to ACS.

Figure 2.7. As for the case of a rectangular and hexagonal antenna, k-space maps can be obtained for the four different resonant colors using unpolarized excitation (Figure 2.7c-f). As shown in Figure 2.7g-j, the beaming conditions for the four different wavelengths in this case occur with the expected 45° separation and can therefore be isolated using four different polarization orientations of the output analyzer. Therefore, while the presence of additional diffraction arcs increases the complexity of the k-space maps, introducing a linear polarization analyzer provides an effective way to emphasize the individual resonances.

The presented direct mapping of each resonant color to a unique linear polarization, combined with the directional control over the out-scattering angle, provides us with the opportunity to generate multiplexed beams

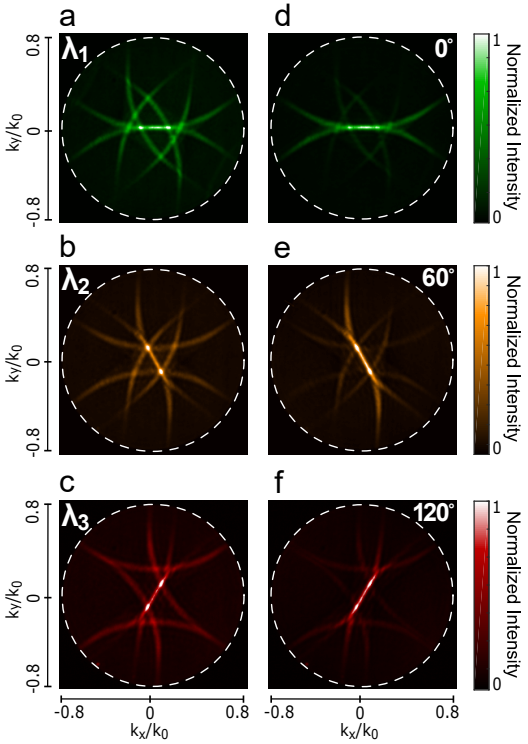

Figure 2.6 – k-space measurements of hexagonal multiresonant antenna. Normalized k-space color maps for light scattered off the structure in Figure 2.1b. We use (a) 550 ± 5, (b) 600 ± 5, and (c) 650 ± 5 nm wavelength excitation. (d-f) From the patterns in (a-c), the different polarization components, for which a color-dependent beaming condition is satisfied, are separated. Due to the geometry of the structure this occurs every 60°. Reprinted with permission from [89], `https://pubs.acs.org/doi/abs/10.1021/acsnano.7b05269`. Further permissions related to the material excerpted should be directed to ACS.

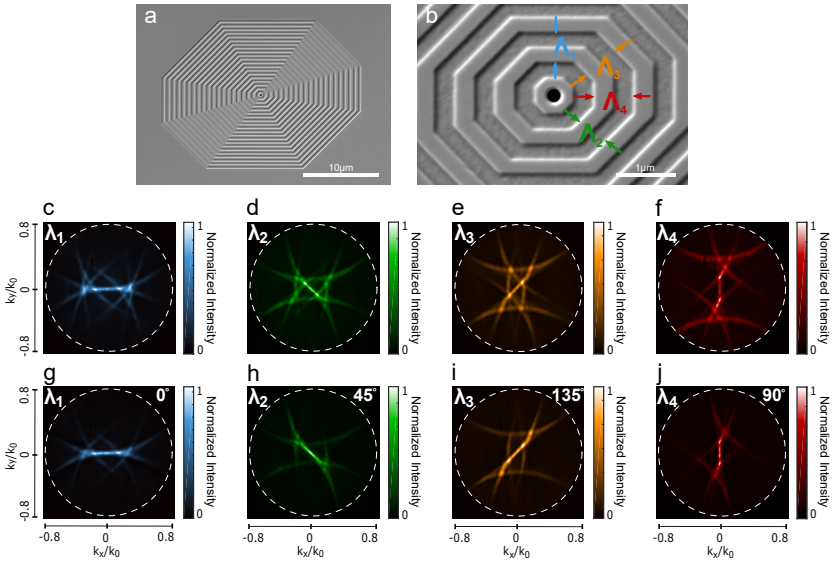

Figure 2.7 – (a) and (b) Scanning electron micrographs at different magnifications of an octagonal antenna ($\Lambda_1 = 462$ nm, $\Lambda_2 = 515$ nm, $\Lambda_3 = 570$ nm, and $\Lambda_4 = 628$ nm) patterned on single-crystalline Ag film. (c-f) k-space maps for the antenna in (a,b) obtained under unpolarized excitation at different wavelengths ($\lambda_1 = 500$ nm, $\lambda_2 = 550$ nm, $\lambda_3 = 600$ nm, and $\lambda_4 = 650$ nm). (g-j) Polarization-resolved k-space maps obtained from (c-f) using an output analyzer. Reprinted with permission from [89], `https://pubs.acs.org/doi/abs/10.1021/acsnano.7b05269`. Further permissions related to the material excerpted should be directed to ACS.

of light in which spectral information is encoded in the polarization state of the beam. To demultiplex and isolate the directional scattering of the resonant condition in the out-of-plane direction, we polarization-resolve the light collected with a low numerical aperture (NA = 0.06) objective, that is sensitive only to a small cone of out-scattering angles (∼6.8°) (see schematic in Figure 2.8a). This angular selection is necessary to isolate a unique polarization for each color, filtering out the non-resonant arcs that

are scattered out at larger angles from their corresponding non-resonant axes (see k-space maps in Figure 2.4 and Figure 2.6). The polarization-

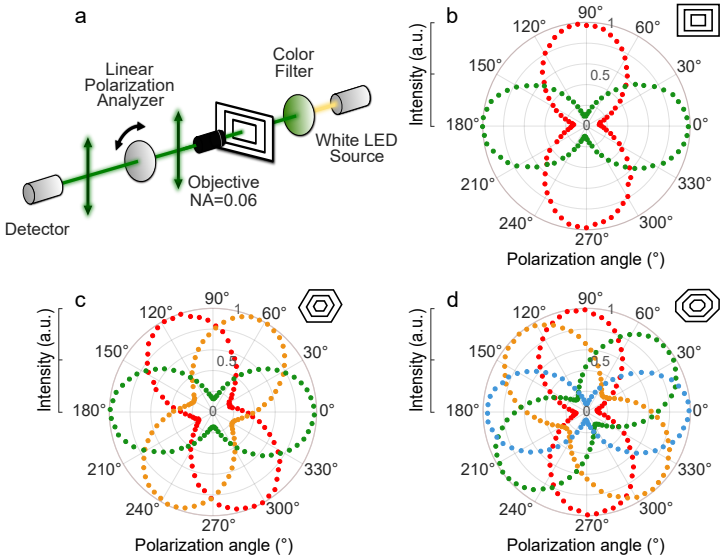

Figure 2.8 – Polarization-resolved spectroscopy. (a) Schematic of the detection scheme. A color filter is used to generate quasi-monochromatic light from a white-light source. Transmittance is collected using a numerical aperture of 0.06 and analyzed with a rotating linear polarizer. (b-d) Normalized transmitted intensity is measured as a function of polarization angle for different excitation wavelengths (red markers for $\lambda = 650 \pm 5$ nm, orange for $\lambda = 600 \pm 5$ nm, green for $\lambda = 550 \pm 5$ nm, and blue for $\lambda = 500 \pm 5$ nm) sent through a (b) rectangular, (c) hexagonal, and (d) octagonal multiresonant antenna. Reprinted with permission from [89], `https://pubs.acs.org/doi/abs/10.1021/acsnano.7b05269`. Further permissions related to the material excerpted should be directed to ACS.

dependent response of our multiresonant structures to different excitation wavelengths is reported in polar coordinates in Figure 2.8b-d. In the case of the rectangular antenna, the highest transmitted intensity for two

different excitation wavelengths (red and green) is found at orthogonal analyzer angles, as predicted by the k-space maps. In the case of a hexagonal structure, these maxima occur for angles shifted by 60°. To extend the multiresonant concept further, we also present the case of the octagonal configuration, in which resonances occur approximately at the expected 45° separation. Slight shifts in the estimated polarization angles can arise when the number of periodicities is significantly increased due to cross-talk of polarization components located at each individual axis. Generally, the measured behavior closely follows the numerical predictions obtained in simulations (see Section 2.2.3).

Spectral transmission measurements of rectangular, hexagonal, and octagonal bull's eye structures were also performed and are shown in Appendix A.

2.4 Fluorescence multiplexing

2.4.1 Coupling to cQDs

To demonstrate how our multiresonant antennas can be used to structure the emission of fluorescent labels, we place colloidal-quantum-dot emitters inside the central aperture. Colloidal quantum dots (cQDs) are commonly used in biological fluorescent labeling thanks to their size-tunable spectral properties, as well as bright and photostable emission [64]. Importantly, they exhibit narrow emission linewidths, making them particularly suited for color-selective sensing. Here, we use a size series of CdSe/CdZnS core/shell cQDs with emission colors in the green (λ_{em} = 565 nm), orange (λ_{em}= 600 nm), and red (λ_{em} = 635 nm), for which the emission spectra are shown in Figure 2.9a. Each antenna is coated with a single emitter color by drop-casting the QDs from dispersion.

We excite the aperture from the unpatterned backside of our antenna using a 488 nm continuous wave (CW) laser (OBIS, Coherent; see schematics in Figure 2.9d,e). The subwavelength nature of the central nanoaperture and the presence of the optically thick Ag film around it, allows for spatially selective excitation of the emitters inside the aperture [37, 47, 65]. The fluorescence is collected with a low-NA objective (NA = 0.06) from the

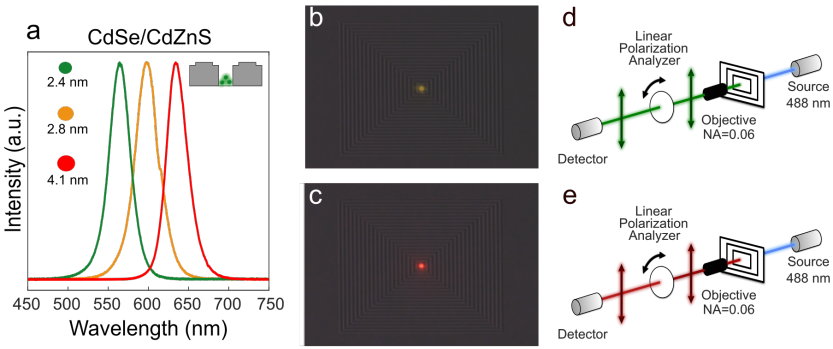

Figure 2.9 – Colloidal CdSe/CdZnS quantum dots (cQDs) are coupled to the aperture of the multiresonant antennas. (a) Normalized emission spectra of cQDs with core sizes of 2.4, 2.8, and 4.1 nm. (b, c) Fluorescence microscopy images of (b) green-emitting and (c) red-emitting quantum-dots coupled to a rectangular bull's-eye antenna superimposed on a scanning electron micrograph of the uncoated rectangular antenna. (d, e) Schematic of the low-NA fluorescence measurement setup. Reprinted with permission from [89], `https://pubs.acs.org/doi/abs/10.1021/acsnano.7b05269`. Further permissions related to the material excerpted should be directed to ACS.

corrugated side of the structure. In Figure 2.10a we show the polarization-dependent fluorescent intensity collected from a set of two rectangular structures, each coated with one of the two resonant emission-color cQDs, in this case red and green. The expected orthogonal polarization for the two colors is indeed obtained. Similarly, Figure 2.10b shows the same measurement for a set of three hexagonal antennas, in this case coated with cQDs of either green, orange, or red emission. From the corresponding measured fluorescence k-space maps for hexagonal antennas that are shown in Figure 2.10c-g, we can notice that, compared to the transmission measurements of Figure 2.8, the larger QD linewidth and smaller difference in the periodicities of the design ($\Lambda_1 = 522$ nm and $\Lambda_2 = 602$ nm due to the reduced spectral separation of the QD emission) introduce a slight broadening and overlap of the different sets of arcs

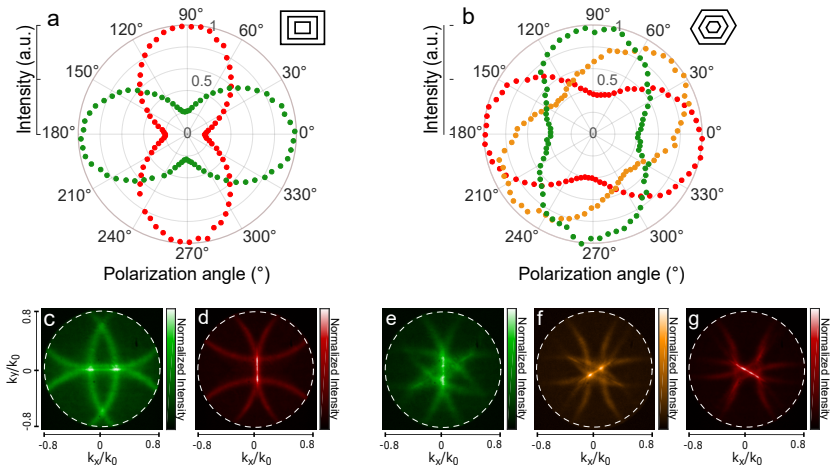

Figure 2.10 – (a, b) Fluorescence intensity recorded using a NA = 0.06 as a function of polarization angle for (a) green and red cQDs on rectangular bull's eyes and (b) green, orange, and red cQDs on hexagonal bull's eyes. (c-g) Complete fluorescence k-space maps corresponding to (c,d) the measurements in (a) and (e-g) the measurements in (b) collected using a NA = 0.8. Reprinted with permission from [89], `https://pubs.acs.org/doi/abs/10.1021/acsnano.7b05269`. Further permissions related to the material excerpted should be directed to ACS.

increasing polarization cross-talk. This requires the use of small NAs in order to select only the resonant set of arcs of a color and reject the other polarizations. Nevertheless, in applications where high sensitivity is required, like single QD detection, higher numerical apertures can also be used to collect the structured light at the cost of a reduced selectivity (see Section 2.4.1.1 for a more detailed discussion). Despite the occurrence of increased cross-talk in the hexagonal structure, causing a reduced on-off ratio in the polarization dependence and a slight shift from the expected 60° separation, the three colors obtain clearly distinct polarization angles (Figure 2.10b). This demonstrates the ability of our antenna platform to structure the fluorescence of coupled emitters even in the hexagonal case.

These characteristics of the fluorescent beam allow us to resolve spectral components using linear polarization analysis and simplified detection schemes.

2.4.1.1 Selectivity and efficiency

To achieve high spectral selectivity in our polarization-resolved spectroscopy scheme it is necessary that, for every scattered color, only a unique polarization orientation is collected within the acceptance cone determined by the NA of the objective. Therefore, different polarization components originating from non-resonant axes need to be scattered into larger far-field angles, outside the acceptance cone. By minimizing the collection cone of the objective (NA = 0.06, corresponding to a collection cone of 6.8°), we apply narrowband angular filtering of scattered emission to minimize non-resonant contributions to the signal. Naturally, applying such strict angular filtering does reduce the collection efficiency of the emission. In the following, we discuss the selectivity–sensitivity tradeoff of our polarization-resolved spectroscopy scheme. To illustrate the influence of the choice of NA, Figure 2.11 shows k-space maps (NA = 0.8) with white circles indicating the size of the collection cone for objectives with different NAs. The k-space maps in Figure 2.11a and b display the out-scattering pattern for typical rectangular structures resonant with red light for both the transmission case (Figure 2.11a, 10 nm bandwidth) and the cQD emission case (Figure 2.11b). It is clear that an NA of 0.06 is small enough to reject the orthogonal non-resonant out-scattering. To compare the collection cone of our NA = 0.06 objective to the emission profile of our resonant out-scattered light, we plot cross-sections of Figure 2.11a and b in Figure 2.11c (see dashed lines through k-space). For light of 10 nm bandwidth transmitted through a 20 groove structure we measure a FWHM = 2.1 ± 0.1 degrees (red line in Figure 2.11c). For the broader cQD emission (Figure 2.11b), a slightly larger FWHM of ±2.8° is measured (orange line in Figure 2.11c). To quantify the collection efficiency, we integrate the intensity within the NA = 0.06 collection cone of the k-space map and compare it to the full emission profile for NA = 0.8. We find that a modest 3-5% of the emission is collected. It is important to note though, that thanks to our resonant out-coupling this collection efficiency is around an order of magnitude higher than the case

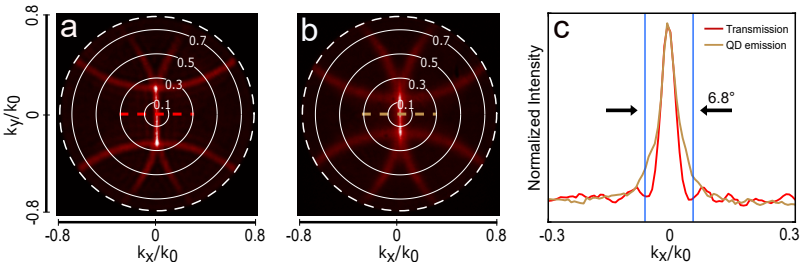

Figure 2.11 – (a),(b) k-space maps of (a) transmission of 650 ± 5 nm light through the rectangular structure of Figure 1a and (b) cQD emission of 635 nm ± 10 nm. White circles indicate the k-space area collected by objectives with increasing numerical apertures. (c) Cross-sections of the k-space maps in (a) and (b) as indicated by the dotted lines. The blue vertical lines indicate the diameter of the collection cone of an objective with NA = 0.06 (corresponding to 6.8°). Reprinted with permission from [89], `https://pubs.acs.org/doi/abs/10.1021/acsnano.7b05269`. Further permissions related to the material excerpted should be directed to ACS.

for an aperture without antenna. Therefore, despite rejecting a large part of the emission pattern through our angular filtering with a small NA, the resonant out-coupling helps to dramatically improve light collection, with a divergence well within the collection cone of the objective. In this study we have optimized for maximum selectivity, motivating our choice for the extreme case of a NA = 0.06 objective. Larger NAs can be used if higher signal intensities are required, although this inevitably goes at the cost of selectivity. To demonstrate this trade-off, Figure 2.12a,d reports the normalized polarization-dependent transmitted intensities for different numerical apertures for the case of a rectangular structure (see k-space maps in Figure 2.11b-c and e-f for green and red, respectively). The largest polarization-dependent modulation of the intensity is present for small NAs with the phase of the modulation oriented along the expected resonant axes. As the NA is increased, more of the orthogonal polarization enters the collection cone (i.e. cross-talk occurs), which reduces the modulation amplitude and starts shifting the phase away from the expected orientation. However, as long as a clear predominance of

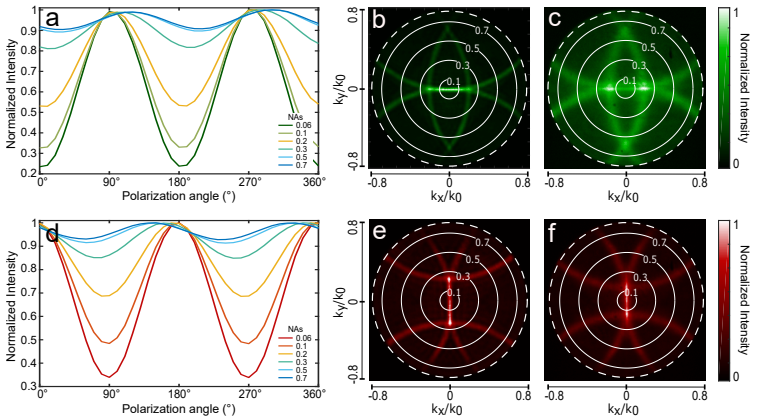

Figure 2.12 – (a),(d) Normalized intensities as a function of polarization angle for increasing NA of the collection objective for the case of transmission through a rectangular antenna illuminated with (a) 550 ± 5 nm and (d) 650 ± 5 nm light. (b),(e) Corresponding unpolarized k-space maps of the sample measured in (a),(b) and (c),(f) k-space maps for the cQD emission as measured in Figure 5. White solid lines in (b)-(f) indicate the k-space are corresponding to a collection objective with the defined NA. Reprinted with permission from [89], `https://pubs.acs.org/doi/abs/10.1021/acsnano.7b05269`. Further permissions related to the material excerpted should be directed to ACS.

intensity from the resonant axis exists, some selectivity is maintained. For the transmission case, an NA of up to 0.3 can be used to maintain a good amount of selectivity. For cQD emission, cross-talk starts to occur at slightly lower NAs, with selectivity dropping beyond NA = 0.2. This is due to the smaller difference in the patterned periodicities that have to satisfy the smaller spectral separation between the emission wavelengths of the cQDs (70 nm between $\lambda_{\mathrm{em}} = 565$, 635 nm compared to 100 nm between $\lambda_{\mathrm{transm}} = 550$, 650 nm). Efficiencies of light collection of around 15 or 20% can be reached using NA = 0.2 or 0.3.

2.4.2 Coupling to dyes

While cQDs are beneficial in terms of their narrow spectral width of emission, organic fluorophores are more commonly used as fluorescent labels, in particular in aqueous media or in biomedical applications where covalent bond formation is necessary [66]. To see whether the selectivity of our polarization multiplexing scheme suffices to distinguish the broader emission bands of a series of organic fluorophores, we use rhodamine dyes — fluorophores belonging to the family of xanthenes — with emission in the visible regime. Here, Rh-NH2, Rh-Pyr and Rh-101, provided by the Rivera-Fuentes group at ETH Zurich are used. Their emission wavelengths are 523 nm, 567 nm, and 587 nm, respectively. The emission spectra and structure of the rhodamine dyes are shown in Figure 2.14a.

To perform polarization-resolved measurements with such dyes, we need to efficiently deposit them on our plasmonic structures. Unfortunately, these molecules are dissolvable in polar solvents like water but not in apolar ones (such as hexane, in which cQDs were dispersed). This is problematic because the Ag surface is hydrophobic. Therefore, when using polar solvents, the very poor wettability and high surface tension of the dye solution prevented the molecules from filling the aperture in the multiresonant Ag structures. To resolve this, the Ag surface was functionalized with PVPA (polyvinylphosphonic acid, whose OH surface groups can provide hydrophilicity) using a deposition procedure adapted from [67]. First, an aluminium oxide protection layer of 20 nm was deposited via reactive radio frequency (RF) magnetron sputtering on the FIB'd Ag substrate. Afterwards, the film was treated for 20 min in UV-ozone and then immersed into a 2 vol % aqueous PVPA solution (Polysciences, 30% solution, molecular weight: 24,000) for 2 min at 90° C. Once taken out of the solution and dried, the substrate was kept in a pre-heated oven for 10 min at 80° C. After the hydrophilization, a 2 vol % rhodamine solution in isopropanol (Sigma, pur.: >99.7%) was drop-casted onto the treated metal film. To verify the surface functionalization, a water droplet was casted onto Ag films after the different treatment steps and the contact angle was estimated. As one can see in Figure 2.13, the contact angle θ was reduced from 90° to 0° during the hydrophilization process. In Figure 2.14, we show preliminary k-space images of Rh-Pyr

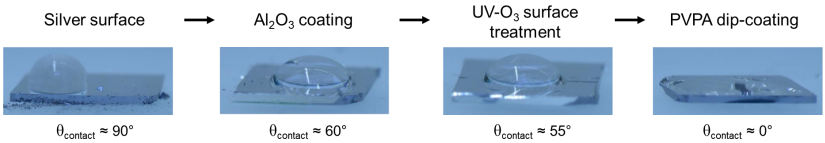

Figure 2.13 – Hydrophilization of the Ag surface via PVPA treatment leads to a significant reduction of the surface contact angle for a water droplet.

and Rh-101 structured fluorescence when deposited on a rectangular antenna with grating periodicities of $\Lambda_1 = 510$ nm and $\Lambda_2 = 635$ nm. Here, the use of antennas with only 10 periodicities instead of 20 (as used

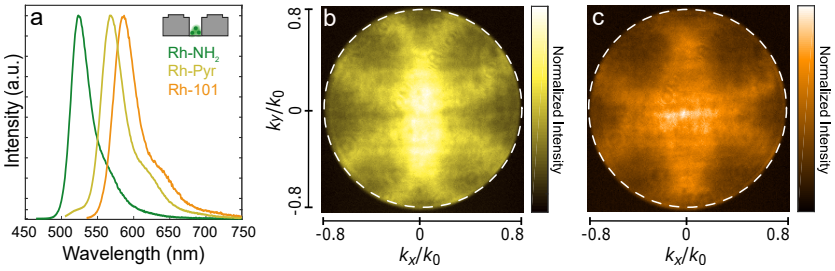

Figure 2.14 – (a) Measured fluorescence spectra of Rh-NH_2, Rh-Pyr, and Rh-101 dyes. (b) and (c) Fluorescence k-space measurements from a rectangular antenna of 10 periodicities with $\Lambda_1 = 510$ nm and $\Lambda_2 = 635$ nm coupled to Rh-Pyr (b) and Rh-101 (c) dyes.

in the rest of this chapter), together with the wider spectral distribution of the dye fluorescence compared to cQDs explains the broader FWHM of the arcs in the k-space measurements.

2.4.3 High-speed readout

In this chapter we have demonstrated the ability to resolve a certain transmitted or fluorescent color using our multiresonant structure and a polarization analyzer. Here, to simulate a possible sequencing readout platform that exploits a rectangular multiresonant antenna (see schematic in the inset of Figure 2.15a), we explore preliminary high-speed readout of alternating colors of transmitted light. For this, we employ a photo-elastic modulator (PEM, Hinds Instruments I/FS50) and a photo multiplier tube (PMT, Hamamatsu R928) connected to a lock-in amplifier (see schematic in Figure 2.15a) to detect the polarization of the light transmitted through our rectangular antenna. For this demonstration,

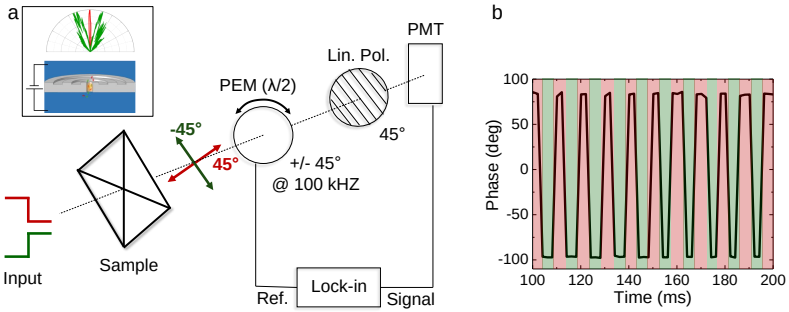

Figure 2.15 – Fast readout is demonstrated using a Photo-Elastic Modulator and a PMT-Lock-in system to detect the polarization of the outgoing light. (a) The schematic of the readout system. The inset shows a possible application in a fluid-cell type system. (b) The measured phase signal varying with the same frequency of the input modulation (marked by red and green time intervals).

we choose a rectangular antenna with $\Lambda_1 = 515$ nm and $\Lambda_2 = 635$ nm that is resonant with green and red light. An incoming source beam of alternating green (532 nm laser) and a red (660 nm laser diode) light is generated using a chopper modulated at 100 Hz. This incoming source simulates possible fluorophores of different color translocating through the aperture. The polarization-encoding nature of our antenna will then

generate a ±45°orientation in the polarization of the transmitted light with respect to the optical axis. Afterwards, the PEM can act on this light as a half-wave plate at 100 kHz while a linear polarizer at a fixed orientation of 45° will allow only one polarization to pass through and be detected by the PMT. This will enable the detection of a phase difference with respect to the reference signal which is dependent on the polarization imposed by the multiresonant antenna and, therefore, on the incident color, as measured in Figure 2.15b. This preliminary demonstration shows that with a relatively simple PEM setup, read-out can be achieved with a time resolution of up to a few ms.

2.5 Conclusions and outlook

Combining multiresonant performance with controlled directionality and straightforward design principles, multiresonant bull's-eye platforms provide opportunities for next-generation polarimetric filtering technologies. We demonstrated that these devices, capable of mapping different colors to a unique polarization state, enable spectral readout using few optical components and compact setups. Moreover, coupling nanoscale emitters to such structures, we have been able to efficiently tailor directionality and polarization of fluorescent emission. Through its built-in nano-cuvette aperture, the presented antenna platform provides opportunities for next-generation sensing technologies towards single-emitter resolution [68]. Specifically, polarization multiplexing of spectral information, as demonstrated through our polarization-resolved spectroscopy scheme, enables new concepts in molecular sequencing analysis. Polarization-resolved spectroscopy may benefit from high-speed signal modulation using, for example, photo-elastic modulators — a strategy that may enable faster detection schemes in fluorescence-based sequencing techniques [65]. Moreover, the high polarization dependence of our structure can add new functionalities to existing sequencing methods as well as be employed for dynamic color tuning [69] or to generate multi-color or holographic on-chip sources [70]. In a further optimization and investigation of such structures and their polarimetric properties, other parameters like the influence of the hole shape can be investigated. Different works have, in fact, introduced designs of nanoapertures in the form of rectangles

or ovals where the polarization properties of the transmitted light can acquire a more substantial polarization dependence that can be use for further tuning of the spectral response. Moreover, additional works have introduced apertures with different lengths in the x and y direction that can give rise to a multiresonant behaviour [71]. These types of apertures could also be combined with our geometrical variation of the periodicity for further tunability.

Chapter 3

Polarization multiplexing of fluorescent emission using multiresonant plasmonic nanoaperture arrays*

Nanoscale apertures arranged in recurring patterns in an otherwise opaque metal film can exhibit strong plasmonic effects leading to extraordinary optical transmission. This allows the amount of light of a particular wavelength transmitted through the film to be increased, while the light in- and out-coupling can also be angularly shaped, making these so-called "plasmonic hole arrays" easily tunable multiple-aperture nanoantennas. Similar to the design principles introduced in Chapter 2, we extend the concept of multiresonant antennas to plasmonic hole arrays, by breaking the symmetry of classical hole array structures. Compared to the bull's-eye case where one single aperture is present, higher transmitted intensities can be achieved, enabling easier integration (e.g. in microfluidic devices). By coupling these multiresonant antennas with cQDs, we show polarization-resolved identification of fluorescent colors and work towards full spectral reconstruction.

*This chapter is based on the following publication:
De Leo, E.*; Köpfli, S.*; Winkler, J.; Norris, D. J.; Prins, F. (*in preparation*)

3.1 Introduction

Roughened plasmonic films and nanoparticles can strongly enhance the signal coming from molecules placed closeby [72, 73]. This effect is a result of the strong localized electromagnetic hot-spots that plasmonic structures can generate [74]. Applications like surface-enhanced raman scattering (SERS) or detection of fluorescent labels have widely exploited this effect to improve detection and sensitivity in miniaturized devices [73, 75]. For analytical applications though, the development of nanofabrication and nanoengineering was essential to realize reproducible and highly ordered structures such as films with aperture or nanoparticle arrays. These arrangements can be engineered to provide tunable spectral and directional properties that can lead to better sensitivities [76–78]. Tiny holes smaller than half the wavelength of light can show unusual behaviors in their interaction with electromagnetic waves [10, 79]. An example are the single-aperture structures introduced in Chapter 2 which can provide enhanced, directional- and polarization-dependent outcoupling. These antennas, despite being able to probe molecules within a single diffraction-limited volume and having great potential in sensing techniques like real-time DNA sequencing [65], are able to achieve only limited transmitted intensities. If these apertures are, instead, periodically arranged, they can function as plasmonic nanoantennas, giving rise to extraordinary optical transmission (EOT, see Section 1.5) through an otherwise opaque metal film. These hole arrays can be structured to tailor the reflection and transmission of light using large-area nanopatterning techniques, allowing them to function as cheap spectral filters for broadband light sources [80]. In addition, reduced background signal that creates high contrast between the opaque film and the aperture, and confined detection volumes have led to a wide exploration of plasmonic hole arrays in sensing applications, including label-free optical biosensing [81–83]. Since fluorescent labels are also widely used for biological applications, by coupling fluorescent markers to plasmonic nanoantennas it is possible to not only enhance the collected signal [79] but also to control directionality and polarization of the outcoupled light. In plasmonic hole arrays, given the presence of a high number of subwavelength apertures, higher signals can be achieved in fluorescence detection.

In this chapter, we introduce a multiresonant plasmonic hole array antenna design that allows one to distinguish between different spectral features. While in Chapter 2 EOT multiresonant properties were obtained by modifying the periodicity of corrugations around a central aperture, here they are tuned by varying the hole array periodicity along the different axes of the structure [see Eq. (1.20)]. After the introduction of the described design concept and fabrication in Section 3.2, we will characterize the optical response of the structures in Section 3.3 and show how they enable EOT of multiple colors simultaneously. Since each color will be predominantly transmitted with a specific polarization orientation, via the analysis of the transmitted intensity as a function of polarization angle, we can recover a narrow-band input wavelength or generate a wide range of colors using a broadband light source (Section 3.4). As a demonstration of this working principle, in Section 3.5 quantum-dot fluorescent emitters are coupled to the hole-array structure to generate directional and polarized fluorescence. This allows to distinguish among emitters of different colors. Beyond differentiating among different emitted colors, such resonance-rich structures can be used to achieve full spectral reconstruction of an incident signal. In a preliminary demonstration, in Section 3.6 we use oblique hole arrays and exploit their polarization-dependent transmission to reconstruct quasi-monochromatic input spectra.

3.2 Design and fabrication

3.2.1 Design concept

Since the first demonstration of extraordinary optical transmission [10], thin plasmonic films perforated with subwavelength hole arrays have been extensively studied to miniaturize color filters and allow integration with imaging cameras and spectroscopic devices [84].

The hole arrangement acts as a periodic grating, making spectral response easily tunable by modifying the periodicity of the array following the condition:

$$k_{\mathrm{SPP}} = k_{\mathrm{inc}} + G \tag{3.1}$$

where k_{SPP} is the momentum of the surface plasmon, k_{inc} is the in-plane momentum of the incoming free-space light, and $G = 2\pi/\Lambda$ is the additional momentum introduced by the grating.

Previously demonstrated hole-array structures consisting of square or hexagonal arrangements, can generate sharp transmission-peak features tunable over a large spectral range (from UV to infrared). The response of such symmetric structures is said to be polarization independent [85]. Nevertheless, polarization can be used to introduce a further degree of freedom in controlling the structure's spectral response. For example, different types of hole shapes have led to a strong polarization response of the transmitted spectrum [86]. In many applications that require one to distinguish between different spectral features, structures that can address and enhance the signal of more than one color are necessary. In particular, if different spectral features are linked to specific polarization orientations, this can allow us to individually address a specific resonant wavelength or fluorescent color using polarization [87–89]. By extending the polygonal design concept introduced in Section 2.2.1 to the single-resonance hole-array structures made up of equal periodicities along the different axes, we modify the hole periodicity and transform a square array into a rectangular arrangement. Similarly, we distort a hexagonal building block into an oblique one as shown in Figure 3.2. While resonances due to higher diffraction orders (as is the case of Λ_3 for the oblique configuration) can introduce additional resonances, more than three resonances in the visible regime are more difficult to achieve for hole-array structures compared to bull's-eyes given the more rigid design constraints.

3.2.2 Template stripping of silver films

The fabrication of our multicolor hole array antennas exploits the template stripping method [90] of silver films. Template stripping combined with high evaporation rates allows for high-purity, low-surface-roughness metal surfaces [91]. In the template stripping process, the desired nanopatterns are etched into a silicon template using standard optimized silicon-technology processes. Subsequently, a thin film of noble metal is deposited using a thin-film deposition technique (e.g. evaporation or sputtering)

and finally, the film is peeled off the template with the use of an epoxy and a backing substrate.

The process used for our multiresonant hole arrays is schematically represented in Figure 3.1. In a first step, hole-array patterns are etched into a silicon template using e-beam lithography and HBr etching procedures. An optically thick Ag film of 200 nm is then deposited on the Si template using thermal evaporation at a high deposition rate of 25 Å/sec. During evaporation, the subwavelength holes present in the template are reproduced in the Ag film since, due to the higher depth of the holes compared to the evaporated Ag film, a non-continuous film is formed. To perform transmission measurements through the structures, the deposited film was peeled off the non-transparent silicon template using a UV-curable epoxy onto a glass slide such that the smooth interface in contact with the template is revealed. In Figure 3.2a,b we present SEM images of the

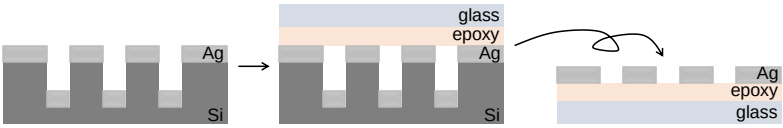

Figure 3.1 – Template stripping process for the fabrication of Ag hole arrays. In a first step, after patterning of the Si template using e-beam lithography and HBr etching, the Ag film is deposited via thermal evaporation. In the following step, UV-curable epoxy and a glass backing layer are deposited onto the Ag film. In a last step, once the epoxy curing is completed, the film is peeled off from the template and the smooth Ag surface is revealed.

fabricated "regular" single-resonant hole arrays, where the periodicity Λ is the same along the different axes. Figure 3.2a shows a square hole array and Figure 3.2b a hexagonal one. In Figure 3.2c,d we show the fabricated multiresonant rectangular and oblique structures. The rectangular hole array is realized with two different periodicities, the periodicity Λ_1 in the x-direction and the periodicity Λ_2 in the y-direction. For the oblique case, a triangular building block having three different distances (Λ_1, Λ_2, and Λ_3) between adjacent holes is constructed.

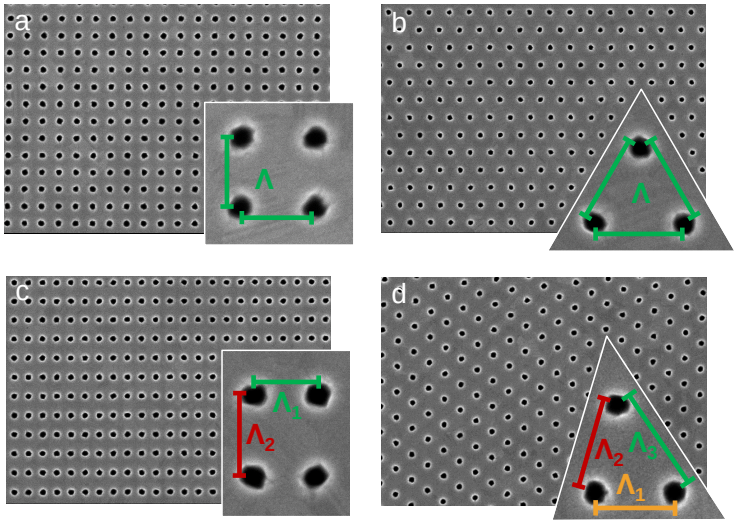

Figure 3.2 – Scanning electron micrographs of the template-stripped hole-array structures. Insets show, with a higher magnification, the building blocks corresponding to a (a) square array with $\Lambda = 300$ nm, (b) hexagonal array with $\Lambda = 350$ nm, (c) rectangular array with $\Lambda_1 = 300$ nm and $\Lambda_2 = 375$ nm, and (d) oblique array with $\Lambda_1 = 375$ nm, $\Lambda_2 = 420$ nm, and $\Lambda_3 = 495$ nm.

3.3 Characterization

3.3.1 Dispersed k-space and polarized-transmission measurements

To characterize the response of the hole array, a transmission-measurement setup similar to the one described in Section 2.3.1 is used. Figure 3.3a-d show transmission measurements through hole-array structures. The arrays are illuminated with a fiber-coupled halogen broadband source through an objective (NA = 0.6) and the transmitted light is collected using a high NA (NA = 0.8) objective (as in Figure 2.3). During transmis-

sion measurements, two interfaces where surface plasmons can propagate are present: the Ag-epoxy-glass interface from the bottom side of the metallic film and the Ag-air interface on the top-side of the fabricated structure. The surface plasmons would therefore experience two different effective refractive indices when they are propagating on the two different interfaces giving rise to an optical response with many spectral features. In order to obtain a spectrally-simplified system, on the air side of the film, we create a uniform refractive index environment by covering the array with a film of epoxy or oil whose refractive indexes closely match the one of the underlying substrate ($n_{\text{sub}} \sim 1.6$). To characterize the transmission properties of the index-matched hole arrays, we perform k-space measurements dispersed along $k_x = 0$, which corresponds to one of the resonant axes of the structure. In Figure 3.3e,f we show the measured transmitted intensity for regular hole arrays as a function of the in-plane momentum in the y-direction k_y and wavelength. Dispersion lines characteristic of diffracted orders due to the period arrangement of the lattice are observed. We expand Eq. (3.1) by considering possible variation of periodicity along more than two axes:

$$k_{\text{SPP}} = |\boldsymbol{k}_0 \sin\theta \pm \sum_{i=1}^{n} m_i \frac{2\pi}{\Lambda_i} \hat{\boldsymbol{e}}_i| \tag{3.2}$$

where $|\boldsymbol{k}_0| = 2\pi/\lambda$, θ is the angle of incidence, i are the different axes of the structure, m_i their respective diffraction order, Λ_i the periodicity and $\hat{\boldsymbol{e}}_i$ the versor of the i^{th} axis. While this equation gives a first estimation on the spectral transmissive behavior of our arrays, we use an extended coupled-oscillator model that allows to retrieve a more complete photonic band structure that includes splitting of modes due to directional surface plasmon scattering rates [92]. The results of this analysis are shown in Figure 3.3a-d as white dotted lines superimposed on the measured data. For details on the used model see Appendix B. By taking a slice at $k_y/k_0 = 0$, which corresponds to a beaming condition in the direction normal to the structure surface, it is possible to verify in Figure 3.3e,f that the "regular" structures give rise to a single-spectral transmission feature around 570 nm. In the case of rectangular and oblique structures, additional features

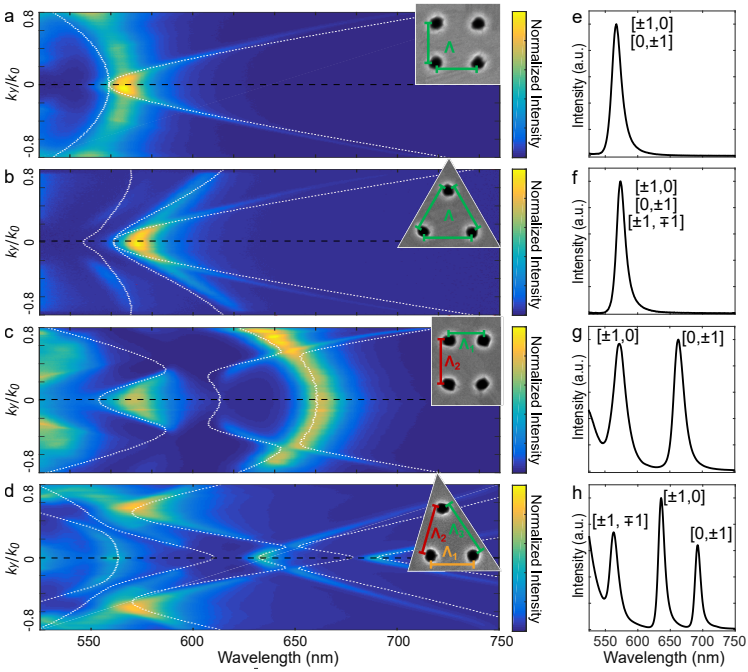

Figure 3.3 – Optical characterization of different hole-array structures. (a-d) Dispersed k-space measurements for the corresponding structures shown in Figure 3.2 where the axis with the shortest periodicity is aligned to the x-direction. White dotted lines represent the calculated modes. (e-h) The spectral response of the films under beaming condition [extrapolated for $k_y/k_0 = 0$, black dashed line of (a-d)] shows the classical single resonant response for (e,f) and a multiresonant spectrum for (g-h).

are present in the dispersion diagram and can be assigned to modes resonant with axes of different periodicities and the coupling between such modes. Line traces along the $k_y/k_0 = 0$ condition show now more than one spectral resonance, in particular, a two-peak resonance for the rectangular case and a three-peak resonance for the hexagonal case as seen in Figure 3.3g,h. This demonstrates that by engineering the array

periodicities, we can achieve beaming transmission of multiple spectrally separated resonances, corresponding to the respective different axes in the structures.

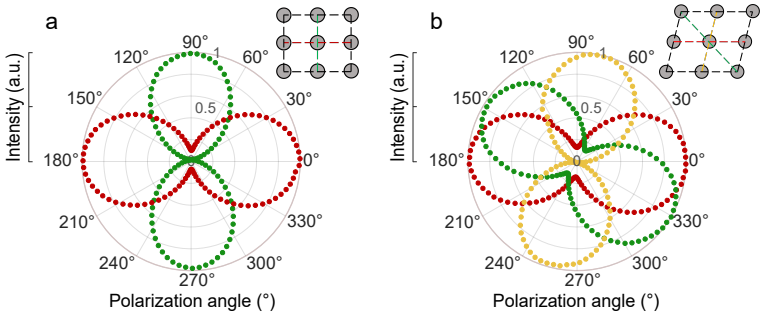

Figure 3.4 – Polarization-dependent transmission of resonant wavelengths for (a) a rectangular structure with two periodicities $\Lambda_1 = 275$ nm and $\Lambda_2 = 325$ nm and (b) an oblique structure with periodicities $\Lambda_1 = 325$ nm, $\Lambda_2 = 375$ nm, and $\Lambda_3 = 430$ nm. The colors correspond to the beaming wavelengths ($\lambda_1 = 550 \pm 5$ nm and $\lambda_2 = 625 \pm 5$ nm for the rectangular array and $\lambda_1 = 525 \pm 5$ nm, $\lambda_2 = 580 \pm 5$ nm, and $\lambda_3 = 635 \pm 5$ nm for the hexagonal array).

Additionally to its multiresonant functionality, a fundamental advantage of the introduced irregular hole array building block is that each resonant color can be mapped to a specific polarization orientation. To quantify this polarization dependence, we collect the amount of transmitted light for each color as a function of polarization angle by introducing a linear polarization analyzer at the back focal plane of the collection objective. Figure 3.4 shows the polarization-dependent transmitted intensity at the resonant wavelengths of 550 and 625 ± 5 nm for a rectangular hole array and of 525, 580, and 635 ± 5 nm for an oblique hole array. The use of a low-numerical-aperture objective of NA = 0.06 allows the isolation of only small $k_{\parallel}$ vectors that correspond to the beaming conditions. In Figure 3.4a, maximum intensity of green light is transmitted for a polarizer angle of 90° while red light achieves a maximum intensity for

the orthogonal polarization angle. This is consistent with the geometry of the structure's building block where the two different periodicities are arranged orthogonally to each other. Similarly, in the case of the oblique structure presented in the inset of Figure 3.4b, the polar map shows maxima around the angles of orientation of the triangular building block. Therefore, in both cases, the different transmitted colors acquire a predominant polarization as opposed to the case of the conventional hole-array structures.

3.4 Polarization-based color tunability

Tunability of the spectral position of the resonant wavelengths can be achieved with high degree of freedom by varying the periodicity along each axis independently as well as the hole size. Figure 3.5a shows bright field transmission images of a series of rectangular hole arrays whose periodicity of the x-axis increases in the x-direction while the periodicity of the y-axis increases in the y-direction. The increments happen in 15 nm steps. The hole size is also varied to keep the effective refractive index constant. If the structures are illuminated with a halogen broadband source and a linear polarizer is introduced before the collection CCD camera, only the color of one resonant axis (x or y) is transmitted. For example, by rotating the linear polarization analyzer to 90°, the colors belonging to the x-axis will be transmitted. When the polarizer is oriented at 0° the colors resonant with the y-axis will be enhanced giving rise to the inverted color distribution. The tunability within one array can be even higher for the case of oblique hole arrays. In Figure 3.5b we show that the same polarization-based concept can be applied to tune the color transmitted by oblique hole arrays. Each line of the sample is made up with one specific oblique configuration (see caption of Figure 3.5). Along one line, the same hole array is repeated 19 times but with a clockwise rotation of 10° with respect to the previous array. This ensures that when we probe the arrays with one fixed polarization, we can capture all the colors that can be generated by one array if a polarization analyzer would be rotated. In fact, when a broadband unpolarized source is used to excite the structures, a uniform color is observed throughout one line (meaning that no orientation-dependent transmission is present, Figure 3.5d). If

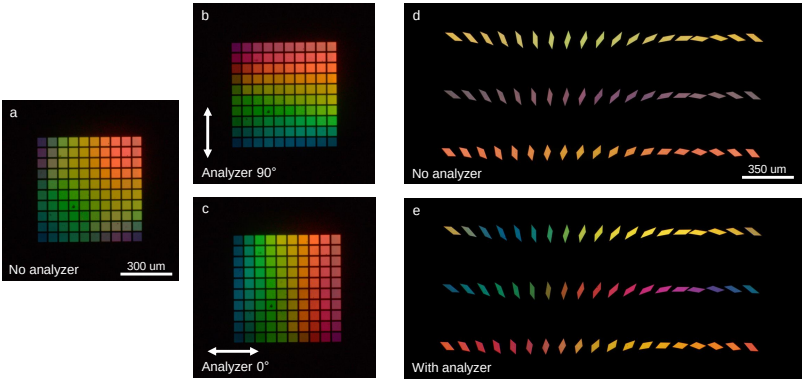

Figure 3.5 – Microscopy images of white-light transmission through different multiresonant plasmonic hole arrays. (a-c) 10 x 10 grid of different rectangular hole arrays, each array is 50 by 50 µm in size while periodicities are varied in steps of 15 nm in the x- and y-direction from one array to the next. The ratio of metal film to hole is kept constant. (a) Transmission without any polarizer and (b,c) when a linear polarizer aligned to the x- and y-direction respectively is introduced. (d,e) Three different oblique arrays are arranged on three different lines. For each line, one hole array is present and duplicated 19 times, with each subsequent replica rotated by 10° compared to the previous one. (d) Trasmission image without an analyser and (e) with a fixed analyzer position.

a linear polarizer is instead introduced, the color transmitted through the array will depend on the relative intensity and spectral mixing of the three resonant peaks as can be seen in Figure 3.5e. Due to cross-talk between different polarization components, it is not possible to select one axis/color individually. Therefore, by analyzing the transmitted light with a linear polarizer and due to the presence of mixing among the colors, one single oblique hole array can be designed to transmit a wide range of colors.

3.5 Fluorescence multiplexing of cQD emission

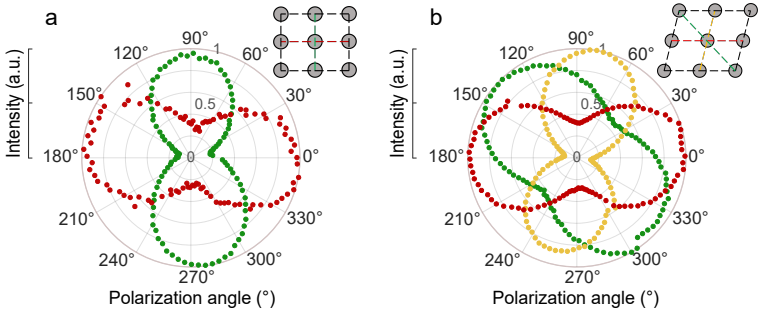

Figure 3.6 – Fluorescence intensity from cQDs coupled to multiresonant hole arrays recorded as a function of linear polarization analyzer angle. Polarization-dependent fluorescence intensity from (a) green (peak emission $\lambda_1 = 553$ nm) and red (peak emission $\lambda_2 = 625$) cQDs coupled to a rectangular hole array ($\Lambda_1 = 275$ nm and $\Lambda_2 = 325$ nm). (b) green ($\lambda_1 = 525$), orange ($\lambda_2 = 588$ nm), and red ($\lambda_3 = 636$ nm) cQDs coupled to an oblique lattice ($\Lambda_1 = 345$ nm, $\Lambda_2 = 375$ nm, and $\Lambda_3 = 460$ nm).

To perform polarization-resolved spectroscopy with such structures, we prepare dispersions of cQDs in oil and deposit it on the multiresonant hole arrays as done for multiresonant bull's eyes in Chapter 2. Using the same antennas of Figure 3.4, we use high energy excitation and the setup described in Section 2.4 to measure the fluorescence signal as a function of polarizer angles for different cQD dispersions (i.e. different colors). In analogy to the multiresonant bull's-eye case, in Figure 3.6a we show the results for a rectangular antenna coupled to green and red cQDs, and in Figure 3.6b we show the case of the hexagonal antenna and three different cQD colors.

3.6 Polarization-resolved spectroscopy

The demonstrated fluorescence multiplexing allows to distinguish among different colors (i.e. whether a blue, green, or red emitter is present) but in many applications it is desirable to obtain detailed information about the spectral shape of the analyte (that could be defined as its molecular fingerprint). Efforts in realizing miniaturized spectrometers [93] that can also allow for real-time sensing [94] usually exploit spatial multiplexing where different areas of a metasurface aim to detect different spectral regions. Nevertheless, polarization properties can be introduced to provide an additional probing degree of freedom [95]. By exploiting the richness in the polarization-dependent spectral features of the oblique structure, we can look into techniques for spectral reconstruction of an incoming signal. Using this structure, in a preliminary demonstration, we reconstruct quasi-monochromatic spectral features and will work towards the realization of a miniaturized and lens-free spectrometer. First, a measurement of the polarization-dependent spectral intensity transmitted through the array is measured using a broadband white-light as excitation source. This polarization-dependent spectral transmissivity map, which is shown in Figure 3.7a, characterizes completely the polarization-dependent transmissive behavior of the array such that the final measured transmission intensity is linked to the incoming spectrum as:

$$Transmitted\ intensity\ (\theta) = Map\ (\theta, \lambda) \times Spectrum\ (\lambda) \qquad (3.3)$$

where θ is the polarization angle. In principle, any quasi-monochromatic spectrum transmitted through the multiresonant hole array will result in a unique spectrally- and polarization(θ)-dependent intensity pattern of transmitted light. From this recorded intensity map, the initial spectral distribution can be reconstructed solving Eq. (3.3), as long as the problem is defined by a full-rank matrix. An ill-defined system, e.g. due to measurement errors, can still be solved by a linear least squares method. To demonstrate spectral reconstruction, we place different bandpass filters (Thorlabs) in the optical path before the hole array structure such that the broadband light source is modified to a quasi-monochromatic source.

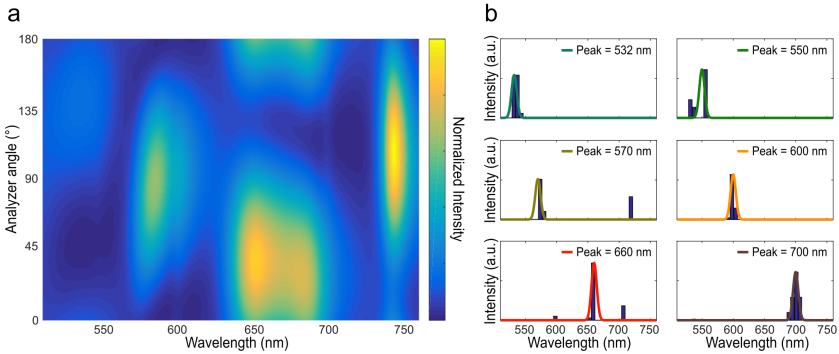

Figure 3.7 – Polarization-resolved spectroscopy. (a) Recorded map of transmission through an hexagonal antenna as a function of analyzer angle. (b) Reconstructed spectra of bandpass filters with different peak wavelengths and FWHM = 10 nm.

Measuring the transmitted light intensity as a function of polarizer angle with such input, it is now possible to retrieve the spectral information given the previous characterization of the hole array (Figure 3.7a). Preliminary measurement results are shown in Figure 3.7b, where six types of different filters in the spectral range from 520 to 720 nm were analyzed and successfully reconstructed in their peak position and peak width. While improvements in the system design, resolution, and reconstruction algorithms are still necessary, these preliminary results show that an array with only few resonances has, nevertheless, the potential to perform spectral reconstruction across a relatively broad spectral range.

3.7 Conclusions and outlook

The optical response of classical hole-array structures is limited to only one beaming resonance which is defined by the periodicity of the lattice (along two directions in the case of a square hole array or along three directions in the case of an hexagonal hole array). Despite enhanced fluorescence of a particular emitter color can be achieved using these configurations [79],

to perform multi-analyte biosensing, a plasmonic surface that supports multiple resonances that can be individually tuned is necessary [49–51, 89, 94, 96]. By varying the periodicity along the different axes of the lattice, we have shown that it is possible to increase the number of resonant wavelengths. Moreover, due to the peculiar polarization dependence of each resonance, mapping the polarized transmitted light allows to sort the wavelength of a quasi-monochromatic source used to excite the multiresonant hole array. Quantum dots in dispersion can be coupled to the multiresonant antenna to obtain polarization dependent directional emission. This allows to sort different fluorescent colors using a linear polarization analyzer. The higher intensity of the measured light compared to the single aperture structure of Chapter 2 and the wide-area patterning allows for integration in microfluidic devices for possible sorting techniques or analyte concentrations measurements. Moreover, since the resonant wavelengths are transmitted in the direction normal to the surface, the use of additional optical elements such as lenses, slits or irises before the signal detection on a photodiode could be unnecessary. Using a resonance-rich structure like the oblique array, we showed a preliminary demonstration towards the efforts of developing a miniaturized optics-free spectrograph device that consists only of a multiresonant hole array, a linear polarizer, and a photodiode. These versatile devices could enable absorption spectroscopy measurements or be used, for example in the context of molecular sequencing, to directly probe spectral features of emitters coupled to high-sensitivity plasmonic hole-array structures.

Chapter 4

Multispectral quantum-dot nanostructures fabricated via direct-patterning to tailor fluorescent emission*

Specific designs of nanostructured surfaces allow enhanced and directional in- and out-coupling of light for targeted wavelengths [19, 97]. Moreover, the ability to control both the polarization-dependent response of an antenna and the polarization state of the outgoing light offers an effective strategy to structure electromagnetic fields [60]. In this chapter, extending the concept of our multiresonant bull's eyes beyond the plasmonic antenna structure, we translate our design to structures made entirely out of colloidal quantum-dots [98]. Efficient Bragg scattering of the quantum-dot fluorescence yields a high degree of directional and polarization control. Our results on quantum-dot structures will be discussed in the context of polarimetric applications that may generate new forms of structured light and enable advanced concepts in spectroscopy and display applications.

*This chapter is based on the following publication:
De Leo, E.; Rossinelli, A.; Marqués-Gallego, P.; Poulikakos L. V.; Norris, D. J.; Prins, F. (*in preparation*)

4.1 Introduction

The idea of structuring, tailoring, or sculpting light fields is connected to the idea of designing their intensity, polarization, and phase [99]. Any interaction of light with matter, from conventional processes of scattering and reflection to color filtering or beam steering can be considered as a way to shape a light beam and enhance or tailor its properties. Moreover, since every interaction between light and matter can reveal new properties of both interacting parts, one of the driving forces behind the shaping of light beams is the desire to discover or generate new intriguing phenomena. For example, as seen in the previous chapters, the light coming from nanoscale emitters can launch surface waves on plasmonic materials while the plasmonic antennas can shape the optical response of such emitters. Advanced holographic beams allow for faster use of scanning microscopy, parallel exposures in laser writing, or micro-manipulation techniques [100]. Differently from plane waves or Gaussian modes that have a homogeneous polarization distribution in their transverse plane, more complicated structured modes having radial or azimuthal polarization, exhibiting phase singularities, or carrying orbital angular momentum, can be realized [101, 102]. These unconventional polarization or phase distributions can grant interesting properties and capabilities to such beams. For instance, tighter focusing can be achieved with radially polarized beams compared to other types of beams and they can also be used for excitation of special near field tips [103]. Beams that carry intrinsic (orbital) angular momentum have instead been used to transfer mechanical torque to microscopic objects [104].

The development of nanofabrication and nano-optics has allowed the realization of complex nanoscale structures that, depending on their shapes and materials can interact selectively with light that has certain characteristics or exhibits particular properties. Such nanostructures provide the ability to shape and manipulate light fields upon reflection, transmission, waveguiding, or scattering. Despite the numerous optical components like plasmonic and photonic metasurfaces that have been designed to generate complex structuring of light beams [19, 97], investigating a way to directly structure light at its source (as has been done with laser cavities [105]) could lead to more compact and versatile devices.

In particular, direct patterning of films of fluorescent material could lead to the development of a new range of nanoscale light sources with easily tunable properties like polarization, spectral definition, or directionality for a wide number of applications [98].

Colloidal quantum dots (cQDs), or semiconductor nanocrystals, are highly versatile building blocks that combine size-tunable optical properties with low-cost wet-chemical processing [106, 107]. Spectrally-narrow emission throughout the visible-near-infrared range [108] with high quantum yield (>90%) [109] has placed cQDs among the highest color-quality emitters available, while at the same time outperforming most organic emitters in terms of photo-stability [110]. A number of cQD-based display [111, 112] and lighting technologies [110, 113] have recently emerged, while backlit display systems have already entered the market [114]. With internal conversion efficiencies of cQDs approaching unity, the light-extraction efficiencies from cQD films have become the limiting factor in terms of brightness. As is inherent to such high refractive-index layers, a significant portion of the emission undergoes internal reflection and gets trapped into waveguiding modes, leading to reabsorptive losses and reduced brightness. To overcome this issue, research efforts are increasingly shifting toward the development of nanophotonic light-management strategies that improve the out-coupling from these materials.

Here we take advantage of the properties of colloidal quantum dots using them as building blocks to fabricate, in Section 4.2.1, nanoscale-patterned multiresonant antennas with a design that allows for highly directional and polarized emission, as demonstrated in Section 4.3.1 and Section 4.3.2. Moreover, in Section 4.4 we will show how their particular concentric configuration offers a way to generate multicolor light sources, while in Section 4.5 we will use them to realize structured light beams that have complex intensity and polarization distributions.

4.2 Fabrication

4.2.1 Template stripping for direct nanopatterning of colloidal quantum-dot films [†]

Direct patterning of light-emitting layers has been successfully applied to organic light-emitting polymers, for example by structuring the surface with linear or circular Bragg gratings [115, 116].

The fabrication of Bragg gratings requires high-quality sub-wavelength patterning of the surface of the light-emitting film. In organic films, Bragg gratings have been fabricated using, for example, soft lithography or stamping [115, 117, 118]. Even though cQDs profit from many of the advantages of solution processability, few methods exist to produce patterned assemblies with submicron resolution [119]. Inkjet [120] and electrohydrodynamic [121] printing techniques have been developed to produce patterned films, and are capable of achieving submicron resolution but have poor definition of taller structures. Soft lithography and stamping techniques do exist for cQD solids [112, 122], but submicron resolution is challenging. While pattern definition using electron beam lithography in combination with lift-off techniques would potentially allow for higher-resolution patterning of taller structures, not many examples are still available and matrix-embedded cQD films have the distinct disadvantage of diluted emitter concentration, which inevitably places limitations on the emission intensity.

Our fabrication method is similar to template stripping techniques used to fabricate patterned metal films and macroscale assemblies of plasmonic nanoparticles [90]. Figure 4.1a shows a schematic of the process. Patterned silicon templates were fabricated using standard e-beam lithography and reactive-ion etching techniques. Si(100) substrates of 2 x 2 cm in size were cleaned using sonication in acetone, isopropanol, and deionized (DI)

[†]This Section is based on the following publication:
Prins, F.*; Kim D. K.*; Cui J.; De Leo E.; Spiegel L. L.; McPeak K.; Norris D. J. *Nano Letters* **2016**, *17*, 1319, `https://pubs.acs.org/doi/abs/10.1021/acs.nanolett.6b03212`. Further permissions related to the material excerpted should be directed to ACS.

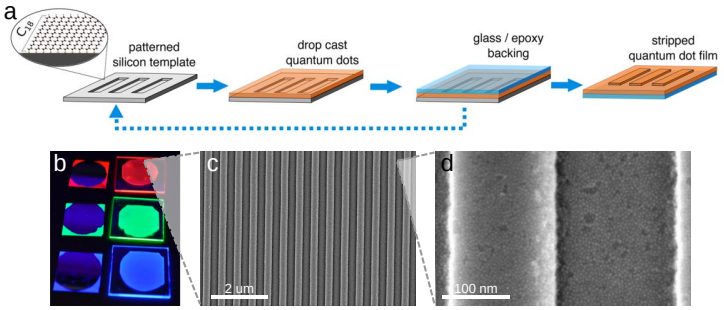

Figure 4.1 – (a) Schematic of the template-stripping technique for fabricating surface-patterned cQD films. Initially, the nanopatterned Si template is coated with an octadecyltrichlorosilane self-assembled monolayer. After covering the hydrophobic surface with cQDs via dropcasting, an adhesive layer of epoxy followed by a glass backing film is used to peel the film off the template revealing a smooth nanopatterned surface. (b) Photograph of ultraviolet-illuminated patterned films of red-, green-, and blue-emitting cQDs that were fabricated using template stripping. On the left-hand side the corresponding templates of 2x2 cm each are shown. (c,d) Scanning electron micrographs at different magnifications of linear gratings. Reprinted with permission from [98], `https://pubs.acs.org/doi/abs/10.1021/acs.nanolett.6b03212`. Further permissions related to the material excerpted should be directed to ACS.

water and prebaked at 180°C for 10 min. Substrates were coated with 200 nm PMMA (AR-P 672.03 950K) and patterns were defined using electron-beam lithography (Vistec, NFL 5). Patterns were developed using MIBK:IPA (1:2 ratio) for 2 min, followed by 1 min in fresh IPA and then 1 min under running DI water. Features 100 nm deep were etched into the Si substrate using deep-reactive-ion etching (Alcatel, AMS-200 I Speeder) at 11.25 mTorr with 60 SCCM C_4F_8, 40 SCCM SF_6, a plate power of 80 W, and an inductive-coupled-plasma (ICP) power of 1200 W. The etch rate for these settings was 8 nm/s. The PMMA mask was removed using ultrasonication in acetone, followed by an IPA rinse,

and subsequent O_2 plasma at 750 mTorr, 600 SCCM O_2, and 600 W (PVA-TePla, GIGAbatch 310 M) for 3 min. Patterned templates were cleaned using O_2 plasma (600W, 3 min) and piranha treatment (1:1 H_2O_2/H_2SO_4, 15 min). The templates were subsequently coated with a dense self-assembled monolayer (SAM) using a previously reported octadecyltrichlorosilane treatment [123, 124]. In short, after cleaning with piranha solution, the templates were submerged in DI water for 5 min, then blow dried with a N_2 gun. In a Teflon container, 150 µL of OTS, 300 µL of CCl_4, and 10 mL of bicyclohexyl were combined. A beaker of DI water was set to 170°C on a hotplate, and the silicon substrate was quickly passed over the water vapor. Immediately after the thin film of water evaporated, the sample was placed in the Teflon container with OTS for 15 min. Next, to remove non-bound OTS, the samples were thoroughly rinsed with cholorform and subsequently sonicated in a chloroform bath for 2 min. Samples were placed back in the Teflon container with OTS, rinsed and sonicated two more times to complete the process. The resulting hydrophobic surface yields a contact angle $>$ 110°.

The cQDs were then drop-cast onto the template to form a dense and continuous layer. The concentration was determined by taking the optical density of the quantum-dot dispersion with a UV-VIS spectrophotometer at the lowest energy exciton. As a first step, we realized red-emitting quantum dot films that we prepared from a cQD dispersion with an optical density of 2.0 (1 cm optical path length). Details on the synthesis of the different types of QDs used in this chapter are reported in Appendix C.3. The dispersion was prepared using a hexane:octane ratio of 9:1. Then, 35 µL of cQDs was dropcast onto the silicon substrate and allowed to dry, yielding a uniform film approximately 200 nm in thickness. In the next step, a glass backing substrate was attached to the colloidal film using an ultraviolet-curable epoxy. In a final step, the colloidal film was mechanically peeled off the template to expose the patterned surface defined by the template. The template can be cleaned for future use through ultra-sonication in chloroform for 5 min. The SAM maintains sufficient quality for 10-15 dropcasts, although best results are generally obtained with freshly prepared SAMs. The use of the high-quality self-assembled monolayer on the silicon template is essential to the success of

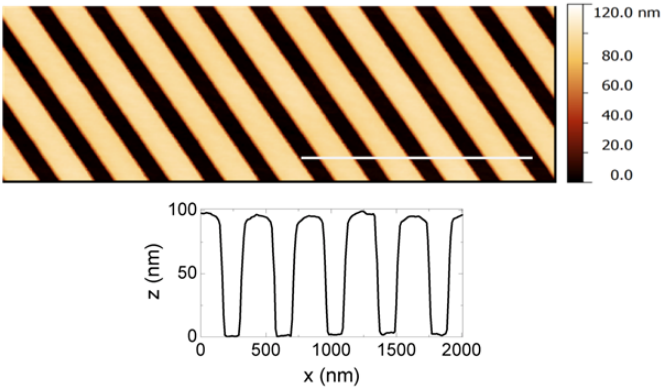

Figure 4.2 – Top: Atomic force micrograph of a cQD linear grating with 400 nm pitch. The scalebar is 1.8 μm. Bottom: line trace taken perpendicular to the same grating structure. Reprinted with permission from [98], `https://pubs.acs.org/doi/abs/10.1021/acs.nanolett.6b03212`. Further permissions related to the material excerpted should be directed to ACS.

this technique. Template stripping relies on a well-defined "weakest link" in the layer stack. Without the self-assembled monolayer, the adhesion between the cQDs and the template would be competing with the cQD-cQD adhesion in the film itself [112]. Using our technique, lateral feature sizes as small as 100 nm are achievable, while feature heights as tall as 100 nm were reproducibly obtained (see Figure 4.2).

4.3 Characterization

4.3.1 Directional emission

Bragg scattering of waveguided light leads to constructive interference of emission in the out-of-plane direction when the in-plane momentum is conserved. The angle of out-coupling (θ) with respect to the surface normal for a given emission wavelength λ_{em} and grating periodicity Λ is

governed by the Bragg condition, given by:

$$k_0 \sin\theta = \pm k_{\mathrm{wg}} \pm m k_{\mathrm{g}} = \pm \frac{2\pi n_{\mathrm{eff}}}{\lambda_{\mathrm{em}}} \pm m \frac{2\pi}{\Lambda} \tag{4.1}$$

where k_0 is the wavevector of the outcoupled light, k_{wg} is the wavevector of the waveguided light, k_{g} is the Bragg vector, n_{eff} is the effective refractive index of the waveguide mode, and m is the diffraction order. Hence, first-order diffraction allows waveguided light to scatter in the out-of-plane (θ = 0) normal direction when $\lambda_{\mathrm{em}} = \Lambda\ n_{\mathrm{eff}}$. In a grating structure, where momentum matching is satisfied for a particular direction, this results in a distinct beaming of fluorescence from the structure, as shown in Figure 4.3 for the grating with periodicity Λ = 400 nm, which appears brighter compared to the other gratings [125]. Additionally, while the first-order diffraction couples the emission out vertically, the second-order diffraction can provide feedback for the in-plane fields — a concept that has been successfully employed to construct surface-emitting Bragg lasers [117].

To look further into such directional character, we use k-space microscopy in which, as described in Chapter 2, we image the back focal plane of our collection objective onto the CCD camera. The used configuration is similar to the one showed in Figure 2.3 but, here, a 488 nm CW laser is used as source to excite the fabricated sample from the back, through the glass substrate. The patterned side of the cQD film faces the high numerical aperture collection objective (NA = 0.8). A notch filter is used in the collection path to remove the excitation beam. In Figure 4.3 we show k-space maps recorded for the linear gratings with periodicity Λ = 450, 400, and 350 nm. The bright arcs represent the k-vectors (i.e. the scattered angles) for which Eq. (4.1) is satisfied and show that emission from the structures has a very directional character. In particular, for Λ = 400 nm, the momentum condition for out-coupling is satisfied in the normal direction and indeed a stronger emitted intensity is recorded in the centre of the k-space map.

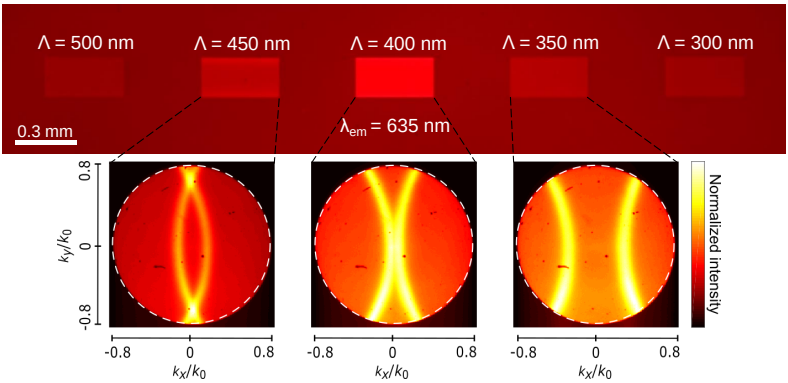

Figure 4.3 – (top) Fluorescence microscopy image of an array of linear gratings of 250 lines each on a red-emitting cQD film. The pitch of these gratings varies from $\Lambda = 550$ nm on the left, to $\Lambda = 300$ nm on the right with 50 nm decrements. (bottom) k-space maps of the recorded intensity for the three central gratings. For $\Lambda = 400$ nm, high intensity in the beaming direction (k_x/k_0 and $k_y/k_0 \sim 0$) is recorded.

4.3.2 Polarization dependence

Waveguided light acquires a predominant polarization when scattering off linear grating outcouplers (as described for plasmonic gratings in Section 2.3.1). The predominant polarization behaviour is dependent on which mode (TE or TM) is propagating in the cQD film. If we fabricate two orthogonally oriented cQD gratings and introduce a linear polarization analyzer to select the incoming and outgoing light, before our collection camera, we are able to isolate the emission coming from one grating with respect to the other one. This means that the out-coupled emitted light has acquired a specific linear polarization imposed by the grating geometry. And if we record the intensity emitted by the grating as a function of linear polarization angle, we can retrieve (as already seen for the waveguided plasmonic case in Chapter 2 and Chapter 3) a typical lobe pattern with a maximum at a specific linear polarization orientation.

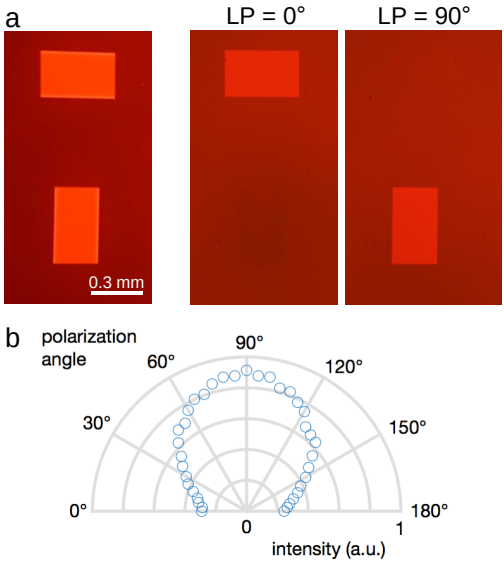

Figure 4.4 – (a) Polarization dependence of cQD linear gratings. The introduction of a linear polarizer (LP) to select the incoming and outgoing light enables one to selectively isolate the emission from one of the two orthogonally oriented gratings. (b) Mapping of the intensity of emission from a grating as a function of polarizer angle.

4.4 Tunable light sources

One of the advantages of colloidal quantum dots versatility is the possibility to create dispersions that contain more than one nanocrystal size and therefore be able to fabricate thin films with a mixture of different colors. The directional properties of the linear grating fluorescent antennas allow us to employ them as building blocks to generate multicolor light sources (Figure 4.5). Recalling our multiresonant antenna concept introduced in Chapter 2 and Chapter 3, we can use the same concentric polygonal antenna geometry, with concentric gratings that vary in periodicity along the different axes, to simultaneously enhance the outcoupling of multiple

colors. Moreover, as seen in Section 4.3.2, since the light emitted from each grating will acquire a predominant polarization, we could generate a wide range of colors using an analyzer to select the outgoing beam. In

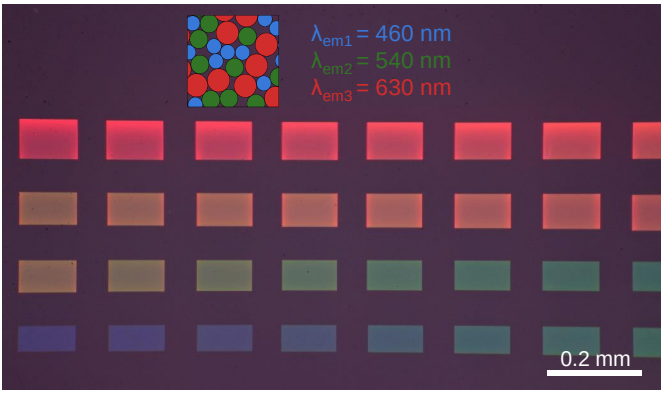

Figure 4.5 – Fluorescence image of a film of mixed blue, green, and red cQDs in which linear gratings with varying periodicities are patterned. Periodicities vary from $\Lambda = 425$ nm in the top left corner to $\Lambda = 270$ nm in the bottom left corner following a snake-like pattern. Each grating acquires a specific fluorescent color given a particular combination of beaming wavelengths from the three different types of quantum dots.

order to fabricate such cQD multiresonant antennas, we pattern in a first step, as discussed in Section 4.2.1, a Si template with the desired grating structures and after surface functionalization, we drop-cast a film of cQDs of mixed colors. In a first demonstration, we prepared a mixture of red and green cQDs with $\lambda_{em1}= 540$ nm and $\lambda_{em2}= 630$ nm and fabricated rectangular structures that present two axes around the centre with two distinct periodicities $\Lambda_1= 340$ nm and $\Lambda_2= 400$ nm. Such periodicities were optimized, taking into account the n_{eff} of Eq. (4.1) to provide beaming for the two colors, respectively. Such rectangular building blocks can, in turn, be employed to generate more complex functional images as in the case of the traffic light pattern in Figure 4.6. By introducing a linear polarization analyzer before the collection optics, we can control the color and therefore the image generated by the light emitted through

the fluorescent film. This multicolor concept can of course be further ex-

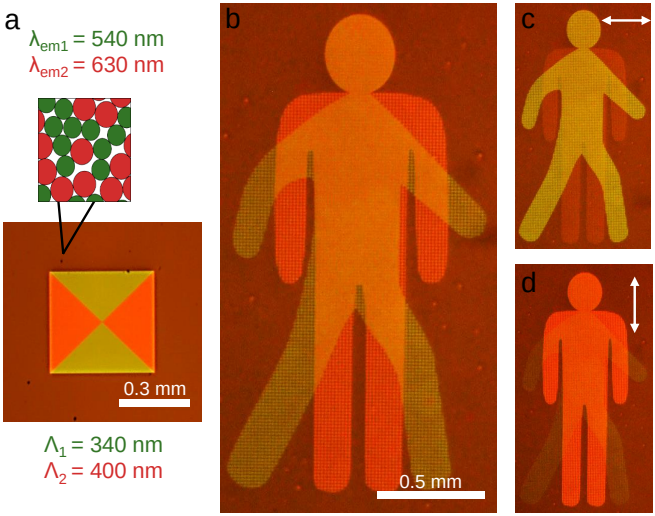

Figure 4.6 – (a) A dual-color film is created by depositing cQDs of two different emission colors $\lambda_{em1} = 540$ nm and $\lambda_{em1} = 630$ nm. Rectangular structures with $\Lambda_1 = 340$ nm and $\Lambda_2 = 400$ nm can provide emission for green and red wavelengths, respectively. (b) Fluorescence image of a traffic light pattern composed of numerous rectangular nanostructures. (c) and (d) By introducing a linear polarization analyzer it is possible to filter out one emission color.

tended by, for instance, generating hexagonal patterns that include three different periodicities (Figure 4.7a, $\Lambda_1 = 275$ nm, $\Lambda_2 = 340$ nm, and $\Lambda_3 = 400$ nm)and therefore allow for beaming of three different colors ($\lambda_{em1} = 460$ nm, $\lambda_{em2} = 540$ nm, and $\lambda_{em3} = 630$ nm respectively). Due to the vectorial nature of light polarization, it is not possible to independently control the emitted color using polarization. However, as in the case of the rectangular structure, it is possible to modify the ratios of the different RGB colors to obtain a tunable white-light source. In Figure 4.7b we report spectra of the emission outcoupled from the hexagonal structure

recorded as a function of analyzer angle to show that intensities of the different colors vary when the angle of the linear polarization analyzer is varied. This polarization dependence would basically allow us to generate a tunable white light source that could generate a warmer or cooler tone of white. In Figure 4.7c we map the spectral features of the emitted light on the CIE (Commission internationale de l'éclairage) color space for each linear polarization angle (in Appendix C.1 we clarify the procedure to define the coordinates on the CIE map starting from our spectral representation).

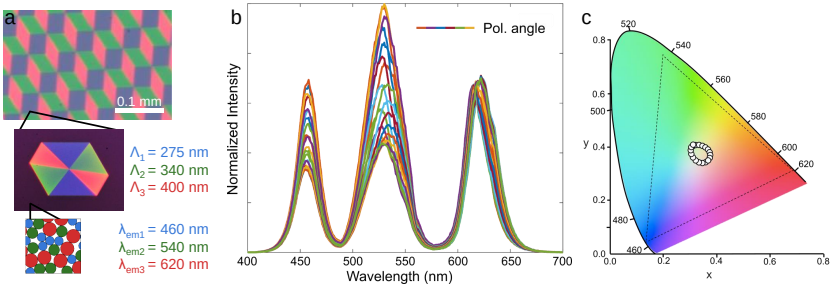

Figure 4.7 – (a) An RGB cQD film is fabricated by dropcasting a dispersion containing three different nanoparticle sizes with emission colors around $\lambda_{em1} = 460$ nm, $\lambda_{em2} = 540$ nm, and $\lambda_{em3} = 620$ nm. Hexagonal structures with $\Lambda_1 = 275$ nm, $\Lambda_2 = 340$ nm, and $\Lambda_3 = 400$ nm can provide directional emission for blue, green, and red wavelengths, respectively. (b) Spectra recorded from the hexagonal ensemble as a function of linear polarization analyzer. (c) Mapping the recorded spectra in (b) on a CIE map where tunable white light is achieved. The vertices of the black dotted triangle indicate the peak emission wavelengths of the three initial cQD colors.

4.5 High-order structuring of light beams

The generation of complex light patterns is possible using nanoscale devices. This process requires careful design of optical components at

the nanoscale with appropriate choice of materials to enable the desired interaction with the light mode of interest. Exploiting the multiresonant-antenna structure already described, we can provide higher-order structuring to the emitted light by directly patterning the cQD film. The linear gratings building blocks, with their properties, together with the possibility to combine different colors of colloidal quantum dots, can allow extensive versatility and ease of design in controlling the directionality, spectral definition, and polarization state of the generated beams of fluorescence. To investigate such functionality, we use k-space microscopy as introduced in Section 4.3.1. In Figure 4.8 we show k-space maps recorded for linear gratings with periodicity Λ ranging from 450 nm on the left to $\Lambda = 350$ nm on the right in steps of 25 nm. The arcs of high intensity that satisfy Eq. (4.1) follow the orientation of the corrugations and are therefore perpendicular to the grating vector as will be discussed later in more detail. As discussed in Section 2.3.1, by introducing a quarter-

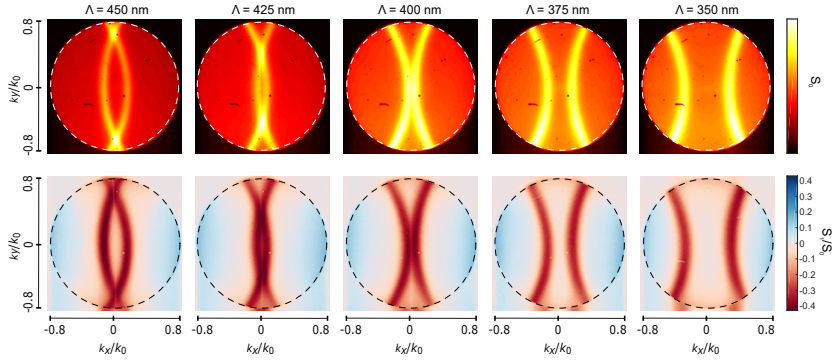

Figure 4.8 – Fluorescence k-space maps of S_0 (top) and S_1/S_0 (bottom) recorded from linear grating of different periodicities. From left to right Λ varies from 450 to 350 nm in steps of 25 nm. The wavelength of emission of the cQDs is $\lambda_{em} = 635$ nm. The strongest outcoupling in the normal direction is observed for $\lambda = 400$ nm, as shown in Figure 4.4 and as predicted by Eq. (4.1).

wave plate (QWP) and a linear polarization analyzer (LP) at the back focal plane of the objective, we can retrieve the four Stokes parameters

that allow the full description of the polarization state of the emitted beam of light. For example, the measured intensity distribution for the S_1 parameter, describing the amount of vertically polarized light with respect to the amount which is horizontally polarized, shows that such cQD linear gratings emit predominantly linear polarization (full polarimetric characterization of these linear gratings is found in Appendix C.2). By using linear gratings as building blocks, we can work towards the

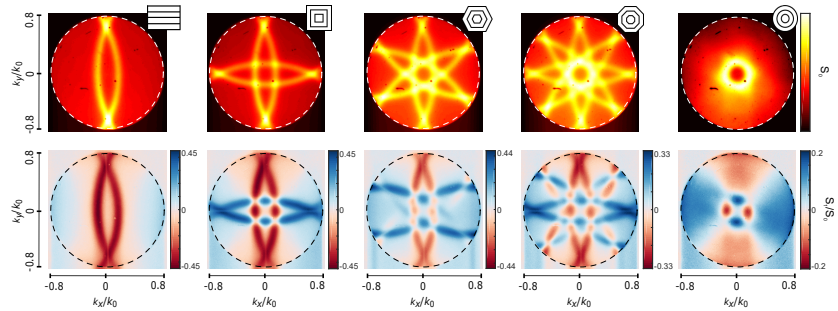

Figure 4.9 – Higher-order structuring of light beams using multiresonant nanopatterns. Angle-resolved S_0 and S_1/S_0 parameters are shown in the top and bottom row, respectively, for a grating with $\Lambda = 450$ nm. By using linear gratings and their polarized emission as building blocks, we can increase the number of axes of our antenna around the centre and progress from a simple linear-grating structure (left) to a hexagonal structure with three axis (centre) towards a bull's-eye antenna with an infinite number of axes around the centre (right). The S_1/S_0 patterns show that this design provides a route for polarization structuring of light beams.

realization of more complicated directional and polarization-dependent beams. We can increase the number of axes along which linear gratings are patterned (see top row of Figure 4.9 for gratings with $\Lambda = 450$ nm), until we have an infinite number around the centre in a configuration which corresponds to the so-called bull's-eye. Figure 4.9 reports also the normalized S_1 Stokes parameter for the different structure geometries. If we consider the case of the bull's-eye antenna, which due to its concentric geometry does not have a preferred polarization distribution,

and merge the measured k-space maps for S_1 and S_2, we obtain a final linear polarization distribution as shown in Figure 4.10. The resulting polarization distribution shows an azimuthal-type behaviour around the high-intensity directional resonance and a radial-type behaviour for the background emission. If we compare this measured distribution with the

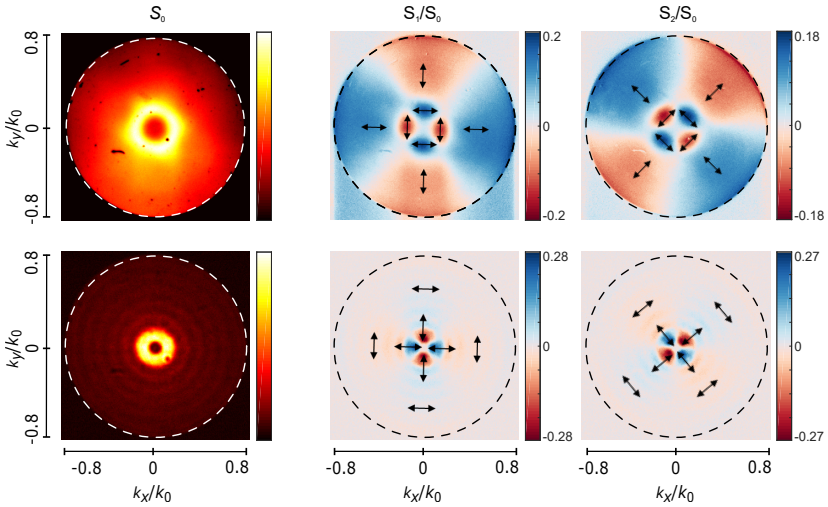

Figure 4.10 – Comparison between S_0, S_1/S_0 and S_2/S_0 k-space patterns generated by (top) a bull's-eye QD antenna working in fluorescence and (bottom) a bull's-eye plasmonic antenna working in transmission configuration. S_1/S_0 and S_2/S_0 parameters show azymuthal-like patterns in the resonant beaming directions for the QD case and a radial polarization distribution for the background emission. The inverted case is found for the plasmonic structures where the background emission is also significantly reduced.

one generated by quasi-monochromatic light transmitted through a silver plasmonic bull's-eye aperture fabricated with the procedure described in Section 2.2.2 of Chapter 2 for multiresonant antennas, we notice an inverted polarization pattern. As introduced in Chapter 2 and as different investigations in literature have demonstrated, surface-plasmon-mediated

scattering from linear gratings generates light which is p-polarized (TM) in the plane perpendicular to the lines of the grating. Therefore, the scattered waveguided modes in the thin quantum-dot film have instead the opposite polarization, with the electric field perpendicular to the grating vector (TE). This observation is also supported by fluorescent imaging measurements where a linear polarization analyzer can be introduced before the imaging camera.

4.6 Conclusions and outlook

Direct patterning of fluorescent materials allows for new types of on-chip nanoscale-controlled light sources. Using the template stripping method with appropriate functionalization of the silicon template, high-quality subwavelength patterns can be realized in a simple and reusable fashion. Moreover, the use of colloidal chemistry allows the combination of different types of fluorescent (and even non-fluorescent) materials in the same nanostructured film, increasing the versatility of this fabrication technique. By carefully engineering the nanopatterns that can be controlled with high-resolution with common lithographic techniques that also can be extended to large scale with other strategies to pattern the template, we can create structures that allow for the generation of polarized directional and tunable emission. The use of compact multiresonant geometries that combine the multicolor capability with the possibility to generate color-dependent directional beams addresses different functions and opens new routes for more complicated types of structured light. Polarization-structured beams like azimuthal or radial beams in particular have widely been used in optical applications like trapping or near-field-measurement techniques. By mapping the orientation of the polarization ellipse [63], as in Figure 4.11, it is also possible to generate beams with designed polarization singularities (i.e. where the orientation of the polarization ellipse is indefinite). Moreover, the investigation of the energy-dependent behaviour of these directional beams as a function of polarization can be achieved by the use of dispersed k-space maps as the results that we see in Figure 4.12a,b for linear gratings and Figure 4.12c,d for rectangular structures. This allows us to explore the modes generated in the high-

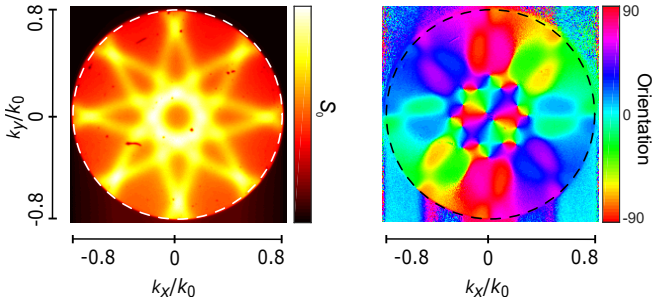

Figure 4.11 – k-space maps of an octagonal cQD antenna with $\Lambda = 400$ nm. (left) S_0 and (right) orientation of the polarization ellipse (°) where polarization singularities are present.

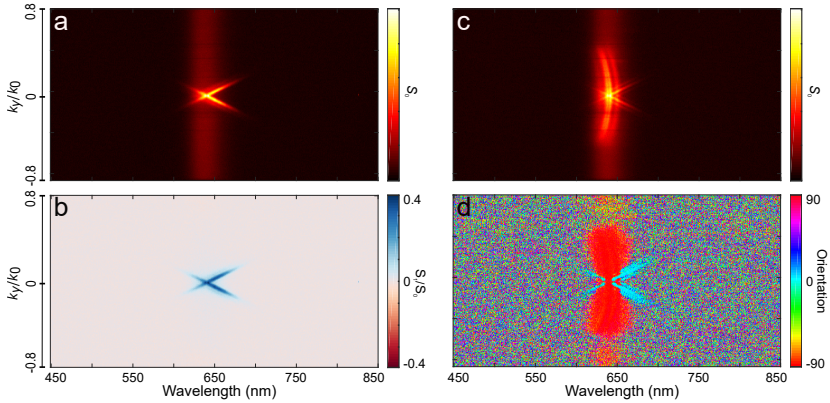

Figure 4.12 – k-space maps dispersed around $k_x = 0$ for linear gratings and for rectangular structures with $\Lambda = 400$ nm. (a) S_0 and (b) S_1/S_0 parameter for a linear grating. (c) S_0 and (d) orientation of the polarization ellipse (°) for a rectangular structure.

refractive-index film more in detail opening new routes for additional levels of light structuring.

Chapter 5

Photonic crystals to tailor thermal emission

In this chapter, we apply Fabry-Pérot 1D photonic-crystal cavities to tune the spectral response of thermal emitters and boost the efficiency of a thermophotovoltaic (TPV) device. Conventional photovoltaic cells convert in electricity only incident solar light that has an energy above their bandgap and are, therefore, unable to exploit the full solar spectrum. TPV devices, on the other hand, can overcome this limitation by first converting light into heat with the use of an absorber element and subsequently, using a radiator element, re-emit thermal radiation that is spectrally tailored to contain frequency components only above the bandgap energy of the photovoltaic cell. This two-step process potentially doubles the efficiency of conventional photovoltaic cells and also allows integration with other energy sources that generate heat (such as combustion or nuclear reactions). Here, we focus on the realization and measurement of the radiator element and show that 1D photonic-crystal cavities are powerful structures for efficient TPV applications. Through a combination of numerical simulations and high-temperature thermal-emission measurements, we will present the optimization of such a device for low-bandgap solar cells and integration on a SiC microcombustor.

5.1 Introduction

Conventional photovoltaic (PV) cells can only convert incident light with an energy above the bandgap into electricity and are, therefore, unable to exploit the full solar spectrum. Moreover, their power production often relies on the surrounding environment with "intermittencies" in the availability of the source (ex. depending on the time of the day or the season). On the other hand, termophotovoltaic (TPV) devices can overcome this limitation by first converting light into heat and subsequently re-radiating this heat above the bandgap energy of a photovoltaic cell. This two-step process can potentially double the efficiency of conventional photovoltaic devices and also allow integration with other energy sources including wasted heat (such as combustion or nuclear reactions) [126, 127].

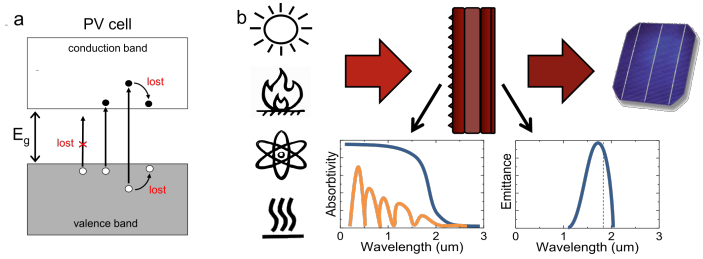

Figure 5.1 – (a) Schematic of energy conversion in a conventional photovoltaic (PV) cell. Energy of the incoming photons which is lower or higher compared to the cell bandgap will be lost and not efficiently converted into electricity. (b) Schematic of a thermophotovoltaic system. Different potential heat sources can be used to power the TPV device, including the use of solar energy efficiently captured by an absorber element. A hot thermal emitter then radiates for selected wavelengths close to the PV cell bandgap, ensuring high conversion efficiencies.

The emitter/radiator plays an essential role in a TPV device since it converts heat into radiation with frequecies that lie in a specific spectral window that can be efficiently converted into electricity by the PV cell. Apart from their spectrally selective response though, radiators need to

be able to operate under challenging conditions. Such structures and materials must sustain high temperatures of operation (usually $> 1000°C$), achieve high emissivities and long lifetimes, and also have good thermal conductivities that allow for uniform temperature distributions.

Concepts from photonics and plasmonics can be used to manipulate thermal emission in metallic structures. In particular, periodic nanostructures with designed spectral and angular response have been extensively proposed in the literature as wide-band thermal emitters since they are capable of exhibiting near-blackbody thermal emission within a defined wavelength range or angles and strongly attenuate emission elsewhere [127]. For their fabrication, usually refractory metals are combined with high-refractive-index dielectrics. Metals have in fact high emissivities at short wavelengths and reduced emissivities in the mid and far infrared portion of the spectrum which makes them good candidates for TPV. In particular, refractory metals present high melting points and thermal stability at elevated temperatures. At the same time, adding antireflective (AR) dielectric coatings to such metal films can enhance significantly their emissivity. Nanoscale corrugated surfaces of metals have been successfully demonstrated for TPV applications, being able to reach high emissivity values [23, 128–131]. Nevertheless, their durability is affected by surface diffusion and polarization- and angle-dependent emissivities for structures like gratings are not sufficiently high [23, 36]. For these reasons, a lot of the most efficient TPV nanostructured designs consist of photonic crystals with alternating materials of high and low dielectric constants [132–136]. In particular, metal–dielectric interference stacks can exploit the high reflectivity of metals and the low absorption and high permittivity of some dielectrics. In these structures, the periodicity of the lattice can be designed such that light in the undesired frequency range destructively interferes (see Section 1.3) giving rise to photonic bandgaps [2, 137]. Wavelengths outside of the bandgap can propagate through the structure with little attenuation. Moreover, the spectral response of such structures is polarization independent as well as only weakly dependent on the collection angle.

Here, we describe our efforts in realizing an optimal thermal emitter to be integrated on an existing silicon carbide microcombustor for continuous and flexible TPV power production. To tune the spectral response

of thermal emitters to match the spectrum of the photocell and boost the efficiency of a TPV device, we explored Fabry-Pérot 1D photonic crystals consisting of layers of materials with alternating refractive index. The fabrication and characterization experiments are supported by numerical simulations performed in our research group. The optical performance of 1D photonic-crystal cavities is extremely sensitive to fabrication-controlled properties such as surface roughness and thickness variation of our dielectric stack, but also dielectric constant and thermal stability. For this reason, we have performed extensive studies of the deposition parameters influencing for example the optical properties and high-temperature stability. Since our target operating temperature is between 1100 and 1300°C, we decided to use: silicon carbide (SiC), already employed for the combustor, tungsten (W, which has the highest melting point, of ∼3400°C, among all metals), and aluminum oxide (Al_2O_3) for the emitter. All fabrication processes were optimized to avoid any delamination at the required high temperatures. We also developed an experimental setup that allows to perform reflection and emission measurements at high temperatures. The optical setup includes the use of a thermal stage to heat the samples and collection optics to direct the infrared light into a Fourier-tranform infrared spectrometer (FTIR). As a consequence of these efforts almost unity emissivity along the normal direction of the sample in the desired spectral range was achieved. Moreover, at 1300°C around 30% overlap of the thermal emission from our structure with the spectrum of the photovoltaic cell was obtained, which would indeed allow a boost in the efficiency of the hybrid device.

5.2 Design and fabrication of the thermal emitter

5.2.1 Design concept

A TPV device usually consists of four main parts: a concentrator, an absorber, an emitter, and a photocell. The absorber and emitter can be structured at the nanoscale to optimize their performance. Ideally, the absorber should collect all incident radiation from the sun while, on the other side, the emitter should radiate the absorbed energy in a narrow

frequency range that matches the absorption edge of the photocell. To focus on the design of the emitter block, we assume the use of an InGaAs photocell with a bandgap of 750 meV and that, during solar operation, the temperature of the emitter can be maintained between 1100 and 1300°C using a solar concentrator.

For the design of our thermal emitter, the emissive power from a surface in the selected wavelength and angular ranges can be obtained as:

$$P = \int_{\lambda_1}^{\lambda_2} \int_{\varphi_1}^{\varphi_2} \int_{\theta_1}^{\theta_2} L_{e\lambda} \langle \varepsilon(\lambda, \varphi, \theta) \rangle \cos\theta \sin\theta d\theta d\varphi d\lambda, [\mathrm{W} \cdot \mathrm{m}^2] \tag{5.1}$$

where $[\lambda_1, \lambda_2]$ is the wavelength range, $[\phi_1, \phi_2]$ is the azimuthal angle range, $[\theta_1, \theta_2]$ is the polar angle range, $\langle \epsilon(\lambda, \phi, \theta) \rangle$ is the polarization-averaged emissivity of the surface which depends on material and structure of the emitter, and $L_{e\lambda}$ is the spectral radiance:

$$L_{e\lambda} = \frac{2hc^2}{\lambda^5} \frac{1}{\exp(hc/\lambda k_B T) + 1} [\mathrm{W m^{-2} \mu m^{-1} sr^{-1}}] \tag{5.2}$$

where c is the velocity of light in vacuum, h is the Planck's constant, k_B is Boltzmann's constant, and T is the temperature of the emitter. According to Kirchhoff's law, the emissivity of a body equals its absorptivity [138], thus:

$$\langle A(\lambda, \phi, \theta) \rangle = \langle \epsilon(\lambda, \phi, \theta) \rangle \tag{5.3}$$

Using an electromagnetic numerical solver, the absorption of the structure, $A(\lambda, \phi, \theta)$, can be derived from an electromagnetic solver via the calculated reflection, transmission, and diffraction efficiencies:

$$A(\lambda, \varphi, \theta, \tau) = 1 - R(\lambda, \varphi, \theta, \tau) - T(\lambda, \varphi, \theta, \tau) - \sum D(\lambda, \varphi, \theta, \tau) \tag{5.4}$$

where τ denotes the polarization state.

To optimize the emission, we utilized a fitness function, Fit, which is a parameter that quantifies the quality of the emitter. It can be introduced in a variety of ways. One possibility is to calculate the fitness as:

$$Fit = \widetilde{P}_{used} - \widetilde{P}_{unused} \leq 1 \tag{5.5}$$

where:

$$P_{used} \equiv P_{0\to\lambda_g} = \int_0^{\lambda_g}\int_0^{2\pi}\int_0^{\pi} L_{e\lambda}\langle\varepsilon(\lambda,\varphi,\theta)\rangle \cos\theta \sin\theta d\theta d\varphi d\lambda \tag{5.6}$$

$$\widetilde{P}_{used} \equiv P_{0\to\lambda_g}/P^{BB}_{0\to\lambda_g} \tag{5.7}$$

$$P_{unused} \equiv P_{\lambda_g\to\infty} = \int_{\lambda_g}^{\infty}\int_0^{2\pi}\int_0^{\pi} L_{e\lambda}\langle\varepsilon(\lambda,\varphi,\theta)\rangle \cos\theta \sin\theta d\theta d\varphi d\lambda \tag{5.8}$$

$$\widetilde{P}_{unused} \equiv P_{\lambda_g\to\infty}/P^{BB}_{\lambda_g\to\infty} \tag{5.9}$$

where P_{used} and P_{unused} represent the emitted power that can and cannot be used (and therefore converted) by the InGaAs photocell respectively and $P^{BB} = \sigma T^4$ is Boltzmann's law for a black body.

From the numerical calculations performed with the code described in [139], and by using experimental optical contants measured using spectroscopic ellipsometry (see Section 5.2.2.1), we obtain an optimized Al_2O_3/W 1D photonic crystal structure as showed in the inset of Figure 5.2 with thicknesses of the layers from top measuring 155, 18, 160, and 85 (or optically thick) nm to achieve maximum absorptivity (emissivity) close to the PV cell bandgap (750 meV).

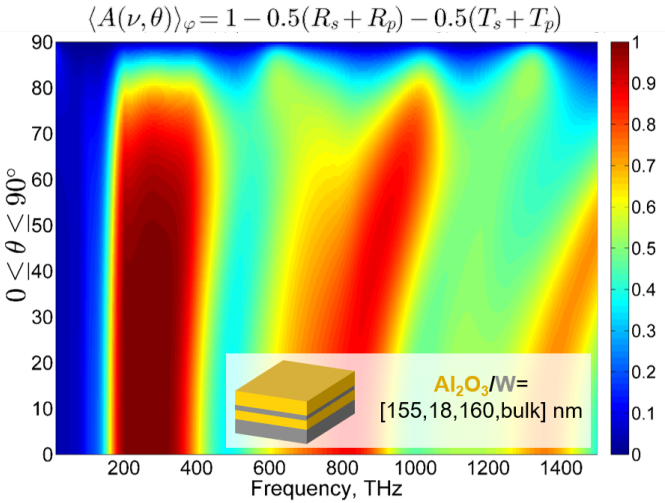

Figure 5.2 – Absorption (ϕ- and polarization-averaged) of the optimized Al_2O_3/W multilayer as a function of frequency and polar angle θ (see inset for details on the calculated optimal materials thicknesses).

5.2.2 Materials

5.2.2.1 Deposition and characterization

The quality of a deposited thin film depends on the deposition method but it is also heavily dependent on deposition rates, pressures, and substrate temperature.

The thermal emitter employed in our work was fabricated using magnetron sputtering (Kurt J. Lesker PVD 75). In a first step, W layers were deposited on a Si or SiC substrate with a DC sputtering power of 250 W. The argon pressure was varied from 0.5 to 25 mTorr to achieve optimal thermal stability. A few attempts with heated substrate during deposition were also performed but gave rise to rougher surfaces. In Figure 5.3 we report the scanning electron micrographs of W films

deposited with different argon pressures along with the optical constants measured (using the spectroscopic ellipsometer V-VASE or VUV-VASE, J. A. Woollam Co.) and those reported from literature (Palik [140]). As

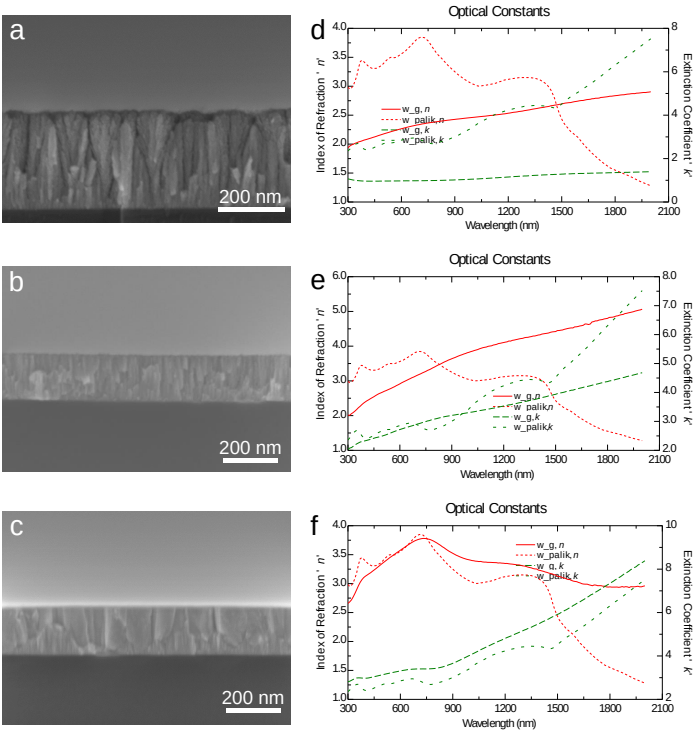

Figure 5.3 – Cross-sectional scanning electron micrographs and refractive indices of tungsten layers deposited with an argon pressure of: (a) and (b) 25 mTorr; (c) and (d) 6 mTorr; (e) and (f) 0.5 mTorr. All the films were deposited with a DC sputtering power of 250 W.

can be seen in Figure 5.3a-c, the W structure varies significantly with argon pressure. At high deposition pressures, the sputtered atoms undergo collisional scattering by the inert gas atoms in the sputtering chamber

and the oblique component of the deposition flux is increased. This enhances atomic shadowing where high points on the growing surface can receive more coating flux during the deposition than the valleys leading to columnar grains separated by voids and increased surface roughness (see atomic force micrographs of Figure 5.4). On the other hand, lower pressures allow the sputtered atoms to retain most of their kinetic energy since fewer thermalizing collisions and scattering occur. Therefore, less shadowing and higher surface diffusion favor an increase in the density of the deposited film which then translates in optical constants closer to literature values. In the same way, increasing the substrate temperature can enhance adatom surface mobility favoring local crystal growth [141, 142].

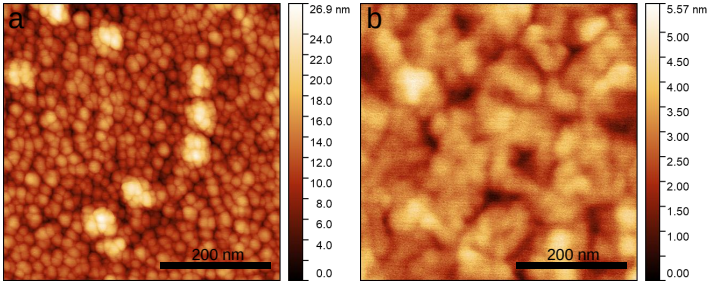

Figure 5.4 – Atomic force micrographs of the surface of tungsten layers deposited at (a) 25 mTorr and (b) 0.5 mTorr argon pressure where bigger grains are formed.

5.2.2.2 Thermal stability

The high-temperature stability of such W films fabricated under different deposition conditions was tested. For this purpose, a heating stage (Linkam TS1500) was used. After evacuation of the heating chamber to 10^{-5} mbar, the temperature was raised to 900°C at a rate of 20°C/min and then cooled to room temperature with the same rate. Scanning electron micrographs in Figure 5.5 show delamination of films deposited with

low deposition pressures. On the other hand, no significant structural modification or significant change in the surface roughness was observed for the other films. Therefore while lower deposition pressures led to high

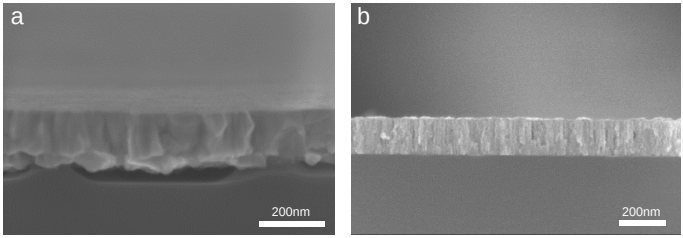

Figure 5.5 – Scanning electron micrographs of tungsten films deposited at (a) 0.5 mTorr and (b) 6 mTorr argon pressure after heating at 900°C. Stress in films deposited at low argon pressures can cause significant delamination from the substrate upon heating.

densities, they can also increase the stress incorporated in the films. This stress is usually of compressive nature caused by tightly packed columnar grains [143]. At high temperatures, the thermal expansion of the material can therefore cause delamination from the substrate. X-ray diffraction (XRD) measurements are shown in Figure 5.6 and summarize some of the discussed characteristics of films deposited at high or low argon pressures. In general, a stronger signal of the XRD peaks is collected from films deposited at lower pressures. This is probably an indication of grains with larger size due to the reduced influence of deposition shadowing. Similarly, a broadening in the peaks associated with higher deposition pressure suggests smaller crystallite size. The broadening at very low deposition pressures (i.e. 0.5 mTorr) can probably be associated with non-uniform strain. A uniform stress distribution also deviates the XRD peaks from the diffraction lines for the low pressure films [144]. A good compromise in terms of film density, incorporated stress, optical properties, and surface roughness appears to be achieved with the use of 6 mTorr argon pressure during the deposition of the W films. The 1D photonic crystal cavities used for thermal emission measurements were fabricated with this deposition parameter. Aluminum oxide layers were deposited

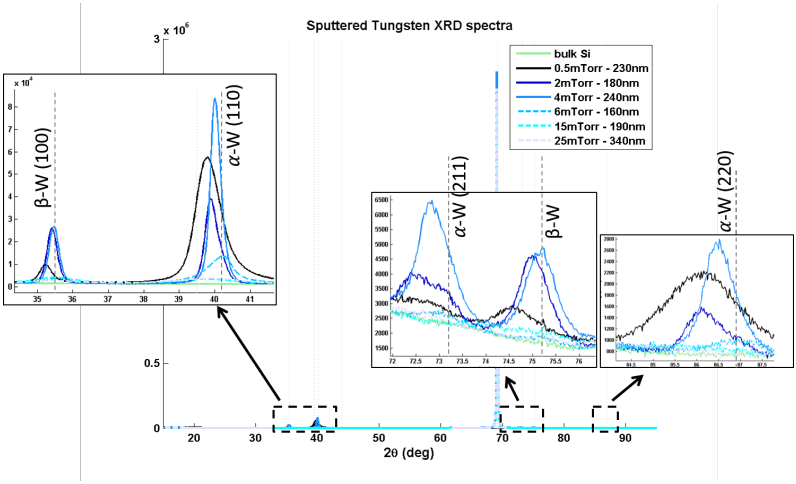

Figure 5.6 – X-ray diffraction measurements of tungsten films fabricated with different deposition pressures. Dotted gray lines indicate the diffraction lines corresponding to expected W phases and crystal orientations.

with a reactive RF sputtering process at 200 W and a pressure of 1 mTorr. Since roughness and grain size can influence the desired optical response, atomic force microscopy was used to characterize the surface of the different sputtered materials, as shown in Figure 5.7a,b. An average surface roughness lower than 3 nm was measured for the multilayer top surface (Figure 5.7d). The material optical constants were determined using spectroscopic ellipsometry (as shown in Figure 5.3 for W films). The refractive index for Al_2O_3 films was measured to be around 1.64 in most of the NIR range. These parameters are important for checking the quality of the deposited layers in comparison with theoretical simulations.

The thermal stability of the 1D photonic crystals was again tested under vacuum (10^{-5} mbar) maintaining the temprature at 900°C for 6 hours. After this heating period, when the samples were examined using scanning electron microscopy, no delamination or defect formation was observed in

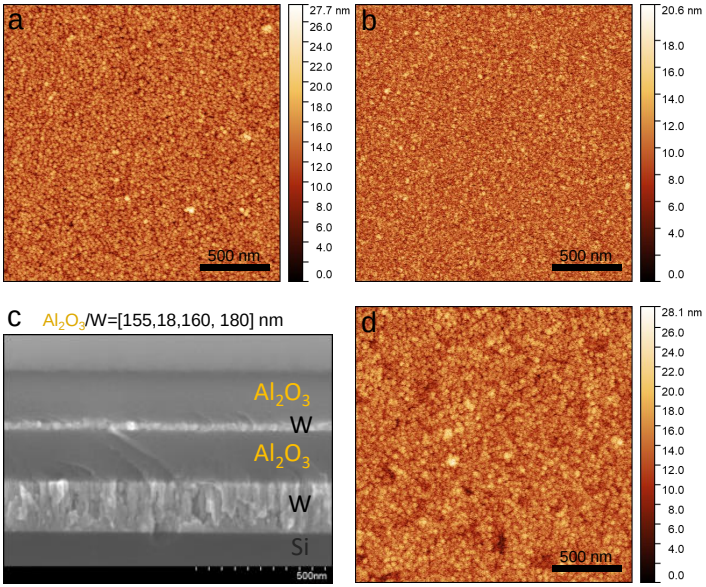

Figure 5.7 – Atomic force micrographs of the (a) tungsten layer, (b) aluminum oxide layer, and (c) multilayer top surface deposited on a Si wafer. A final average surface roughness < 3 nm is measured for the single films as well as for the photonic crystal stack.

scanning electron micrographs (Figure 5.8a). Moreover, surface investigations revealed a surface roughness similar to the values determined prior to the heating process. With the same purpose, structures fabricated on purchased polished SiC (MTI-XTL) were brought to 1300°C. No substantial deteriorating effect, such as delamination, can be noticed when the structures are imaged after heating (Figure 5.8b, the crossection was realized using focused ion beam milling).

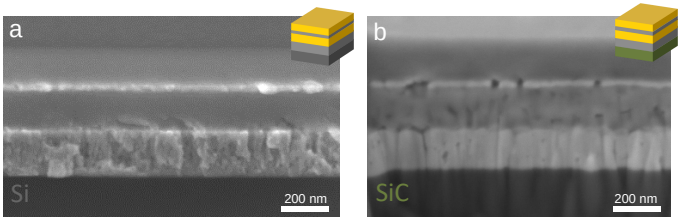

Figure 5.8 – Cross-sectional scanning electron micrograph of the refractory materials stack on (a) silicon after heating up to 900 °C and (b) silicon carbide after heating up to 1300 °C. The structure deposited on silicon carbide has been patterned using a focused ion beam to access its crossection.

5.3 Thermal emission measurements and integration on a SiC microcombustor

An optical system that allows the testing of the nanostructures spectral response in the IR range is shown in Figure 5.9. The thermal emitter was placed on a heating element inside a water-cooled chamber (Linkam TS1500 heating stage). The chamber can be evacuated or filled with inert gases. In our main tests, we evacuate the chamber to 10^{-5} mbar using a turbo pump. After evacuation, the sample reached high temperatures at a rate of 20°C/min or of 100°C/min. The emitted radiation is collected, using a KBr beam splitter and a liquid-nitrogen-cooled InSb detector, in a Fourier-transform infrared spectrometer (FT-IR, Bruker Vertex 80) for spectral analysis. Absorptivity/reflectivity measurements were carried out with the use of a broadband light source (ORIEL, Newport) and a beam splitter in the optical path (see setup in Figure 5.9). According to Kirchhoff's law, where absorptivity equals emissivity at thermal equilibrium, the emissivity spectra are extracted from the reflectivity measurements (Abs = 1 - Refl). The absorptivity (and calculated derived emissivity) of the optimized structures measured at room temperature approaches unity and is significantly higher if compared to the one of a bare W film (Figure 5.10, measurements in the visible were performed

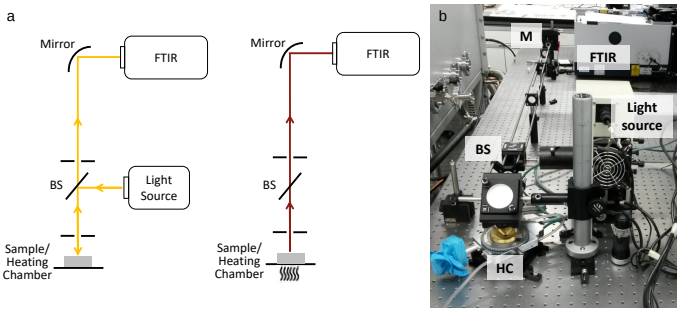

Figure 5.9 – (a) Schematics of the thermal-emission measurement setup. For reflectivity/absorptivity measurements a broadband light source is introduced in the setup. (b) Photograph of the actual experimental setup. HC = heating chamber, BS = beam splitter, and M = mirror.

using the inverted Ti-U microscope and spectrometer setup of Chapter 2 and Chapter 3). Good agreement is found between the measured and the calculated absorptivity values. To proceed with absorptivity measurements at high temperature, the nanostructures were deposited both on polished purchased SiC (MTI-XTL) and on the SiC combustor chambers for integration. The stack was integrated on both polished and unpolished combustor chambers fabricated by Microcertec SAS. The mirror-like surface of Figure 5.12b is an indication of conformal deposition of the layers. Better results were obtained on polished surfaces where the thickness of each deposited layer could be controlled with higher accuracy.

The structures were then tested and characterized at high temperatures. Due to the sensitivity of W to oxidation when exposed to air, preferred conditions for high temperature stability of metal structures are vacuum or inert gas conditions. Therefore, main efforts were devoted to the investigation and optimization of absorptivity results and thermal stability over short and long time scales under vacuum conditions (pressures of 10^{-5} mbar). In Figure 5.12a,c we report the emissivity spectra of our thermal emitter for increasing temperatures. The structure maintains very good performances up to 1300°C. Under these conditions, extrapolation of the

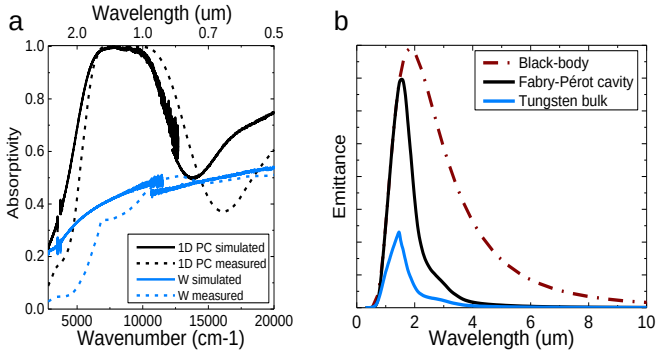

Figure 5.10 – (a) Numerical calculations (dotted lines) and measurements (continuous lines) of the absorptivity of the Al_2O_3/W Fabry-Pérot 1D photonic-crystal emitter compared to a bare W film. (b) Calculated emissivities for the two structures at 1300°C compared with a black-body spectrum. 1D PC= 1D photonic crystal.

cavity emittance demonstrated more than 30% of emission below 1.7μm (bandgap of InGaAs PV cell) for an emitter temperature of 1300°C, as shown in Figure 5.11b,d. Long-term stability measurements show negligible modification of the emissivity spectrum both at 1100 and 1300°C. A temperature of 1100°C (expected temperature at the surface of the combustor) was maintained for 8 hours and, once returned to room temperature, the sample inspected using a scanning electron microscope in cross-section configuration showed only small signs of degradation (Figure 5.12a).

5.4 Conclusions and outlook

We have shown the design, fabrication, and optical characterization of a 1D photonic-crystal cavity for thermophotovoltaic applications. The chosen structure consists of alternating layers of W and Al_2O_3 whose thickness and number of layers has been optimized numerically. The

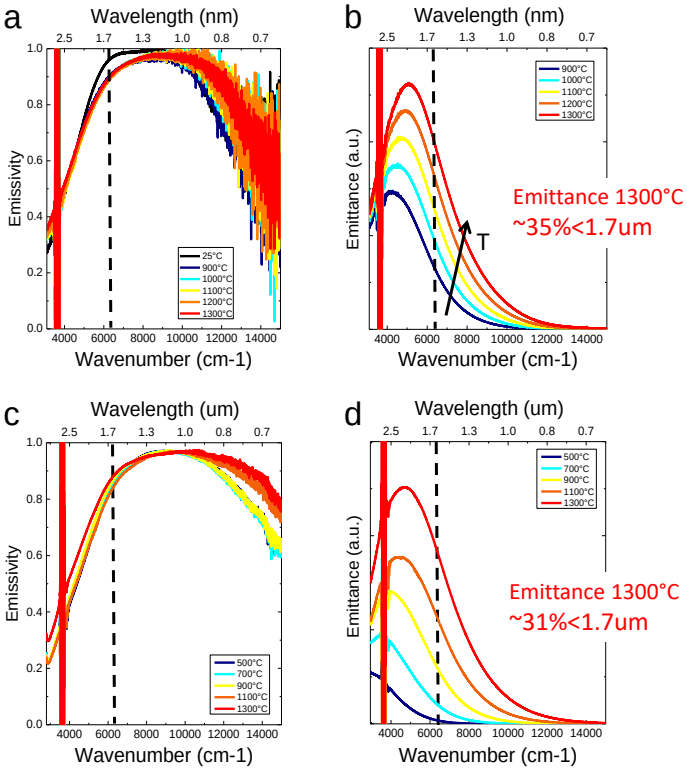

Figure 5.11 – (a) Measured emissivity spectra for the 1D photonic crystal cavity deposited on single-crystalline purchased polished SiC up to 1300°C and (b) extrapolated emittance. (c) and (d) For a cavity deposited on the combustor SiC fabricated and polished by Microcertec SAS. Dotted lines indicate the PV cell bandgap.

parameters of fabrication of the emitter are studied to achieve very small surface roughness and therefore more reproducible optical results, reduced stress in the films upon deposition, and optimized thermal stability

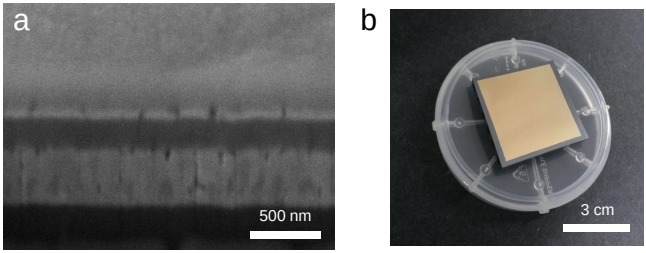

Figure 5.12 – (a) Cross-sectional SEM images of the 1D photonic crystal cavity, deposited on Microcertec SAS SiC, after annealing at 1100°C for 8 hours. (b) Optimized stack deposited on a combustor chamber and ready for full integration.

and optical properties. Significant enhancement in emissivity (almost reaching unity close to the bandgap) is observed when the nanostructure is compared to bulk W films. The thermal stability is also investigated, mainly under vacuum conditions where more than 30% of the emission is obtained for frequencies above the bandgap, but also under air and controlled atmosphere.

Further investigations of the behaviour under controlled atmosphere and air need to be performed. Preliminary results were obtained by connecting argon gas inlet and outlet tubes to the heating chamber. After stabilizing the argon flow, the photonic-crystal structure was annealed up to 1100°C. The spectra and SEM images of the structure reported in Figure 5.13 show that the structures can reach high temperatures even though they indicate a higher oxidation probability for the W films compared to the vacuum case. For this reason, argon parameters should be controlled more accurately and a pre-evacuation of the chamber could be necessary. When the emitter is heated in air, the W films are stable up to 700°C. After this temperature, a combination of focused ion beam and scanning electron micrographs revealed an increase in porosity in the W film and a significant thermal expansion. A thermogravimetric analysis was carried out in both air and inert atmosphere and demonstrated an increase in the structure's weight around 700°C when heated in air, probable indication

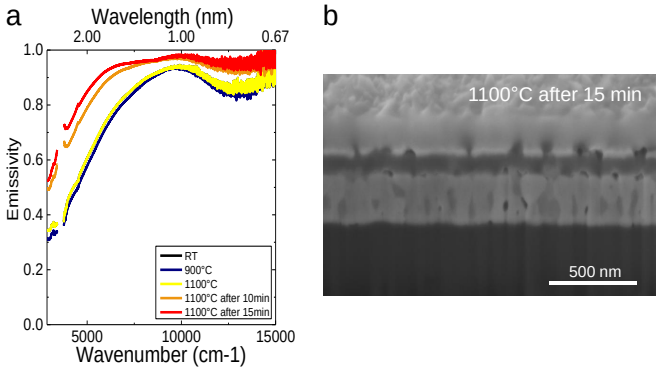

Figure 5.13 – (a) Emissivity spectra for a photonic crystal cavity up to 1100°C and (b) Scanning electron micrograph of the sample after heating for 15 minutes at 1100°C.

of W oxidation. To prevent degradation of the structure above this critical temperature, a protective layer of HfO_2 of thicknesses varying from 5 to 50 nm was deposited on the W films using atomic layer deposition (ALD) [57, 133]. To improve the structure's adhesion to the substrate and try to reduce the effect of oxidation processes, a 15 nm thin Ti adhesion layer was deposited on the combustor surface before proceeding with the fabrication of the 1D photonic crystal cavity. This precaution slightly improved the high temperature stability of the structure but increased the chance to observe delamination wherever substrate defects were present. For future studies, by depositing the dielectric layers using ALD instead of sputtering higher protection to oxidation in both vacuum and non-vacuum conditions could be obtained. Alternatively, more inert materials (like platinum) could also be considered. Moreover, by introducing dielectric properties of the materials at high temperatures, further efforts can be oriented to numerically optimize the 1D photonic crystal cavity design to achieve higher efficiencies. In fact, such design structure allows flexibility also in the chosen bandgap value since by changing the thicknesses of the cavity stack, different spectral behaviours can be obtained.

Chapter 6

Conclusions and outlook

Multiresonant nanoantenna designs based on periodic corrugations with directional and polarization dependence have been introduced in this thesis. While a detailed outlook of the work presented is provided at the end of each chapter, we conclude the thesis by discussing the main findings and implications of our research. Furthermore, we describe possible future work that would enrich the functionalities of plasmonic and photonics nanoantennas for use in sensing, spectroscopy, integrated photonics, and thermal-emission applications.

The rapid development of nanofabrication techniques has driven the realization of a wide range of nanostructured thin films to manipulate light beams. In particular, plasmonic nanoantennas can strongly interact with light, confine electromagnetic fields at the nanoscale, and shape the far-field pattern of coupled emitters. Most nanoantenna designs are engineered to address one specific frequency, direction, or polarization. However, in many applications it is desirable to control many resonant wavelengths simultaneously while providing high directionality. In this thesis we have shown that the ability to predict and control both the polarization-dependent response of the plasmonic antenna and the polarization state of the outgoing light, offers a powerful perspective in manipulating the structure of electromagnetic fields. Inspired by the plasmonic bull's-eye apertures [13] that can demonstrate efficient light manipulation in sensing and photodetection [20] as well as thermal emission applications [23], in Chapter 2, we have introduced a new family of multiresonant bull's-eye nanoantennas. The concentric circular gratings of the bull's eye, which provided its polarization independence, were substituted with concentric polygonal corrugations that can provide a strong polarized response. By varying the periodicity of these corrugations along the different axes of the polygon, we showed polarization-dependent multicolor beaming. The central nanoaperture of such structures allows us to isolate very small sampling volumes and can be used as a nanocuvette for sensing applications. In fact, by coupling fluorescent emitters to the nanoaperture, we demonstrate polarization-based sorting of fluorescent colors.

In many photoluminescence applications that involve spectral sorting of fluorescence, such as surface enhanced spectroscopy, the detection efficiency can be greatly improved by enhancing the absorption/scattering and/or emission optical transitions [145]. In single resonance structures, the density of optical states is enhanced around one unique central frequency. However, if more than one resonant wavelength is present, higher enhancements can be achieved opening up possibilities for new interesting research fields [48, 49]. Our multiresonant bull's-eye antennas could be used for sequencing applications as suggested by our preliminary experiments of Section 2.4.3 and different single-molecule fluorescence measurements with nanoaperture antennas [65]. Wider interest could be enabled by extending these measurements to label-free detection.

Metasurfaces where multi-analyte identification in real time is possible are of great interest especially in the infrared range [96].

These considerations extend to the multiresonant hole-array structures presented in Chapter 3 where, by introducing differences in the periodicity of the different axes, we can achieve multicolor polarization-dependent extraordinary optical transmission. Aside from exploiting strong localized plasmonic near fields to enhance and tailor the emission from nanoscale light sources, we exploit the high transmittance attainable with these systems to use them as color filters. To extend this concept, in preliminary measurements, we show that it is possible to use these antennas to perform spectral reconstruction of quasi-monochromatic signals. Improving the spectral- and polarization-dependent response of these structures could open new routes for miniaturized polarization-controlled spectrographs.

Tailoring fluorescent emission can also be of great interest to realize on-chip light sources. For this purpose, the development of reproducible and versatile fabrication methods to structure fluorescent materials is of essential importance. In particular, direct patterning of colloidal quantum-dot (cQD) films can be used to realize extremely directional light sources for lasing applications [98]. In Chapter 4 we have demonstrated the fabrication and characterization of grating nanostructures to achieve directional and polarized emission. Such gratings building blocks offer plentiful opportunities to generate structured light beams. For example, in Section 4.4 we use the multiresonant bull's-eye design in combination with different types of cQDs to realize multicolor tunable light sources. In Section 4.5 we extend the use of linear grating building blocks to generate complex beams with structured intensity and polarization patterns as revealed from angle-resolved polarimetry measurements. It is also possible to combine such high-order structuring of light beams with a multicolor response to design a wavelength dependent far-field response. Our k-space polarimetry analysis reveals also the presence of polarization singularities whose properties and position could be carefully engineered.

In Chapter 5 we employed 1D photonic crystals as thermal emitters for thermophotovoltaic (TPV) applications. By introducing an additional step in the energy conversion process, which consists in the conversion of energy into heat before it reaches a PV cell in the form of electromagnetic

radiation, thermophotovoltaics allows the increase of power generation efficiencies [127]. A heated body can be in fact nanostructured such that the spectral properties of its thermal radiation are modified to match the bandgap energies of the PV cell. In particular, 1D photonic crystals have proved to be very promising structures for solar thermophotovoltaic applications [132]. Since high operating temperatures (above 1000°C) are required, it is important to establish the right typology and quality of the materials used. To achieve the best compromise between thermal stability and optical properties, we optimized the deposition process for the refractory materials that compose our 1D photonic structure (tungsten and aluminum oxide). A high-temperature absorptivity/emissivity measurement setup was then used to characterize the optical performance of the structures under vacuum conditions and also for long operating times, once integration on a microcombustor was performed. While most thermal emitters demonstrated for TPV applications operate under vacuum conditions, the performance of our stack was preliminarly tested also under inert atmosphere. Under these conditions a substantially reduced structural stability was observed, but the introduction of oxide capping layers and a more precise control of the atmosphere pressures inside the heating chamber could improve non-vacuum performance in future measurements.

Since studies on nanostructured thermal emitters exploiting surface phonon polaritons in materials like SiC were pioneering in the generation of directional and polarization-sensitive nanoantennas [128], we can envision interesting properties of these systems being translated to our plasmonic and quantum-dot antenna concepts. In particular, nanostructured thermal emitters that present a spin-split energy dispersion diagram have been developed [146, 147]. According to Greffet *et al.* [148], Kirchoff's law for thermal emission, i.e. that the absorptivity of a body in thermal equilibrium equals its emissivity, can be extended to model light emission by systems in local thermodynamic equilibrium which would allow, for example, to study spontaneous emission processes in semiconductors. For this reason, an interesting engineering problem would be to realize such spin-dependent nanostructures in our cQD films. Such designs could open new interesting directions in realizing on-chip sources with on-demand polarization properties or that could exhibit very par-

ticular spatial field distribution (e.g. carrying spin or orbital angular momentum).

Bibliography

[1] Hecht, E. *Optics*; Pearson education; Addison-Wesley, 2002.

[2] Saleh, B. E.; Teich, M. C.; Saleh, B. E. *Fundamentals of photonics*; Wiley New York, 1991; Vol. 22.

[3] Novotny, L.; Hecht, B. *Principles of nano-optics*; Cambridge university press, 2012.

[4] Norris, D. J. *Lecture notes – Introduction to plasmonics*; ETH Zürich, Optical Materials Engineering Laboratory, 2014.

[5] Grimaldi, F. M. *Physico-mathesis de lumine, coloribus et iride*; Victorii Benatii, 1963.

[6] Young, T. I. The Bakerian Lecture. Experiments and calculations relative to physical optics. *Philosophical Transactions of the Royal Society of London* **1804**, *94*, 1.

[7] Bethe, H. A. Theory of diffraction by small holes. *Physical Review* **1944**, *66*, 163.

[8] Genet, C.; Ebbesen, T. W. Light in tiny holes. *Nature* **2007**, *445*, 39.

[9] Cohn, S. B. Microwave coupling by large apertures. *Proceedings of the IRE* **1952**, *40*, 696.

[10] Ebbesen, T. W.; Lezec, H. J.; Ghaemi, H.; Thio, T.; Wolff, P. Extraordinary optical transmission through sub-wavelength hole arrays. *Nature* **1998**, *391*, 667.

[11] Ghaemi, H.; Thio, T.; Grupp, D. e. a.; Ebbesen, T. W.; Lezec, H. Surface plasmons enhance optical transmission through subwavelength holes. *Physical Review B* **1998**, *58*, 6779.

[12] Garcia-Vidal, F. J.; Martin-Moreno, L.; Ebbesen, T. W.; Kuipers, L. Light passing through subwavelength apertures. *Reviews of Modern Physics* **2010**, *82*, 729.

[13] Lezec, H. J.; Degiron, A.; Devaux, E.; Linke, R. A.; Martin-Moreno, L.; Garcia-Vidal, F. J.; Ebbesen, T. W. Beaming light from a subwavelength aperture. *Science* **2002**, *297*, 820.

[14] Ishi, T.; Fujikata, J.; Makita, K.; Baba, T.; Ohashi, K. Si Nano-Photodiode with a Surface Plasmon Antenna. *Japanese Journal of Applied Physics* **2005**, *44*, L364.

[15] Stanley, R. Plasmonics in the mid-infrared. *Nature Photonics* **2012**, *6*, 409.

[16] Laux, E.; Genet, C.; Skauli, T.; Ebbesen, T. W. Plasmonic photon sorters for spectral and polarimetric imaging. *Nature Photonics* **2008**, *2*, 161.

[17] Mahboub, O.; Palacios, S. C.; Genet, C.; Garcia-Vidal, F. J.; Rodrigo, S. G.; Martin-Moreno, L.; Ebbesen, T. W. Optimization of bull's eye structures for transmission enhancement. *Optics Express* **2010**, *18*, 11292.

[18] Aouani, H.; Mahboub, O.; Devaux, E.; Rigneault, H.; Ebbesen, T. W.; Wenger, J. Plasmonic antennas for directional sorting of fluorescence emission. *Nano Letters* **2011**, *11*, 2400.

[19] Novotny, L.; van Hulst, N. Antennas for light. *Nature Photonics* **2011**, *5*, 83–90.

[20] Schuller, J. A.; Barnard, E. S.; Cai, W.; Jun, Y. C.; White, J. S.; Brongersma, M. L. Plasmonics for extreme light concentration and manipulation. *Nature Materials* **2010**, *9*, 193.

[21] Koenderink, A. F.; Alù, A.; Polman, A. Nanophotonics: Shrinking light-based technology. *Science* **2015**, *348*, 516.

[22] Atwater, H. A.; Polman, A. Plasmonics for improved photovoltaic devices. *Nature Materials* **2010**, *9*, 205.

[23] Park, J. H.; Han, S. E.; Nagpal, P.; Norris, D. J. Observation of thermal beaming from tungsten and molybdenum bull's eyes. *ACS Photonics* **2016**, *3*, 494.

[24] Lozano, G.; Rodriguez, S. R.; Verschuuren, M. A.; Rivas, J. G. Metallic nanostructures for efficient LED lighting. *Light: Science and Applications* **2016**, *5*, 1.

[25] Brolo, A. G. Plasmonics for future biosensors. *Nature Photonics* **2012**, *6*, 709.

[26] Zijlstra, P.; Paulo, P. M. R.; Orrit, M. Optical detection of single non-absorbing molecules using the surface plasmon resonance of a gold nanorod. *Nature Nanotechnology* **2012**, *7*, 379.

[27] Arroyo, J. O.; Kukura, P. Non-fluorescent schemes for single-molecule detection, imaging and spectroscopy. *Nature Photonics* **2015**, *10*, 11.

[28] Punj, D.; Mivelle, M.; Moparthi, S. B.; van Zanten, T. S.; Rigneault, H.; van Hulst, N. F.; García-Parajó, M. F.; Wenger, J. A plasmonic 'antenna-in-box' platform for enhanced single-molecule analysis at micromolar concentrations. *Nature Nanotechnology* **2013**, *8*, 512.

[29] Kinkhabwala, A.; Yu, Z.; Fan, S.; Avlasevich, Y.; Müllen, K.; Moerner, W. E. Large single-molecule fluorescence enhancements produced by a bowtie nanoantenna. *Nature Photonics* **2009**, *3*, 654.

[30] Curto, A. G.; Volpe, G.; Taminiau, T. H.; Kreuzer, M. P.; Quidant, R.; van Hulst, N. F. Unidirectional Emission of a Quantum Dot Coupled to a Nanoantenna. *Science* **2010**, *329*, 930.

[31] Li, Z.; Shegai, T.; Haran, G.; Xu, H. Multiple-particle nanoantennas for enormous enhancement and polarization control of light emission. *ACS Nano* **2009**, *3*, 637.

[32] Shegai, T.; Li, Z.; Dadosh, T.; Zhang, Z.; Xu, H.; Haran, G. Managing light polarization via plasmon–molecule interactions within an asymmetric metal nanoparticle trimer. *Proceedings of the National Academy of Sciences* **2008**, *105*, 16448.

[33] Shegai, T.; Brian, B.; Miljkovic, V. D.; Kall, M. Angular distribution of surface-enhanced Raman scattering from individual Au nanoparticle aggregates. *ACS Nano* **2011**, *5*, 2036.

[34] Garcia-Vidal, F. J.; Martin-Moreno, L.; Lezec, H. J.; Ebbesen, T. W. Focusing light with a single subwavelength aperture flanked by surface corrugations. *Applied Physics Letters* **2003**, *83*, 4500.

[35] Martin-Moreno, L.; Garcia-Vidal, F.; Lezec, H.; Degiron, A.; Ebbesen, T. Theory of highly directional emission from a single subwavelength aperture surrounded by surface corrugations. *Physical Review Letters* **2003**, *90*, 167401.

[36] Han, S.; Norris, D. J. Beaming thermal emission from hot metallic bull's eyes. *Optics Express* **2010**, *18*, 4829.

[37] Jun, Y. C.; Huang, K. C.; Brongersma, M. L. Plasmonic beaming and active control over fluorescent emission. *Nature Communications* **2011**, *2*, 283.

[38] Harats, M. G.; Livneh, N.; Zaiats, G.; Yochelis, S.; Paltiel, Y.; Lifshitz, E.; Rapaport, R. Full spectral and angular characterization of highly directional emission from nanocrystal quantum dots positioned on circular plasmonic lenses. *Nano Letters* **2014**, *14*, 5766.

[39] Livneh, N.; Harats, M. G.; Yochelis, S.; Paltiel, Y.; Rapaport, R. Efficient collection of light from colloidal quantum dots with a hybrid metal–dielectric nanoantenna. *ACS Photonics* **2015**, *2*, 1669.

[40] Sapienza, L.; Davanço, M.; Badolato, A.; Srinivasan, K. Nanoscale optical positioning of single quantum dots for bright and pure single-photon emission. *Nature Communications* **2015**, *6*, 7833.

[41] Aouani, H.; Itzhakov, S.; Gachet, D.; Devaux, E.; Ebbesen, T. W.; Rigneault, H.; Oron, D.; Wenger, J. Colloidal quantum dots as probes of excitation field enhancement in photonic antennas. *ACS Nano* **2010**, *4*, 4571.

[42] Mohtashami, A.; Osorio, C. I.; Koenderink, A. F. Angle-resolved polarimetry of antenna-mediated fluorescence. *Physical Review Applied* **2015**, *4*, 054014.

[43] Li, L.; Chen, E. H.; Zheng, J.; Mouradian, S. L.; Dolde, F.; Schröder, T.; Karaveli, S.; Markham, M. L.; Twitchen, D. J.; Englund, D. Efficient photon collection from a nitrogen vacancy center in a circular bullseye grating. *Nano Letters* **2015**, *15*, 1493.

[44] Aouani, H.; Mahboub, O.; Bonod, N.; Devaux, E.; Popov, E.; Rigneault, H.; Ebbesen, T. W.; Wenger, J. Bright unidirectional fluorescence emission of molecules in a nanoaperture with plasmonic corrugations. *Nano Letters* **2011**, *11*, 637.

[45] Wenger, J.; Gerard, D.; Aouani, H.; Rigneault, H.; Lowder, B.; Blair, S.; Devaux, E.; Ebbesen, T. W. Nanoaperture-enhanced signal-to-noise ratio in fluorescence correlation spectroscopy. *Analytical Chemistry* **2008**, *81*, 834.

[46] Laux, E.; Genet, C.; Skauli, T.; Ebbesen, T. W. Plasmonic photon sorters for spectral and polarimetric imaging. *Nature Photonics* **2008**, *2*, 161.

[47] Levene, M. J.; Korlach, J.; Turner, S. W.; Foquet, M.; Craighead, H. G.; Webb, W. W. Zero-mode waveguides for single-molecule analysis at high concentrations. *Science* **2003**, *299*, 682.

[48] Chu, Y.; Banaee, M. G.; Crozier, K. B. Double-resonance plasmon substrates for surface-enhanced Raman scattering with enhancement at excitation and stokes frequencies. *ACS Nano* **2010**, *4*, 2804.

[49] Turkmen, M.; Aksu, S.; Çetin, A.; Yanik, A. A.; Altug, H. Multi-resonant metamaterials based on UT-shaped nano-aperture antennas. *Optics Express* **2011**, *19*, 7921.

[50] Cetin, A. E.; Turkmen, M.; Aksu, S.; Etezadi, D.; Altug, H. Multi-resonant compact nanoaperture with accessible large nearfields. *Applied Physics B* **2015**, *118*, 29.

[51] Hughes, T. W.; Fan, S. Plasmonic Circuit Theory for Multiresonant Light Funneling to a Single Spatial Hot Spot. *Nano Letters* **2016**, *16*, 5764.

[52] Sedoglavich, N.; Sharpe, J. C.; Künnemeyer, R.; Rubanov, S. Polarisation and wavelength selective transmission through nanohole structures with multiple grating geometry. *Optics Express* **2008**, *16*, 5832.

[53] Sedoglavich, N.; Künnemeyer, R.; Sharpe, J. C. Polarization tunable selective polariton generator. *Applied Physics Letters* **2009**, *94*, 101111.

[54] Jiao, X.; Blair, S. Polarization multiplexed optical bullseye antennas. *Plasmonics* **2012**, *7*, 39.

[55] Nazari, T.; Kassani, S. H.; Khazaeinezhad, R.; Oh, K. Polarization dependent transmission through a sub-wavelength hexagonal aperture surrounded by segmented polygonal grooves. *Optics Express* **2013**, *21*, 32668.

[56] Maier, S. A. *Plasmonics: fundamentals and applications*; Springer Science & Business Media, 2007.

[57] Park, J. H.; Ambwani, P.; Manno, M.; Lindquist, N. C.; Nagpal, P.; Oh, S.-H.; Leighton, C.; Norris, D. J. Single-crystalline silver films for plasmonics. *Advanced Materials* **2012**, *24*, 3988.

[58] Marquier, F.; Arnold, C.; Laroche, M.; Greffet, J.-J.; Chen, Y. Degree of polarization of thermal light emitted by gratings supporting surface waves. *Optics Express* **2008**, *16*, 5305.

[59] Li, L.; Li, T.; Tang, X.-M.; Wang, S.-M.; Wang, Q.-J.; Zhu, S.-N. Plasmonic polarization generator in well-routed beaming. *Light: Science and Applications* **2015**, *4*, e330.

[60] Osorio, C. I.; Mohtashami, A.; Koenderink, A. F. K-space polarimetry of bullseye plasmon antennas. *Scientific Reports* **2015**, *5*, 9966.

[61] Clarke, D.; Grainger, J. F. *Polarized light and optical measurement*; Elsevier, 2013; Vol. 35.

[62] Berry, H. G.; Gabrielse, G.; Livingston, A. Measurement of the Stokes parameters of light. *Applied Optics* **1977**, *16*, 3200.

[63] Collett, E. *Field guide to polarization*; SPIE press Bellingham, 2005; Vol. 15.

[64] Alivisatos, P. The use of nanocrystals in biological detection. *Nature Biotechnology* **2004**, *22*, 47.

[65] Eid, J. et al. Real-time DNA sequencing from single polymerase molecules. *Science* **2009**, *323*, 133.

[66] Beija, M.; Afonso, C. A.; Martinho, J. M. Synthesis and applications of Rhodamine derivatives as fluorescent probes. *Chemical Society Reviews* **2009**, *38*, 2410.

[67] Korlach, J.; Marks, P. J.; Cicero, R. L.; Gray, J. J.; Murphy, D. L.; Roitman, D. B.; Pham, T. T.; Otto, G. A.; Foquet, M.; Turner, S. W. Selective aluminum passivation for targeted immobilization of single DNA polymerase molecules in zero-mode waveguide nanostructures. *Proceedings of the National Academy of Sciences* **2008**, *105*, 1176.

[68] Livneh, N.; Harats, M. G.; Istrati, D.; Eisenberg, H. S.; Rapaport, R. Highly directional room-temperature single photon device. *Nano Letters* **2016**, *16*, 2527.

[69] Yun, H.; Lee, S.-Y.; Hong, K.; Yeom, J.; Lee, B. Plasmonic cavity-apertures as dynamic pixels for the simultaneous control of colour and intensity. *Nature Communications* **2015**, *6*, 7133.

[70] Chen, J.; Li, T.; Wang, S.; Zhu, S. Multiplexed holograms by surface plasmon propagation and polarized scattering. *Nano Letters* **2017**, *17*, 5051.

[71] Li, Z.; Clark, A. W.; Cooper, J. M. Dual color plasmonic pixels create a polarization controlled nano color palette. *ACS Nano* **2016**, *10*, 492, PMID: 26631346.

[72] Jeanmaire, D. L.; Van Duyne, R. P. Surface Raman spectroelectrochemistry: Part I. Heterocyclic, aromatic, and aliphatic amines adsorbed on the anodized silver electrode. *Journal of Electroanalytical Chemistry and Interfacial Electrochemistry* **1977**, *84*, 1.

[73] Sharma, B.; Frontiera, R. R.; Henry, A.-I.; Ringe, E.; Van Duyne, R. P. SERS: Materials, applications, and the future. *Materials Today* **2012**, *15*, 16.

[74] Le Ru, E. C.; Etchegoin, P. G. Quantifying SERS enhancements. *MRS bulletin* **2013**, *38*, 631.

[75] Bauch, M.; Toma, K.; Toma, M.; Zhang, Q.; Dostalek, J. Plasmon-enhanced fluorescence biosensors: a review. *Plasmonics* **2014**, *9*, 781.

[76] Hutter, E.; Fendler, J. H. Exploitation of localized surface plasmon resonance. *Advanced Materials* **2004**, *16*, 1685.

[77] Willets, K. A.; Van Duyne, R. P. Localized surface plasmon resonance spectroscopy and sensing. *Annual Review of Physical Chemistry* **2007**, *58*, 267.

[78] Lal, S.; Grady, N. K.; Kundu, J.; Levin, C. S.; Lassiter, J. B.; Halas, N. J. Tailoring plasmonic substrates for surface enhanced spectroscopies. *Chemical Society Reviews* **2008**, *37*, 898.

[79] Brolo, A. G.; Kwok, S. C.; Moffitt, M. G.; Gordon, R.; Riordon, J.; Kavanagh, K. L. Enhanced fluorescence from arrays of nanoholes in a gold film. *Journal of the American Chemical Society* **2005**, *127*, 14936.

[80] Barnes, W. L.; Dereux, A.; Ebbesen, T. W. Surface plasmon subwavelength optics. *Nature* **2003**, *424*, 824.

[81] Lesuffleur, A.; Im, H.; Lindquist, N. C.; Oh, S.-H. Periodic nanohole arrays with shape-enhanced plasmon resonance as real-time biosensors. *Applied Physics Letters* **2007**, *90*, 243110.

[82] Yanik, A. A.; Cetin, A. E.; Huang, M.; Artar, A.; Mousavi, S. H.; Khanikaev, A.; Connor, J. H.; Shvets, G.; Altug, H. Seeing protein monolayers with naked eye through plasmonic Fano resonances. *Proceedings of the National Academy of Sciences* **2011**, *108*, 11784.

[83] Cetin, A. E.; Etezadi, D.; Galarreta, B. C.; Busson, M. P.; Eksioglu, Y.; Altug, H. Plasmonic nanohole arrays on a robust hybrid substrate for highly sensitive label-free biosensing. *ACS Photonics* **2015**, *2*, 1167.

[84] Yokogawa, S.; Burgos, S. P.; Atwater, H. A. Plasmonic color filters for CMOS image sensor applications. *Nano Letters* **2012**, *12*, 4349.

[85] Inoue, D.; Miura, A.; Nomura, T.; Fujikawa, H.; Sato, K.; Ikeda, N.; Tsuya, D.; Sugimoto, Y.; Koide, Y. Polarization independent visible color filter comprising an aluminum film with surface-plasmon enhanced transmission through a subwavelength array of holes. *Applied Physics Letters* **2011**, *98*, 093113.

[86] Koerkamp, K. K.; Enoch, S.; Segerink, F. B.; Van Hulst, N.; Kuipers, L. Strong influence of hole shape on extraordinary transmission through periodic arrays of subwavelength holes. *Physical Review Letters* **2004**, *92*, 183901.

[87] Arteaga, O.; Maoz, B. M.; Nichols, S.; Markovich, G.; Kahr, B. Complete polarimetry on the asymmetric transmission through subwavelength hole arrays. *Optics Express* **2014**, *22*, 13719.

[88] Lee, Y.; Park, M.-K.; Kim, S.; Shin, J. H.; Moon, C.; Hwang, J. Y.; Choi, J.-C.; Park, H.; Kim, H.-R.; Jang, J. E. Electrical broad tuning of plasmonic color filter employing an asymmetric-lattice nanohole array of metasurface controlled by polarization rotator. *ACS Photonics* **2017**, *4*, 1954.

[89] De Leo, E.; Cocina, A.; Tiwari, P.; Poulikakos, L. V.; Marqués-Gallego, P.; Le Feber, B.; Norris, D. J.; Prins, F. Polarization multiplexing of fluorescent emission using multiresonant plasmonic antennas. *ACS Nano* **2017**, *11*, 12167.

[90] Nagpal, P.; Lindquist, N. C.; Oh, S.-H.; Norris, D. J. Ultrasmooth patterned metals for plasmonics and metamaterials. *Science* **2009**, *325*, 594.

[91] McPeak, K. M.; Jayanti, S. V.; Kress, S. J.; Meyer, S.; Iotti, S.; Rossinelli, A.; Norris, D. J. Plasmonic films can easily be better: rules and recipes. *ACS Photonics* **2015**, *2*, 326.

[92] Tenner, V. T.; de Dood, M.; van Exter, M. Surface plasmon dispersion in hexagonal, honeycomb and kagome plasmonic crystals. *Optics Express* **2016**, *24*, 29624.

[93] Bao, J.; Bawendi, M. G. A colloidal quantum dot spectrometer. *Nature* **2015**, *523*, 67.

[94] Tittl, A.; Leitis, A.; Liu, M.; Yesilkoy, F.; Choi, D.-Y.; Neshev, D. N.; Kivshar, Y. S.; Altug, H. Imaging-based molecular barcoding with pixelated dielectric metasurfaces. *Science* **2018**, *360*, 1105.

[95] Duempelmann, L.; Gallinet, B.; Novotny, L. Multispectral Imaging with Tunable Plasmonic Filters. *ACS Photonics* **2017**, *4*, 236.

[96] Rodrigo, D.; Tittl, A.; Ait-Bouziad, N.; John-Herpin, A.; Limaj, O.; Kelly, C.; Yoo, D.; Wittenberg, N. J.; Oh, S. H.; Lashuel, H. A.; Altug, H. Resolving molecule-specific information in dynamic lipid membrane processes with multi-resonant infrared metasurfaces. *Nature Communications* **2018**, *9*, 2160.

[97] Genevet, P.; Capasso, F.; Aieta, F.; Khorasaninejad, M.; Devlin, R. Recent advances in planar optics: from plasmonic to dielectric metasurfaces. *Optica* **2017**, *4*, 139.

[98] Prins, F.; Kim, D. K.; Cui, J.; De Leo, E.; Spiegel, L. L.; McPeak, K. M.; Norris, D. J. Direct patterning of colloidal quantum-dot thin films for enhanced and spectrally selective out-coupling of emission. *Nano Letters* **2017**, *17*, 1319.

[99] Rubinsztein-Dunlop, H. et al. Roadmap on structured light. *Journal of Optics* **2017**, *19*, 013001.

[100] Deubel, M.; Von Freymann, G.; Wegener, M.; Pereira, S.; Busch, K.; Soukoulis, C. M. Direct laser writing of three-dimensional photonic-crystal templates for telecommunications. *Nature Materials* **2004**, *3*, 444.

[101] Allen, L.; Padgett, M.; Babiker, M. *Progress in Optics*; Elsevier, 1999; Vol. 39; p 291.

[102] Dennis, M. R.; O'Holleran, K.; Padgett, M. J. *Progress in Optics*; Elsevier, 2009; Vol. 53; p 293.

[103] Dorn, R.; Quabis, S.; Leuchs, G. Sharper focus for a radially polarized light beam. *Physical Review Letters* **2003**, *91*, 233901.

[104] Molloy, J. E.; Padgett, M. J. Lights, action: optical tweezers. *Contemporary Physics* **2002**, *43*, 241.

[105] Naidoo, D.; Roux, F. S.; Dudley, A.; Litvin, I.; Piccirillo, B.; Marrucci, L.; Forbes, A. Controlled generation of higher-order Poincaré sphere beams from a laser. *Nature Photonics* **2016**, *10*, 327.

[106] Alivisatos, A. P. Semiconductor clusters, nanocrystals, and quantum dots. *Science* **1996**, *271*, 933.

[107] Kim, J. Y.; Voznyy, O.; Zhitomirsky, D.; Sargent, E. H. 25th Anniversary Article: Colloidal Quantum Dot Materials and Devices: A Quarter-Century of Advances. *Advanced Materials* **2013**, *25*, 4986.

[108] Murray, C.; Norris, D. J.; Bawendi, M. G. Synthesis and characterization of nearly monodisperse CdE (E= sulfur, selenium, tellurium) semiconductor nanocrystallites. *Journal of the American Chemical Society* **1993**, *115*, 8706.

[109] Chen, O.; Zhao, J.; Chauhan, V. P.; Cui, J.; Wong, C.; Harris, D. K.; Wei, H.; Han, H. S.; Fukumura, D.; Jain, R. K.; Bawendi, M. G. Compact high-quality CdSe-CdS core-shell nanocrystals with narrow emission linewidths and suppressed blinking. *Nature Materials* **2013**, *12*, 445.

[110] Shirasaki, Y.; Supran, G. J.; Bawendi, M. G.; Bulović, V. Emergence of colloidal quantum-dot light-emitting technologies. *Nature Photonics* **2013**, *7*, 13.

[111] Jang, E.; Jun, S.; Jang, H.; Lim, J.; Kim, B.; Kim, Y. White-light-emitting diodes with quantum dot color converters for display backlights. *Advanced Materials* **2010**, *22*, 3076.

[112] Kim, T. H.; Cho, K. S.; Lee, E. K.; Lee, S. J.; Chae, J.; Kim, J. W.; Kim, D. H.; Kwon, J. Y.; Amaratunga, G.; Lee, S. Y.; Choi, B. L.; Kuk, Y.; Kim, J. M.; Kim, K. Full-colour quantum dot displays fabricated by transfer printing. *Nature Photonics* **2011**, *5*, 176.

[113] Colvin, V.; Schlamp, M.; Alivisatos, A. P. Light-emitting diodes made from cadmium selenide nanocrystals and a semiconducting polymer. *Nature* **1994**, *370*, 354.

[114] Bourzac, K. Quantum dots go on display: adoption by TV makers could expand the market for light-emitting nanocrystals. *Nature* **2013**, *493*, 283.

[115] Matterson, B. J.; Lupton, J. M.; Safonov, A. F.; Salt, M. G.; Barnes, W. L.; Samuel, I. D. Increased efficiency and controlled light output from a microstructured light-emitting diode. *Advanced Materials* **2001**, *13*, 123.

[116] Lupton, J. M.; Matterson, B. J.; Samuel, I. D.; Jory, M. J.; Barnes, W. L. Bragg scattering from periodically microstructured light emitting diodes. *Applied Physics Letters* **2000**, *77*, 3340.

[117] Jebali, A.; Mahrt, R. F.; Moll, N.; Erni, D.; Bauer, C.; Bona, G.-L.; Bächtold, W. Lasing in organic circular grating structures. *Journal of Applied Physics* **2004**, *96*, 3043.

[118] Ziebarth, J. M.; Saafir, A. K.; Fan, S.; McGehee, M. D. Extracting light from polymer light-emitting diodes using stamped bragg gratings. *Advanced Functional Materials* **2004**, *14*, 451.

[119] Yang, J.; Choi, M. K.; Kim, D.-H.; Hyeon, T. Designed assembly and integration of colloidal nanocrystals for device applications. *Advanced Materials* **2016**, *28*, 1176.

[120] Wood, V.; Panzer, M. J.; Chen, J.; Bradley, M. S.; Halpert, J. E.; Bawendi, M. G.; Bulović, V. Inkjet-printed quantum dot–polymer composites for full-color ac-driven displays. *Advanced Materials* **2009**, *21*, 2151.

[121] Kress, S. J.; Richner, P.; Jayanti, S. V.; Galliker, P.; Kim, D. K.; Poulikakos, D.; Norris, D. J. Near-field light design with colloidal quantum dots for photonics and plasmonics. *Nano Letters* **2014**, *14*, 5827.

[122] Kim, L.; Anikeeva, P. O.; Coe-Sullivan, S. A.; Steckel, J. S.; Bawendi, M. G.; Bulovic, V. Contact printing of quantum dot light-emitting devices. *Nano Letters* **2008**, *8*, 4513.

[123] Lessel, M.; Bäumchen, O.; Klos, M.; Hähl, H.; Fetzer, R.; Paulus, M.; Seemann, R.; Jacobs, K. Self-assembled silane monolayers: an efficient step-by-step recipe for high-quality, low energy surfaces. *Surface and Interface Analysis* **2015**, *47*, 557.

[124] McPeak, K. M.; van Engers, C. D.; Bianchi, S.; Rossinelli, A.; Poulikakos, L. V.; Bernard, L.; Herrmann, S.; Kim, D. K.; Burger, S.; Blome, M.; Jayanti, S. V.; Norris, D. J. Ultraviolet plasmonic chirality from colloidal aluminum nanoparticles exhibiting charge-selective protein detection. *Advanced Materials 27*, 6244.

[125] Erdogan, T.; Hall, D. Circularly symmetric distributed feedback semiconductor laser: an analysis. *Journal of Applied Physics* **1990**, *68*, 1435.

[126] Chubb, D. *Fundamentals of thermophotovoltaic energy conversion*; Elsevier, 2007.

[127] Bauer, T. *Thermophotovoltaics: basic principles and critical aspects of system design*; Springer Science & Business Media, 2011.

[128] Greffet, J.-J.; Carminati, R.; Joulain, K.; Mulet, J.-P.; Mainguy, S.; Chen, Y. Coherent emission of light by thermal sources. *Nature* **2002**, *416*, 61.

[129] Arnold, C.; Marquier, F.; Garin, M.; Pardo, F.; Collin, S.; Bardou, N.; Pelouard, J.-L.; Greffet, J.-J. Coherent thermal infrared emission by two-dimensional silicon carbide gratings. *Physical Review B* **2012**, *86*, 035316.

[130] Costantini, D.; Lefebvre, A.; Coutrot, A.-L.; Moldovan-Doyen, I.; Hugonin, J.-P.; Boutami, S.; Marquier, F.; Benisty, H.; Greffet, J.-J. Plasmonic metasurface for directional and frequency-selective thermal emission. *Physical Review Applied* **2015**, *4*, 014023.

[131] Lochbaum, A.; Fedoryshyn, Y.; Dorodnyy, A.; Koch, U.; Hafner, C.; Leuthold, J. On-chip narrowband thermal emitter for mid-IR optical gas sensing. *ACS Photonics* **2017**, *4*, 1371.

[132] Lenert, A.; Bierman, D. M.; Nam, Y.; Chan, W. R.; Celanović, I.; Soljačić, M.; Wang, E. N. A nanophotonic solar thermophotovoltaic device. *Nature Nanotechnology* **2014**, *9*, 126.

[133] Arpin, K. A.; Losego, M. D.; Cloud, A. N.; Ning, H.; Mallek, J.; Sergeant, N. P.; Zhu, L.; Yu, Z.; Kalanyan, B.; Parsons, G. N.; Girolami, G. S.; Abelson, J. R.; Fan, S.; Braun, P. V. Three-dimensional self-assembled photonic crystals with high temperature stability for thermal emission modification. *Nature Communications* **2013**, *4*, 2630.

[134] Rinnerbauer, V.; Lenert, A.; Bierman, D. M.; Yeng, Y. X.; Chan, W. R.; Geil, R. D.; Senkevich, J. J.; Joannopoulos, J. D.; Wang, E. N.; Soljačić, M.; Celanovic, I. Metallic photonic crystal absorber-emitter for efficient spectral control in high-temperature solar thermophotovoltaics. *Advanced Energy Materials* **2014**, *4*, 1400334.

[135] Nagpal, P.; Han, S. E.; Stein, A.; Norris, D. J. Efficient low-temperature thermophotovoltaic emitters from metallic photonic crystals. *Nano Letters* **2008**, *8*, 3238.

[136] Fleming, J.; Lin, S.; El-Kady, I.; Biswas, R.; Ho, K. All-metallic three-dimensional photonic crystals with a large infrared bandgap. *Nature* **2002**, *417*, 52.

[137] Čelanović, I.; Ghebrebrhan, M.; Yeng, Y. X.; Kassakian, J.; Soljačić, M.; Joannopoulos, J. Photonic crystals: shaping the flow of thermal radiation. *MRS Online Proceedings Library Archive* **2009**, *1162*.

[138] Kirchhoff, G. Ueber das Verhältniss zwischen dem Emissionsvermögen und dem Absorptionsvermögen der Körper für Wärme und Licht. *Annalen der Physik 185*, 275.

[139] Komarevskiy, N. On the optimal design of photonic structures. Ph.D. thesis, ETH Zurich, 2013.

[140] Palik, E. D. *Handbook of optical constants of solids*; Elsevier, 1997.

[141] Thornton, J. A. Influence of apparatus geometry and deposition conditions on the structure and topography of thick sputtered coatings. *Journal of Vacuum Science and Technology* **1974**, *11*, 666.

[142] Petrov, I.; Barna, P.; Hultman, L.; Greene, J. Microstructural evolution during film growth. *Journal of Vacuum Science and Technology A: Vacuum, Surfaces, and Films* **2003**, *21*, S117.

[143] Vink, T.; Somers, M.; Daams, J.; Dirks, A. Stress, strain, and microstructure of sputter-deposited Mo thin films. *Journal of Applied Physics* **1991**, *70*, 4301.

[144] Klug, H. P.; Alexander, L. E. *X-ray diffraction procedures: for polycrystalline and amorphous materials*; Wiley, 1974.

[145] Metiu, H.; Das, P. The electromagnetic theory of surface enhanced spectroscopy. *Annual Review of Physical Chemistry* **1984**, *35*, 507.

[146] Dahan, N.; Gorodetski, Y.; Frischwasser, K.; Kleiner, V.; Hasman, E. Geometric Doppler effect: spin-split dispersion of thermal radiation. *Physical Review Letters* **2010**, *105*, 136402.

[147] Frischwasser, K.; Yulevich, I.; Kleiner, V.; Hasman, E. Rashba-like spin degeneracy breaking in coupled thermal antenna lattices. *Optics Express* **2011**, *19*, 23475.

[148] Greffet, J.-J.; Bouchon, P.; Brucoli, G.; Marquier, F. Light emission by nonequilibrium bodies: local Kirchhoff law. *Physical Review X* **2018**, *8*, 021008.

[149] Mahboub, O.; Palacios, S. C.; Genet, C.; Garcia-Vidal, F.; Rodrigo, S. G.; Martin-Moreno, L.; Ebbesen, T. Optimization of bull's eye structures for transmission enhancement. *Optics Express* **2010**, *18*, 11292.

[150] Yu, W. W.; Qu, L.; Guo, W.; Peng, X. Experimental determination of the extinction coefficient of CdTe, CdSe, and CdS nanocrystals. *Chemistry of Materials* **2003**, *15*, 2854.

[151] Reiss, P.; Bleuse, J.; Pron, A. Highly luminescent CdSe/ZnSe core/shell nanocrystals of low size dispersion. *Nano Letters* **2002**, *2*, 781.

[152] Boldt, K.; Kirkwood, N.; Beane, G. A.; Mulvaney, P. Synthesis of highly luminescent and photo-stable, graded shell CdSe/$Cd_xZn_{1-x}S$ nanoparticles by in situ alloying. *Chemistry of Materials* **2013**, *25*, 4731.

[153] van Exter, M.; Tenner, V.; van Beijnum, F.; de Dood, M.; van Veldhoven, P.; Geluk, E.; 't Hooft, G. W. Surface plasmon dispersion in metal hole array lasers. *Optics Express* **2013**, *21*, 27422.

[154] Schanda, J. *Colorimetry: understanding the CIE system*; John Wiley & Sons, 2007.

[155] Hunt, R. W. G.; Pointer, M. R. *Measuring colour*; John Wiley & Sons, 2011.

[156] Bae, W. K.; Char, K.; Hur, H.; Lee, S. Single-step synthesis of quantum dots with chemical composition gradients. *Chemistry of Materials* **2008**, *20*, 531.

[157] Lee, K.-H.; Lee, J.-H.; Song, W.-S.; Ko, H.; Lee, C.; Lee, J.-H.; Yang, H. Highly efficient, color-pure, color-stable blue quantum dot light-emitting devices. *ACS Nano* **2013**, *7*, 7295.

Appendix A

Supporting information for: Polarization multiplexing of fluorescent emission using multiresonant plasmonic antennas

A.1 Influence of the number of periodicities

The number of periodicities of a bull's-eye antenna can significantly impact its transmission performances. It has been shown that an increase in the number of rings that surround the central aperture can lead to higher transmission enhancements if the propagation lengths of the surface plasmons are sufficiently long [149]. In order to determine an efficient design of our structure with respect to this parameter, we investigated multiresonant antennas with increasing number of periodicities. In Figure A.1a-d, we report the k-space images of 600 nm light with a 10 nm bandwidth transmitted through such antennas. In Figure A.1e-h we report intensity line traces extracted along the green markers of Figure A.1a-d. As evident from both k-space images and line traces, an increasing number of rings increases the transmitted intensity and decreases the FWHM of the individual arcs. Quantitatively, the FWHM of the resonances for 5, 10, 20 and 40 rings are ± 5.8, 4.0, 2.0 and 1.6°, respectively (see Figure A.1i). The monotonically improving performance up to 40 periods is a clear indication of long plasmon propagation lengths on our single-crystalline silver films [57]. Since a smaller FWHM is beneficial to distinguish between two spectrally-close colors, we chose to proceed with 20-ring structures as a good compromise between enhanced performances and FIB fabrication times. Being probed with light of a finite spectral width, the widths of

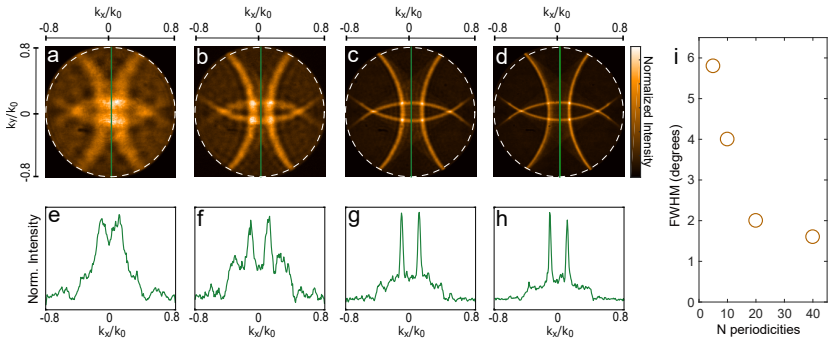

Figure A.1 – (a-d) k-space maps for the antenna design of Figure 1a fabricated with increasing number of periodicities (5, 10, 20 and 40) and excited with a 600 +/- 5 nm wavelength source. (e-h) Respective intensity line traces along the green marker of (a-d). (i) FWHM as a function of the number of periodicities. The smooth surface of the structures allows for long plasmon propagation lengths and therefore the FWHM of the resonances decreases with increasing number of periodicities. Reprinted with permission from [89], `https://pubs.acs.org/doi/abs/10.1021/acsnano.7b05269`. Further permissions related to the material excerpted should be directed to ACS.

the resonances in Figure A.2 are spectrally broadened. To investigate the fundamental width of the resonances, we illuminate our rectangular antenna of 20 rings with a broadband light source (white-light LED, Thorlabs MWWHLP1K) and disperse the $k_y/k_0 = 0$ line-trace of the collected k-space by projecting it onto an imaging spectrograph. We obtain the dispersed k-space map of Figure A.2a, by which it is possible to separate the spectral divergence from the intrinsic resonance width of the structure. At the resonant wavelength $\lambda_{\text{res}} = 650$ nm, we measure an angular divergence with FWHM = 1.6°. This is the divergence that we would obtain when exciting the structure with truly monochromatic light of 650 nm (see green line in Figure A.2b). In real applications, this minimum divergence will be a function of the spectral bandwidth of the light. For example, for the transmission measurements using 650 +/- 5

nm illumination, a small broadening of the divergence is observed (see red line in Figure A.2b).

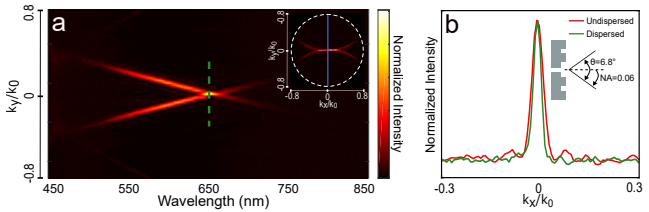

Figure A.2 – (a) The polarized k-space map from a rectangular antenna (as shown in inset for the case of a 10 nm bandwidth excitation) is recorded for a broadband excitation and the light along $k_x/k0 = 0$ (blue line in inset) is spectrally dispersed. (b) Cross-section of the dispersed k-space of (a) along the green dotted line superimposed to the cross-section of the undispersed k-space of the inset in (a). Reprinted with permission from [89], `https://pubs.acs.org/doi/abs/10.1021/acsnano.7b05269`. Further permissions related to the material excerpted should be directed to ACS.

A.2 Low-NA transmission measurements

Spectral transmission measurements of rectangular, hexagonal, and octagonal bull's-eye structures were also performed. The setup in Figure 2.3 was used, substituting the high-NA collection objective with a low NA one (NA = 0.06). The collected light is dispersed and analyzed using the spectrometer and CCD camera. The obtained spectral transmission data is normalized by the transmission through a single hole without corrugations. The different polarization components can be selected by simply introducing a linear polarization analyzer after the collection objective (Figure A.3b) allowing for a simplified readout scheme that avoids any need for high-NA optics.

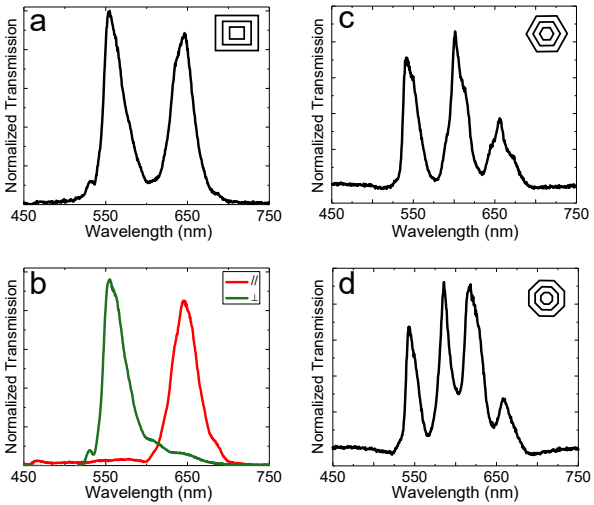

Figure A.3 – Normalized transmission spectra from (a) rectangular, (c) hexagonal and (d) octagonal multiresonant bull's-eye antennas. (b) Polarization-resolved transmission of the spectrum in (a). The analyzer is oriented parallel and orthogonal to the longest axis of the rectangular structure. Reprinted with permission from [89], `https://pubs.acs.org/doi/abs/10.1021/acsnano.7b05269`. Further permissions related to the material excerpted should be directed to ACS.

A.3 Synthesis and deposition of core-shell-shell CdSe/CdZnS quantum dots

CdSe cores with a lowest energy exciton peak at 505 nm, 535 nm and 587 nm (diameters of 2.4 nm, 2.8 nm, and 4.1 nm, respectively, as determined by Yu *et al.* [150]) were prepared modifying the reported procedure by Reiss *et. al.* [98, 151] The synthesis of core-shell-shell CdSe/CdZnS dots was performed according to the method reported by Boldt *et al.* [152] 4 monolayers (ML) of CdS and 2 ML of ZnS were grown on CdSe cores

with a 4.1 nm and 2.8 nm diameter to yield red- and orange-emitting core/shell/shell dots, respectively. For green-emitting core/shell/shell dots, 2ML of CdS and 2 ML of ZnS were grown on CdSe cores with a 2.4 nm diameter. The required precursor amounts were estimated considering the core size and desired shell thickness (each CdS shell and each ZnS shell increased the radius by 0.337 and 0.312 nm, respectively). The resulting nanocrystals were precipitated from the crude solution using acetone and small amounts of ethanol. The bright precipitate was dispersed in hexane and washed with acetone and ethanol. The nanocrystals were collected after centrifugation at 4000 rpm (2147 g) for 10 minutes. This step was repeated three times. The final product was dispersed in hexane and stored in the dark until used. The synthesis resulted in CdSe/CdZnS core/shell nanocrystals with an emission peak at 635 nm and FWHM of 29 nm for red-emitting quantum dots, 600 nm with FWHM of 35 nm for orange-emitting dots and 565 nm with FWHM of 31 nm for green-emitting quantum dots.

The colloidal quantum dots were deposited on the patterned Ag films using drop-casting from 9:1 hexane:octane solutions. 20 μl of the dispersions were deposited on the 15 mm diameter disks to create a quantum dot film in the aperture of the antennas.

Appendix B

Supporting information for: Polarization multiplexing of fluorescent emission using multiresonant plasmonic nanoaperture arrays

B.1 Photonic band structure

B.1.1 Momentum conservation

To describe the resonant wavelength and the photonic band structure, the momentum conservation for surface plasmons is used:

$$k_{\mathrm{sp}} = k_{\mathrm{inc}} + G \tag{B.1}$$

where $G = 2\pi/\Lambda$ is the momentum gain due to the grating character of the hole array, k_{inc} is the in-plane momentum of the incoming light and $k_{\mathrm{sp}} = n_{\mathrm{eff}}\omega/c$. Differently from linear gratings, the various hole array structures give rise to momentum gain in different directions, leading to a vectorial form of the momentum conservation as:

$$|\mathbf{k}_{\mathrm{SP}}| = |\mathbf{k}_{\mathrm{inc}} + \mathbf{G}| \tag{B.2}$$

$$\frac{2\pi}{\lambda}\sqrt{\frac{\varepsilon_m\varepsilon_d}{\varepsilon_m+\varepsilon_d}} = \left|\mathbf{k}_0\sin(\theta) + \sum_{i=1}^{2} m_i \frac{2\pi}{\Lambda_i}\widehat{\mathbf{e}_\mathbf{i}}\right| \tag{B.3}$$

where $\widehat{\mathbf{e}_\mathbf{i}}$ is the lattice direction vector, m_i the diffraction order mode and $\mathbf{k}_0\sin(\theta) = k_0\sin(\theta)\begin{pmatrix}\cos\alpha\\ \sin\alpha\end{pmatrix}$, with α essentially describing the array orientation to the slit.

The wavelength dependent dielectric constant of silver, $\varepsilon_m = \varepsilon_m^{'} + i\varepsilon_m^{''}$, is taken from ellipsometry values measured in McPeak *et al.* [91]. The dielectric of the epoxy used in the template stripping fabrication step is given by the manufacturer (Norland) as:

$$n = 1.5015 + \frac{8290.45\cdot 1}{\lambda^2} - \frac{2.11046\cdot 10^8\cdot 1}{\lambda^4} \tag{B.4}$$

$$\varepsilon = n^2 \tag{B.5}$$

The lattice directions and diffraction orders for the four different types of arrays are shown in Figure B.1

Square/Rectangular array:

$$\frac{2\pi}{\lambda}\sqrt{\frac{\varepsilon_m\varepsilon_d}{\varepsilon_m+\varepsilon_d}} = \left|k_0\sin(\theta) + m_1\frac{2\pi}{\Lambda_1}\begin{pmatrix}1\\0\end{pmatrix} + m_2\frac{2\pi}{\Lambda_2}\begin{pmatrix}0\\1\end{pmatrix}\right| \tag{B.6}$$

With $m = [m_1 m_2]$ the diffraction mode, where we only consider the four fundamental modes:
$m = [\pm 1\ 0], [0\ \pm 1]$
Solving the equation for λ as a function of k returns the photonic band structure as measured in the dispersed k-space.

The next higher order modes that are not considered for the square and rectangular hole arrays lead to an effective shorter pitch due to the

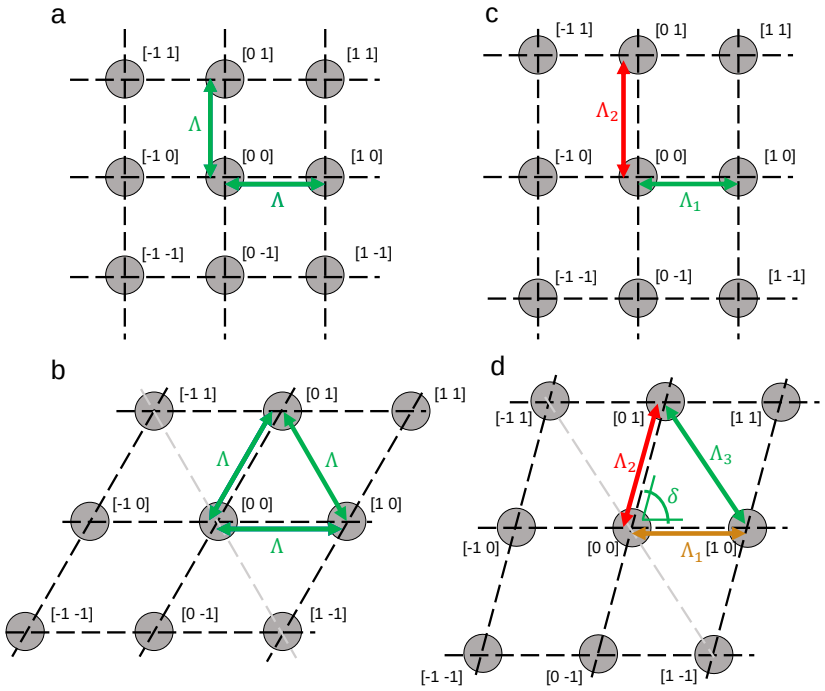

Figure B.1 – Lattice with marked periodicities and diffraction order directions for a (a) square, (b) hexagonal, (c) rectangular and (d) oblique hole array.

right-angle characteristic of the arrays:

$$G = \left| \pm \frac{2\pi}{\Lambda_1} \begin{pmatrix} 1 \\ 0 \end{pmatrix} \pm \frac{2\pi}{\Lambda_2} \begin{pmatrix} 0 \\ 1 \end{pmatrix} \right| = 2\pi \sqrt{\frac{1}{\Lambda_1^2} + \frac{1}{\Lambda_2^2}} = 2\pi \frac{\sqrt{\Lambda_1^2 + \Lambda_2^2}}{\Lambda_1 \Lambda_2} \quad \text{(B.7)}$$

$$\Lambda_{\text{eff}} = \frac{\Lambda_1 \Lambda_2}{\sqrt{\Lambda_1^2 + \Lambda_2^2}} \tag{B.8}$$

Which is always smaller than Λ_1, Λ_2 leading to a resonance in the blue spectral regime.

Hexagonal/Oblique array:

$$\frac{2\pi}{\lambda}\sqrt{\frac{\varepsilon_m \varepsilon_d}{\varepsilon_m + \varepsilon_d}} = \left| k_0 \sin(\theta) + m_1 \frac{2\pi}{\Lambda_1}\begin{pmatrix}1\\0\end{pmatrix} + m_2 \frac{2\pi}{\Lambda_2}\begin{pmatrix}\cos\delta\\ \sin\delta\end{pmatrix}\right| \tag{B.9}$$

With $m = [m_1 m_2]$ the diffraction mode, where in this case we form a set of six modes:
$m = [\pm 1\ 0], [0\ \pm 1], [\pm 1\ \mp 1]$
and the angle δ is defined as:

$$\delta = \arccos\left(\frac{-\Lambda_3^2 + \Lambda_1^2 + \Lambda_2^2}{2\Lambda_1 \Lambda_2}\right) \tag{B.10}$$

The angle for the hexagonal structure is per definition fixed to 60°, which leads to momentum gain for the $[\pm 1\ \ \mp 1]$:

$$\begin{aligned} G &= \left| \pm\frac{2\pi}{\Lambda}\begin{pmatrix}1\\0\end{pmatrix} \mp \frac{2\pi}{\Lambda}\begin{pmatrix}\cos 60^\circ\\ \sin 60^\circ\end{pmatrix}\right| = \left|\frac{2\pi}{\Lambda}\begin{pmatrix}\pm 1 \mp \cos 60^\circ\\ \mp \sin 60^\circ\end{pmatrix}\right| \\ &= \left|\frac{2\pi}{\Lambda}\begin{pmatrix}\pm 1 \mp \cos 60^\circ\\ \mp \sin 60^\circ\end{pmatrix}\right| = \left|\frac{2\pi}{\Lambda}\begin{pmatrix}\pm \cos 60^\circ\\ \mp \sin 60^\circ\end{pmatrix}\right| \end{aligned} \tag{B.11}$$

Which is equal to the momentum gain of the two fundamental modes, leading to the same resonance. This allows for the equivalent representation with a basis set of three vectors $m = [i\ j\ k]$, that is sometimes found in literature.

Due to the symmetry breaking in the oblique structure, the $[\pm 1\ \mp 1]$

modes result in a resonance with lower energy compared to the four fundamental modes. These modes do not directly correspond to the third periodicity defined in the building block, but is tuneable by the angle $\delta = f(\Lambda_3)$.

B.1.2 Coupled-mode interaction

To accurately describe the photonic band structures of hole arrays, we use a coupled-mode model for the surface plasmon interaction as shown by van Exter *et al.* [153]. The time evolution of the surface plasmon field is described as:

$$\frac{dE}{dt} = -iHE \tag{B.12}$$

Where H is the scattering matrix. We assume all scattering rates to be real valued and write the matrix for the square and rectangular case as:

$$H = \begin{bmatrix} EV_{10} & \gamma_1 & \kappa_2 & \kappa_1 \\ \gamma_1 & EV_{\bar{1}0} & \kappa_1 & \kappa_2 \\ \kappa_2 & \kappa_1 & EV_{01} & \gamma_2 \\ \kappa_1 & \kappa_2 & \gamma_2 & EV_{0\bar{1}} \end{bmatrix} \tag{B.13}$$

where EV_i are the solutions to the uncoupled-modes discussed in the previous chapter, γ_i are the back-scattering rates and κ_i are the right-angle scattering rates. As γ and κ are wavelength dependent, we introduce two different values denoted with the subscript 1, 2 as the rectangular structure has multiple crossings at different wavelengths.

The hexagonal structure that incorporate now six modes leads to the

symmetric 6x6-matrix:

$$H = \begin{bmatrix} EV_{10} & \gamma & \mu & \kappa & \kappa & \mu \\ \gamma & EV_{\bar{1}0} & \kappa & \mu & \mu & \kappa \\ \mu & \kappa & EV_{01} & \gamma & \mu & \kappa \\ \kappa & \mu & \gamma & EV_{0\bar{1}} & \kappa & \mu \\ \kappa & \mu & \mu & \kappa & EV_{1\bar{1}} & \gamma \\ \mu & \kappa & \kappa & \mu & \gamma & EV_{\bar{1}1} \end{bmatrix} \tag{B.14}$$

where γ is the back-scattering rate and κ and μ the 60°and 120°angle-dependent scattering rates.

Due to the broad spectral range and increasing complexity in the oblique structure, we consider now eight modes to capture interactions at high NA. These modes are:
$m = [\pm 1\ 0], [0\ \pm 1], [\pm 1\ \mp 1], [\pm 1\ \pm 1]$
represented in the 8x8 scattering matrix:

$$H = \begin{bmatrix} EV_{10} & \gamma_1 & \mu_1 & \kappa & \kappa & \mu_2 & \chi & \chi \\ \gamma_1 & EV_{\bar{1}0} & \kappa & \mu_1 & \mu_2 & \kappa & \chi & \chi \\ \mu_1 & \kappa & EV_{01} & \gamma_2 & \mu_1 & \kappa & 0 & 0 \\ \kappa & \mu_1 & \gamma_2 & EV_{0\bar{1}} & \kappa & \mu_1 & 0 & 0 \\ \kappa & \mu_2 & \mu_1 & \kappa & EV_{1\bar{1}} & \gamma_3 & \psi & \psi \\ \mu_2 & \kappa & \kappa & \mu_1 & \gamma_3 & EV_{\bar{1}1} & \psi & \psi \\ \chi & \chi & 0 & 0 & \psi & \psi & EV_{11} & \gamma_4 \\ \chi & \chi & 0 & 0 & \psi & \psi & \gamma_4 & EV_{\bar{1}\bar{1}} \end{bmatrix} \tag{B.15}$$

where we do not using all potential scattering parameters for the oblique case due to the complexity of the fitting problem. We highlight that the backscattering rates γ_i have the largest influence in describing the beaming resonances, as they determine the splitting of the positive and negative mode at $k = 0$

By solving the eigenvalue problem of the time evolution of the surface

plasmon field, we find the solutions to the coupled-modes that are shown in Figure 3.3. The parameters used for the fittings are given in Table B.1.

Since the model assumes a flat metal-dielectric interface, while the holes will introduce an additional change in the effective refractive index, arising differences are corrected by assuming an effective pitch.

Structure: Square								
Parameters:	**Period** x	**Period** y	γ_1	γ_2	κ_1	κ_2	α	
Model:	300 nm	300 nm	0.18	0.18	0.08	0.08	10°	
System:	300 nm	300 nm						
Structure: Rectangular								
Parameters:	**Period** x	**Period** y	γ_1	γ_2	κ_1	κ_2	α	
Model:	300 nm	390 nm	0.16	0.08	0.04	0.06	10°	
System:	300 nm	375 nm						
Structure: Hexagonal								
Parameters:	**Period** Λ	γ	κ	μ	α			
Model:	305 nm	0.14	0.08	0.06	5°			
System:	350 nm							
Structure: Oblique								
Parameters:	**Period** Λ_1	**Period** Λ_2	**Period** Λ_3	γ_1	γ_2	γ_3		
Model:	375 nm	420 nm	495 nm	0.06	0.04	0.10		
System:	375 nm	420 nm	495 nm					

Parameters:	γ_4	κ	μ_1	μ_2	χ	ψ	α
Model:	0.07	0.03	0.015	0.055	0.10	0.02	45°

Table B.1 – Table of fitting parameters.

Appendix C

Supporting information for: Multispectral quantum-dot nanostructures fabricated via direct-patterning to tailor fluorescent emission

C.1 CIE mapping

The spectral response $L_e(\lambda)$ for a cQD RGB hexagonal structure measured as a function of polarization angle is presented in Figure 4.7b. Tristimulus values represent the amount of three primary colors necessary to reproduce a certain color as perceived by the human eye and are obtained as [154]:

$$\begin{aligned} X &= \int_{\lambda} L_e(\lambda)\overline{x}(\lambda)d\lambda \\ Y &= \int_{\lambda} L_e(\lambda)\overline{y}(\lambda)d\lambda \\ Z &= \int_{\lambda} L_e(\lambda)\overline{z}(\lambda)d\lambda \end{aligned} \tag{C.1}$$

where $\overline{x}(\lambda), \overline{y}(\lambda), \overline{z}(\lambda)$ are the color-matching functions (as in Figure C.1), each corresponding to a primary color, that take into account the human eye response to reconstruct the visible spectrum. The chromaticity values

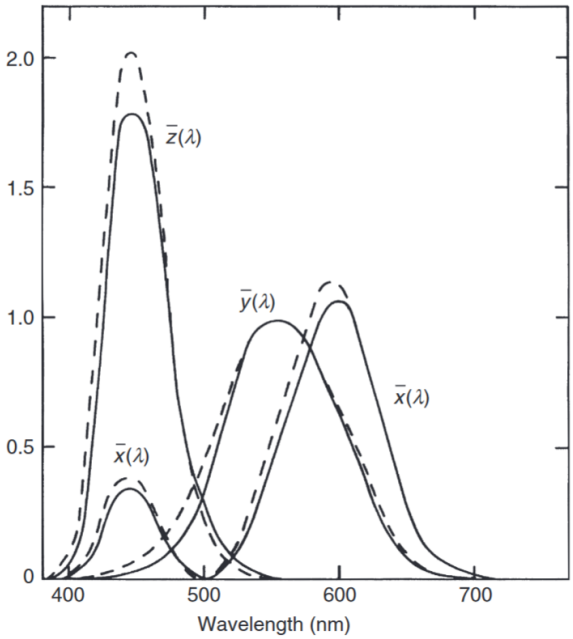

Figure C.1 – CIE color-matching functions from [155] for the 1931 (continuous lines) and 1964 (broken lines) Standard Colorimetric Observer. Reprinted with permission from [155], Copyright 2011 John Wiley and Sons, Inc.

represented on the CIE diagram of Figure 4.7c are then calculated as:

$$\begin{aligned} x &= \frac{X}{X+Y+Z} \\ y &= \frac{Y}{X+Y+Z} \\ z &= 1-x-y \end{aligned} \tag{C.2}$$

C.2 k-space polarimetry of linear gratings

Full k-space polarimetry for a cQD linear grating with periodicity $\Lambda = 450$ nm and $\lambda_{em} = 635$ nm is presented in Figure C.2.

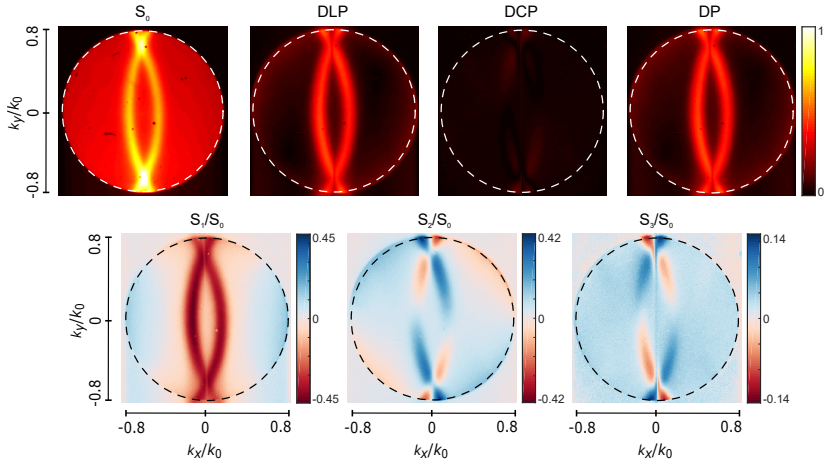

Figure C.2 – k-space polarimetry for a cQD linear grating with periodicity $\Lambda = 450$ nm. The four normalized Stokes parameters are presented along with the degree of linear polarization (DLP), degree of circular polarization (DCP) and total degree of polarization (DP).

C.3 Material synthesis*

C.3.1 Chemicals

Cadmium oxide (CdO, 99.999%) was purchased from Strem Chemicals. n-dodecylphosphonic acid (DDPA, 98%) was purchased from Epsilon Chimie. 1-butanol (ACS Grade) was purchased from Merck KGaA. Diphenylphosphine (DPP, 98%), ethanol (96%), hexadecylamine (HDA, 90%), hexane (95%), methanol (99.9%), selenium pellets (99.999%), sulfur (99.5%), trioctylphosphine (TOP, 90% and 97%), trioctylphosphine oxide (TOPO, 90%), 1-octadecene (ODE, 90%), 1-octanethiol (98.5%), octylamine (99%), oleylamine (OAm, 70%), oleic acid (OLA, 90%), and zinc acetate [Zn(ac)2, 99.99%] were purchased from Sigma.

Cadmium oleate stock and zinc oleate stock were prepared as previously reported1 and stored in the glovebox for future use.

C.3.2 Preparation of red-emitting core/shell quantum dots

CdSe cores with a lowest energy exciton peak of 579 nm (size approximately 3.8 nm, as determined by Yu *et al.* [150]) were synthesized following a modified version of a procedure by Reiss *et. al.* [151] Briefly, 822 mg of CdO (6.4 mmol), 16.2 g of TOPO (42 mmol), 37 g of HDA (153.2 mmol), and 3.215 g of DDPA (12.8 mmol) were combined in a 250 mL 4-neck round-bottom flask and heated to 90°C under N_2(g). Then, the mixture was degassed 3 times to below 0.1 Torr with stirring at 1000 rpm. The flask was filled with N_2(g) and heated at 320°C until the solution turned clear. The temperature was then reduced to 260°C and 8 mL of 1M Se in TOP (97%) solution containing 85 μL of DPP was swiftly injected at 300 rpm. After injection, the stir rate was increased to 1000 rpm and the temperature was maintained at 260°C. The growth of

*This Section is based on the following publication:
Prins, F.*; Kim D. K.*; Cui J.; De Leo E.; Spiegel L. L.; McPeak K.; Norris D. J. *Nano Letters* **2016**, *17*, 1319, `https://pubs.acs.org/doi/abs/10.1021/acs.nanolett.6b03212`. Further permissions related to the material excerpted should be directed to ACS.

CdSe nanocrystals was monitored using an UV-visible spectrophotometer (Varian Cary 300, UV-VIS). The reaction was quenched by removing the heating mantle, cooling to 200°C with an air gun, submerging the flask in a water bath, and adding 40 mL of 1-butanol at 130°C to prevent solidification. To isolate the product, the reaction mixture was split into 6 centrifuge tubes and methanol was added to reach a total volume of 50 mL in each tube. A precipitate was collected by centrifugation at 4000 rpm for 10 min, redispersed in 20 mL of hexane, and left undisturbed overnight at room temperature (RT). The following day, the mixture was centrifuged at 4000 rpm for 20 min, the supernatant was transferred to 6 centrifuge tubes, and ethanol was added to precipitate the product. The nanocrystals were isolated by centrifugation at 4000 rpm for 10 min. The precipitate in each tube was dispersed in 4 mL of hexane to be precipitated out once more with ethanol and centrifuged under the same conditions. The nanocrystals were dispersed in a 20 mL of hexane and stored in the dark until further use.

The growth of the CdS/ZnS shell on CdSe nanocrystals was performed following Boldt *et al.* [152] and as previously reported by our group.1 Briefly, 100 nmol of CdSe nanocrystals in hexane, 3 mL of ODE, and 3 mL of OAm were combined in a 3-neck 100 mL round-bottom flask and degassed at RT for 1 h. The mixture was then heated at 120°C for 20 min. The flask was filled with N_2(g) and heated to 305°C at a rate of 16°C/min. At 210°C, two separate syringes containing cadmium oleate (0.22 mmol) and octanethiol (0.26 mmol), each diluted in ODE (final volume of 3 mL), were injected with a syringe pump at a rate of 1.5 mL/h. After injection, the temperature was lowered to 200°C, 1 mL of degassed OLA was added dropwise, and the mixture was allowed to anneal for 1 h at 200°C. Subsequently, the temperature was lowered to 120°C and the reaction mixture was degassed for 30 min. The flask was then filled with N_2(g) and the temperature was raised to 280°C at a rate of 16°C/min. At 210°C, two separate syringes containing zinc oleate (0.24 mmol) and octanethiol (0.48 mmol) each diluted in ODE (final volume of 3 mL) were injected with a syringe pump at a rate of 2.5 mL/h. After injection, the reaction mixture was quickly cooled down to RT. To precipitate and clean the nanocrystals, an equivalent amount of ethanol to reaction-mixture volume was added and centrifuged at 4000 rpm for 10 min. The bright

precipitate was dispersed in 4 mL of hexane, 10 mL of ethanol was added, and the mixture was centrifuged under the same conditions. This step was repeated (2 mL of hexane and 5 mL of ethanol). The product was dispersed in a small volume of hexane and stored in the dark until future use. The recipe resulted in core/shell nanocrystals with a lowest energy excitonic absorption peak at 607 nm and an emission peak at 622 nm with a full-width-at-half-maximum (FWHM) of 28 nm.

C.3.3 Preparation of green-emitting core/shell quantum dots

The core/shell CdSe/ZnS nanocrystals with a composition gradient were prepared by modifying a procedure by Bae *et al.* [156] Briefly, 51.4 mg of CdO (0.4 mmol), 734 mg of $Zn(ac)_2$ (3.34 mmol), and 2 mL of OLA (6 mmol) were combined in a 3-neck 100 mL round-bottom flask and degassed 3 times under 0.1 Torr. The mixture was heated at 150°C and degassed for 30 min. Then, the flask was filled with N_2(g), 15 mL of degassed ODE was added and degassed at 120°C for an additional 5 min. Subsequently, the mixture was heated at 310°C to form a clear solution. 3 mL of TOP (90°) containing 0.2 mmol Se and 4 mmol S was then swiftly injected into the reaction mixture. The temperature was maintained at 300°C for 10 min and it was then quickly cooled down to RT. The reaction mixture was transferred to a centrifuge tube, filled with ethanol, vortexed and centrifuged at 4000 rpm for 10 min. This ethanol extraction procedure was repeated (typically 5 times) until a bright pellet was fully precipitated with a clear supernatant. The product was dispersed in 8 mL of hexane and stored in the dark until future use. The recipe resulted in core-shell nanocrystals with a lowest energy excitonic absorption peak at 530 nm and an emission peak at 545 nm.

To grow a ZnS shell on CdSe/ZnS nanocrystals a modified recipe by Boldt *et al.* was followed. Briefly, 100 nmol of CdSe/ZnS nanocrystals in hexane (which was approximated with an absorption cross-section of 517 nm CdSe cores), 3 mL of ODE, 3 mL of OAm, and 1 mL OLA were combined in a 3-neck 100 mL round-bottom flask and degassed at room temperature for 1 h. The mixture was heated to 120°C for 20 min, switched to N_2(g) and raised to 280°C at a rate of 16°C/min. When 210°C was reached, two

separate syringes containing zinc oleate (0.25 mmol) and octanethiol (0.5 mmol), each diluted in ODE (final volume of 3 mL), were injected using a syringe pump at a rate of 2.5 mL/h. After injection, the temperature was lowered to 200°C and 1 mL of degassed OLA was added dropwise. The reaction annealed at 200°C for 1 h, and then it was quickly cooled down to RT. The nanocrystals were purified and isolated by precipitation with ethanol and centrifugation at 4000 rpm for 10 min. The resulting bright precipitate was dispersed in 2 mL of hexane 5 mL of ethanol was slowly added, and the mixture was centrifuged once more. This step was repeated (1 mL hexane and 3 mL ethanol). The product was dispersed in 3 mL of hexane and stored in the dark until future use. The recipe resulted in nanocrystals with a lowest energy excitonic absorption peak at 505 nm and an emission peak at 526 nm with a FWHM of 29 nm.

C.3.4 Preparation of blue-emitting core/shell quantum dots

The core/shell nanocrystals with a composition gradient were prepared by modifying a procedure by Lee *et al.* [157] Briefly, 128.4 mg of CdO (1 mmol), 1832 mg of $Zn(ac)_2$ (8.3 mmol), and 7 mL of OLA (22 mmol) were combined in a 3-neck 100 mL round-bottom flask. The mixture was degassed 3 times under 0.1 Torr and at 150°C for 20 min while stirring at 1000 rpm. The flask was filled with N_2(g), 15 mL of degassed ODE was added, and the mixture was degassed at 120°C for 10 min. The flask was filled with N_2(g) and heated to 305°C to obtain a clear solution. At 305°C, a clear solution consisting of 3 mL of ODE with 1.6 mmol of S prepared inside the glovebox, was swiftly injected into the reaction mixture. After injection, the temperature was maintained at 305°C for 12 min. Subsequently, a clear solution consisting of 5 mL of OLA with 4 mmol of sulfur prepared in the glovebox, was injected with a syringe pump at a rate of 0.5 mL/min. After injection, the temperature was maintained at 305°C for 3 h. After annealing, the reaction mixture was quickly cooled down to RT. To precipitate and purify the nanocrystals, the reaction mixture was split into two centrifuge tubes. Then 20 mL of ethanol was added to each tube and centrifuged at 8000 rpm for 10 min. The solid was dispersed in 5 mL of hexane, 1 mL of octylamine was added, and the mixture was sonicated for 5 min. Then, 20 mL of ethanol

was added and the mixture was centrifuged at 8000 rpm for 10 min. The cleaning process was repeated 2 times. The particles were cleaned 3 times using a combination of hexane (4 mL) and a mixture of acetone (10 mL) ethanol (20 mL), with a clear supernatant being discarded each time. The particles were dispersed in 5 mL of hexane and stored in the dark until future use. The recipe resulted in core/shell nanocrystals with a lowest energy excitonic absorption peak at 450 nm and an emission peak at 460 nm with a FWHM of 25 nm.